

**ANGULAR GATING AND BIOLOGICAL
SCATTERING IN OPTICAL MICROSCOPY**

SI KE

NATIONAL UNIVERSITY OF SINGAPORE

2011

**ANGULAR GATING AND BIOLOGICAL
SCATTERING IN OPTICAL MICROSCOPY**

SI KE

B. Eng. (Hons.), Zhejiang University, China

**A THESIS SUBMITTED
FOR THE DEGREE OF DOCTOR OF PHILOSOPHY**

Acknowledgements

My thesis is a result of an exciting journey first undertaken in 2007. During the four years research study in National University of Singapore, I have met many nice people who helped me and gave me big encouragement:

First and foremost, I would like to express my sincere appreciation to my supervisor Prof. Colin J. R. Sheppard for his supervision and guidance throughout my postgraduate study. It is also very impressive that Prof. Colin is always willing to find the time to sit down and discuss and solve problems with us, just like a good friend. I believe and appreciate that Prof. Sheppard has an extraordinary impact on my future research career. Without his invaluable suggestions and patient discussions, this thesis could not be completed.

I am also grateful for my co-supervisor Prof. Hanry Yu and Dr. Chen Nanguang, who taught me useful knowledge on optics and biology research and gave me a lot of useful discussion, especially on the experiments. I enjoyed every discussion with them and will never forget their valuable advices and contributions. I greatly appreciate the generous support from Prof. Teoh Swee Hin and Dr. Chui Chee Kong for their guidance for my lab rotation project. I would also thank my thesis advisory committee member Dr. Huang Zhiwei for his scientific inputs and continuous support. His valuable during my PhD qualification exam helps me to steer more smoothly towards the completion of this thesis work.

I would like to thank for the enthusiastic discussions and suggestions given by my coworkers and team members: Waiteng, Shakil, Elijah, Shanshan, Shalin and Naveen. I also would like to thank the support and understanding of all the other students and staff in Optical Bioimaging Laboratory, especially Dr. Zheng Wei, Dr. Gao Guangjun, Shau Poh Chong, Teh Seng Knoon, Liu Linbo, Shao Xiaozhuo, Lu Fake, Mo Jianhua, Zhang Qiang, Chen Ling, and Lin Kan.

My special thanks also to my parents, it is their love that makes me become the happiest person in the world. I am also willing to express my most special thanks to my wife Dr Gong Wei for her support and understanding. Despite how hard the reverse and difficulty are, she always believes in me and offers me support and encouragement.

Last but not least, I would like to acknowledge the financial support from NGS (NUS Graduate School for Integrative Sciences &Engineering).

Table of Contents

Acknowledgements	I
Table of Contents	II
Summary	V
List of Publications	VII
List of Tables	X
List of Figures	XI
List of Abbreviations	XVI
Chapter 1 Introduction	1
1.1 Background	1
1.2 Motivation.....	3
1.2.1 Light scattering modeling.....	5
1.2.2 Angular gating techniques.....	8
1.3 Significance of the research	12
1.4 Structure of the thesis	14
Chapter 2 Literature reviews.....	18
2.1 Conventional scattering models.....	18
2.1.1 Discrete model.....	18
2.1.2 Fractal model.....	23
2.2 Optical microscopy	27
2.2.1 Confocal microscopy.....	27
2.2.2 Multi-photon microscopy.....	29

2.2.3	4Pi microscopy.....	32
Chapter 3	Model for light scattering in biological tissue and cells	40
3.1	Introduction.....	40
3.2	Discrete model with rough surface nonspherical particles.....	41
3.3	Fractal model in biological tissue.....	51
3.4	Conclusion.....	57
Chapter 4	Confocal microscopy using angular gating techniques.....	61
4.1	Introduction.....	61
4.2	Confocal scanning microscope with D-shaped apertures.....	63
4.2.1	Coherent transfer function	64
4.2.2	Optical transfer function.....	68
4.3	Confocal scanning microscope with off-axis apertures.....	73
4.4	Confocal scanning microscope with elliptical apertures.....	81
4.5	Confocal scanning microscope with Schwartz apertures.....	88
4.6	Conclusion.....	92
Chapter 5	One-photon focal modulation microscopy	96
5.1	Introduction.....	96
5.2	Principle of focal modulation microscopy.....	98
5.3	Optical transfer function.....	101
5.4	Axial resolution.....	103
5.5	Transverse resolution.....	106
5.6	Background rejection capability.....	112
5.7	Signal level.....	113

5.8	Conclusion.....	115
Chapter 6 Two-photon focal modulation microscopy		119
6.1	Introduction.....	119
6.2	Ballistic light analysis.....	122
6.2.1	3D Optical transfer function.....	122
6.2.2	Axial resolution.....	126
6.2.3	Transverse resolution	128
6.3	Multiple-scattering analysis.....	131
6.4	Conclusion.....	146
Chapter 7 Polarization effects in 4Pi microscopy.....		149
7.1	Introduction.....	149
7.2	Symmetry considerations.....	150
7.3	Illumination using two counter-propagating beams.....	153
7.4	Comparison of various geometries.....	163
7.5	Discussion.....	166
Chapter 8 Conclusions		169

Summary

The main purpose of my work is to precisely and effectively explore biological phenomenon in vivo by using optical method. To achieve this aim, my major work focuses on two aspects: one is to solve the fundamental problems of lack of precise optical scattering models for biological tissue and cells, and the other is to establish a high performance optical microscopy. For the first aspect, we developed a random nonspherical model and a fractal model for the biological tissue and cells. These two models are introduced based on different fundamentals and have different applications. The power spectrum of the contrast phase images is investigated. The phase function, the anisotropy factor of scattering, and the reduced scattering coefficient are derived. The effect of different size distributions is also discussed. The theoretical results show good agreement with experimental data. The application of this model in phase contrast microscopy is in process. For the second aspect, we discuss the confocal microscopy with angular gating techniques (divided apertures) and investigate the performance of focal modulation microscopy (FMM), which modifies a confocal microscopy by a combination of angular gating technique with modulation and demodulation techniques. We analytically derived the three-dimensional coherent transfer function (CTF) for reflection-mode confocal scanning microscopy with angular techniques under the paraxial approximation and also analyzed the three-dimensional incoherent transfer function (OTF) for fluorescence confocal scanning microscopy with angular gating techniques. The effects on different aperture shapes such as off-axis apertures, elliptical apertures, and Schwartz apertures are investigated. FMM was introduced to increase imaging depth into tissue and rejection of background from a thick scattering object. A theory for image formation in one-photon FMM is presented, and the effects of detecting the in-phase modulated fluorescence signal are discussed. Two different non-overlapping apertures of D-shaped and quadrant apertures are studied. Two-photon FMM was proposed by us at the first time. The enhanced depth penetration permitted by two-photon excitation with the near-infrared photons is particularly attractive for deep-tissue imaging. The investigation of the imaging depth in an extension of single-photon FMM to two-photon FMM (2PFMM)

allows the penetration depth to be three-fold of that in convention two-photon microscopy (2PM). This result suggests that 2PFMM may hold great promise for non-invasive detection of cancer and pre-cancer, treatment planning, and may also server as a research tool for small animal whole body imaging. The effects of different apodization conditions and polarization distributions on imaging in 4Pi microscopy are also discussed. With radially polarized illumination, the transverse resolution in the 4Pi mode can be increased by about 18%, but at the expense of axial resolution.

List of Publications

Journal papers

1. W. Gong, K. Si, X. Q. Ye, and W. K. Gu, "A highly robust real-time image enhancement," *Chinese Journal of Sensors and Actuators*, **9**, 58-62 (2007)
2. W. Gong, K. Si, and C. J. R. Sheppard, "Light scattering by random non-spherical particles with rough surface in biological tissue and cells," *J. Biomechanical Science and Engineering*, **2**, S171 (2007)
3. K. Si, W. Gong, C. C. Kong, and T. S. Hin, "Visualization of bone material map with novel material sensitive transfer functions," *J. Biomechanical Science and Engineering*, **2**, S211 (2007)
4. W. Gong, K. Si, and C. J. R. Sheppard. "Modeling phase functions in biological tissue," *Opt. Lett.* **33**, 1599-1601. (2008)
5. C. J. R. Sheppard, W. Gong, and K. Si, "The divided aperture technique for microscopy through scattering media," *Opt. Express*, **16**, 17031–17038 (2008)
6. K. Si, W. Gong, and C. J. R. Sheppard, "Three-dimensional coherent transfer function for a confocal microscope with two D-shaped pupils," *Appl. Opt.* **48**, 810-817 (2009)
7. K. Si, W. Gong, and C. J. R. Sheppard, "Model for light scattering in biological tissue and cells based on random rough nonspherical particles", *Appl. Opt.* **48**, 1153-1157 (2009).
8. W. Gong, K. Si, and C. J. R. Sheppard, "Optimization of axial resolution in confocal microscope with D-shaped apertures," *Appl. Opt.* **48**, 3998-4002 (2009).
9. W. Gong, K. Si, and C. J. R. Sheppard, "Improvements in confocal microscopy imaging using serrated divided apertures," *Opt. Commun.* **282**, 3846-3849 (2009).
10. K. Si, W. Gong, N. Chen, and C. J. R. Sheppard, "Edge enhancement for in-phase focal modulation microscope", *Appl. Opt.* **48**, 6290-6295 (2009).
11. W. Gong, K. Si, N. Chen, and C. J. R. Sheppard, "Improved spatial resolution in fluorescence focal modulation microscopy", *Opt. Lett.* **34**, 3508-3510 (2009).
12. W. Gong, K. Si, and C. J. R. Sheppard, "Divided-aperture technique for fluorescence confocal microscopy through scattering media," *Appl. Opt.* **49**, 752-757 (2010).
13. W. Gong, K. Si, N. Chen, and C. J. R. Sheppard, "Focal modulation microscopy with annular apertures: A numerical study," *J. Biophoton.*, doi: 10.1002/jbio.200900110 (2010).
14. C. J. R. Sheppard, W. Gong, and K. Si, "Polarization effects in 4Pi microscopy," *Micron*, doi: 10.1016/j.micron.2010.07.013 (2010).

15. K. Si, W. Gong, and C. J. R. Sheppard, "Enhanced background rejection in thick tissue using focal modulation microscopy with quadrant apertures," *Appl. Opt.*, doi:10.1016/j.optcom.2010.11.007 (2010).
16. K. Si, W. Gong, and C. J. R. Sheppard, "Penetration depth in two-photon focal modulation microscopy," *Opt. Lett.*, (submitted).

Conference presentations

1. W. Gong, K. Si, and C. J. R. Sheppard, "Light Scattering by Random Non-spherical Particles with Rough Surfaces in Biological Tissue and Cells," The 4th Scientific Meeting of the Biomedical Engineering Society of Singapore (2007).
2. K. Si, W. Gong, C. C. Kong, and T. S. Hin, "Application of Novel Material Sensitive Transfer Function in Characterizing Bone Material Properties," The 4th Scientific Meeting of the Biomedical Engineering Society of Singapore (2007).
3. W. Gong, K. Si, and C. J. R. Sheppard, "Light Scattering by Random Non-spherical Particles with Rough Surface in Biological Tissue and Cells," Third Asian Pacific Conference on Biomechanics, (2007)
4. K. Si, W. Gong, C. C. Kong, and T. S. Hin, "Visualization of Bone Material with Novel Material Sensitive Transfer Functions," Third Asian Pacific Conference on Biomechanics, (2007).
5. K. Si, W. Gong, and C. J. R. Sheppard, "3D Fractal Model for Scattering in Biological Tissue and Cells," 5th International Symposium on Nanomanufacturing, (2008)
6. K. Si, W. Gong, and C. J. R. Sheppard, "Application of Random Rough Nonspherical Particles Mode in Light Scattering in Biological Cells," GPBE/NUS-TOHOKU Graduate Student Conference in Bioengineering, (2008).
7. K. Si, W. Gong, and C. J. R. Sheppard, "Fractal Characterization of Biological Tissue with Structure Function", the Seventh Asian-Pacific Conference on Medical and Biological Engineering (APCMBE 2008)
8. K. Si, W. Gong, and C. J. R. Sheppard, "Modulation Confocal Microscope with Large Penetration Depth", SPIE Photonics West, (2009).
9. K. Si, W. Gong, and C. J. R. Sheppard, "Better Background Rejection in Focal Modulation Microscopy", OSA Frontiers in Optics (FiO)/Laser Science XXV (LS) Conference, (2009)
10. K. Si, W. Gong, N. Chen, and C. J. R. Sheppard, "Focal Modulation Microscopy with Annular Apertures," 2nd NGS Student symposium, (2010).
11. W. Gong, K. Si, N. Chen, and C. J. R. Sheppard, "Two photon focal modulation microscopy," *Focus on Microscopy*, (2010).

12. K. Si, W. Gong, N. Chen, and C. J. R. Sheppard, "Annular pupil focal modulation microscopy," *Focus on Microscopy*, (2010).
13. W. Gong, K. Si, N. Chen, and C. J. R. Sheppard, "Two-photon microscopy with simultaneous standard and enhanced imaging performance using focal modulation technique," *SPIE Photonics Europe*, (2010).
14. K. Si, W. Gong, N. Chen, and C. J. R. Sheppard, "Imaging Formation of Scattering Media by Focal Modulation Microscopy with Annular Apertures," *SPIE Photonics Europe*, (2010).

List of Tables

Table 3.1. *Anisotropy factors and reduced scattering coefficients for M1 cells and mitochondria.*51

Table 7.1. *Values of the parameters F , G_T and M for $NA = 1.46$. “% increase in resolution” is for 4Pi compared with the single lens case.....163*

List of Figures

Fig. 3.1.	<i>Phase functions with different size distribution functions with same $r_{eff} = 3.36$ and $v_{eff} = 0.12$, and same shape parameters ($K = 2, \tau = 0.7, CP = -0.5$), at incident wavelength 1100 nm.....</i>	<i>46</i>
Fig. 3.2.	<i>Phase functions for randomly oriented slight rough prolate (solid curves) and oblate (dash curves) spheroids with different aspect ratios of 1.2, 2.4, and equal-projected-area spheres with different effective size parameter S_{eff}.(a) $S_{eff} = 15$; (b) $S_{eff} = 8$.....</i>	<i>47</i>
Fig. 3.3.	<i>Phase functions for suspensions of rat embryo fibroblast cells (M1) with spherical and nonspherical model with the effective size parameter $S_{eff} = 15.5$ and experimental results</i>	<i>49</i>
Fig. 3.4.	<i>Phase functions for suspensions of mitochondria with random non-spherical model, spherical model with the effective size parameter $S_{eff} = 10.3$ and experimental results. The particles are chosen as a combination of Figure 1(c) and (d) in Ref.[5].....</i>	<i>50</i>
Fig. 3.5.	<i>Power spectrums, normalized to unity for low frequencies</i>	<i>54</i>
Fig. 3.6.	<i>Anisotropy factor as a function of kL and fractal dimension D_f</i>	<i>55</i>
Fig. 3.7.	<i>Reduced scattering coefficient as for different fractal dimensions...55</i>	
Fig. 3.8.	<i>Phase function as a function for: (a) given D_f; (b) given kL</i>	<i>56</i>
Fig. 4.1.	<i>Geometry of the confocal microscope with two centro-symmetric D-shaped pupils.</i>	<i>64</i>
Fig. 4.2.	<i>The 3-D coherent transfer functions with different distance parameter d and different angle ψ. For $d = 0$ and $\psi = \pi/2$, the 3-D CTF is the same as the conventional confocal microscope with two circular pupils....</i>	<i>66</i>
Fig. 4.3.	<i>The intensity along the axis for a D-shaped pupil shown as a log-log plot.....</i>	<i>67</i>
Fig. 4.4.	<i>3D OTFs for confocal one-photon fluorescence microscopy with D-shaped apertures with various d and v_d. (a) $C(m = 0, n, s)$ with $v_d = 0, d = 0$ and circular apertures with $v_d = 0$; (b) $C(m, n = 0, s)$ with $v_d = 0, d = 0$ (c) $C(m = 0, n, s)$ with $v_d = 4, d = 0$ and circular apertures with $v_d = 4$; (d) $C(m, n = 0, s)$ with $v_d = 4, d = 0$; (e) $C(m = 0, n, s)$ with $v_d = 0, d = 0.4$; (f) $C(m, n = 0, s)$ with $v_d = 0, d = 0.4$; (g) $C(m = 0, n, s)$ with $v_d = 4, d = 0.4$; (h) $C(m, n = 0, s)$ with $v_d = 4, d = 0.4$.</i>	<i>70</i>

Fig. 4.5.	<i>Integrated intensities of CM (solid lines) and DCM (dash lines) for (a) $v_d=0$, and (b) $v_d=4$, respectively.....</i>	72
Fig. 4.6.	<i>Two off-axis circular apertures: one for illumination, and the other for detection</i>	73
Fig. 4.7.	<i>The 3-D amplitude coherent transfer functions in the reflection-mode confocal scanning microscope with two off-axis circular apertures. .</i>	74
Fig. 4.8.	<i>Axial responses of reflection-mode confocal scanning microscope with a point detector with traditional two circular apertures (CM), with two D-shaped apertures, and with two off-axis apertures, respectively....</i>	75
Fig. 4.9.	<i>Integrated intensity of a reflection-mode confocal scanning microscope with a point detector using D-shaped and off-axis apertures.....</i>	76
Fig. 4.10.	<i>Axial response of a reflection-mode confocal scanning microscope with a point detector using D-shaped (dash lines) and off-axis apertures (solid lines) with equal area: (a) near focal plane; (b) far from the focal plane</i>	77
Fig. 4.11.	<i>Half-width-half-maximum of the axial response as a function of normalized detector size for D-shaped apertures (dash lines) and off-axis apertures (solid lines).....</i>	78
Fig. 4.12.	<i>Integrated intensity of a reflection-mode confocal scanning microscope with a point detector for D-shaped (dash lines) and off-axis apertures (solid lines).....</i>	79
Fig. 4.13.	<i>Signal level as a function of detected pinhole size for D-shaped (dash lines) and off-axis apertures (solid lines).....</i>	81
Fig. 4.14.	<i>Two elliptical apertures: one for illumination and the other for detection</i>	82
Fig. 4.15.	<i>Integrated pupil function $P_\theta(t)$ for (a) given $a = 0.8$ and $b = 0.89$; (b) $a = 0.9$ and $d = 0.3$.....</i>	83
Fig. 4.16.	<i>Axial response for elliptical apertures when u is large.....</i>	83
Fig. 4.17.	<i>Integrated intensity for elliptical apertures with given value of d.....</i>	84
Fig. 4.18.	<i>Signal level as a function of normalized detector pinhole size for elliptical apertures.....</i>	85
Fig. 4.19.	<i>Axial response for elliptical and D-shaped aperture ($a=b=1$) with equal area</i>	86
Fig. 4.20.	<i>Integrated intensity for elliptical and D-shaped ($a=b=1$) apertures with equal area</i>	87

Fig. 4.21.	<i>Signal level for elliptical and D-shaped ($a=b=1$) apertures with equal area</i>	88
Fig. 4.22.	<i>Integrated pupil function of Schwartz aperture</i>	90
Fig. 4.23.	<i>A set of Schwartz apertures with same integrated pupil function.</i>	90
Fig. 4.24.	<i>Axial response for Schwartz apertures</i>	91
Fig. 5.1.	<i>Schematic diagram of the focal modulation microscope. LBE: laser beam expander. SPM: spatial phase modulator. DM: dichroic mirror. LF: long-pass filter. PMT: photomultiplier tube. L_1 and L_2: collection lenses. L_3: objective lens</i>	98
Fig. 5.2.	<i>Three dimensional optical transfer functions for: (a) CM with a point detector; (b) CM with $v_d = 3$; (c) DFMM in horizontal direction with a point detector; (d) DFMM in horizontal direction with $v_d = 3$; (e) DFMM in vertical direction with a point detector; (f) DFMM in vertical direction with $v_d = 3$; (g) QFMM in direction a with a point detector; (h) QFMM in direction a with $v_d = 3$; (i) QFMM in direction b with a point detector; (j) QFMM in direction b with $v_d = 3$</i>	103
Fig. 5.3.	<i>The axial cross-sections of the 3D OTF of CM, DFMM and QFMM for (a) a point detector; (b) a finite size detector with $v_d = 3$</i>	104
Fig. 5.4.	<i>Images of a thick fluorescent layer for CM, DFMM and QFMM with (a) a point detector; (b) a finite size detector with $v_d = 3$</i>	105
Fig. 5.5.	<i>Images of a radial spoke pattern at the focal plane for (a) CM with a point detector; (b) DFMM with a point detector; (c) QFMM with a point detector; (d) CM with $v_d = 3$; (e) DFMM with $v_d = 3$; (f) QFMM with $v_d = 3$. The horizontal and vertical axes are in units of v</i>	107
Fig. 5.6.	<i>Image of a thick fluorescent edge in CM, DFMM and QFMM for (a) a point detector and (b) a finite size detector with $v_d = 3$</i>	108
Fig. 5.7.	<i>Image of a thin fluorescent edge in CM, DFMM and QFMM for (a) a point detector and (b) a finite size detector with $v_d = 3$</i>	110
Fig. 5.8.	<i>The total background normalized by intensity at focal point for CM, DFMM and QFMM at different values of v_d: (a) a point detector; (b) a finite size detector with $v_d = 3$</i>	113
Fig. 5.9.	<i>Signal level from a thin fluorescent sheet for DFMM and QFMM as a function of detector sizes</i>	114
Fig. 6.1.	<i>Schematic diagram of two-photon focal modulation microscopy with annular apertures. SPM: spatial phase modulator; DM: dichroic mirror; L_1 and L_2: collection lenses; L_3: objective lens; PMT: photomultiplier tube</i>	121

Fig. 6.2.	<i>The 3D OTF of (a) 2PM and (b) 2PFMM with annular apertures; (c) 2PFMM with D-shaped apertures in m direction (n=0); (d) 2PFMM with D-shaped apertures in n direction (m=0).....</i>	<i>125</i>
Fig. 6.3.	<i>Images of a thick uniform fluorescent layer scanning in the axial direction for two-photon excitation fluorescence microscopy (2P), 2PFMM with D-shaped apertures (2PDFMM), and 2PFMM with annular apertures (2PAFMM), respectively.....</i>	<i>127</i>
Fig. 6.4.	<i>Images of a thick, sharp and straight fluorescent edge scanned in the transverse direction for two-photon excitation fluorescence microscopy (2P), 2PFMM with D-shaped apertures (2PDFMM), and 2PFMM with annular apertures (2PAFMM), respectively.....</i>	<i>129</i>
Fig. 6.5.	<i>Images of a thin, sharp and straight fluorescent edge scanned in the transverse direction for two-photon excitation fluorescence microscopy (2P), 2PFMM with D-shaped apertures (2PDFMM), and 2PFMM with annular apertures (2PAFMM), respectively.....</i>	<i>131</i>
Fig. 6.6.	<i>The scattering light with various focus depth at 0μm, 400 μm, 600 μm, and 1000 μm, respectively. $l_s = 200\mu\text{m}$, $n = 1.33$, $NA = 0.566$, and $\lambda = 0.9\mu\text{m}$</i>	<i>136</i>
Fig. 6.7.	<i>The ballistic light (log value) focused at $5l_s$ with $l_s = 200\mu\text{m}$, $n = 1.33$, $NA = 0.556$, and $\lambda = 0.9\mu\text{m}$ in (a) 2PM, and (b) 2PFMM.....</i>	<i>137</i>
Fig. 6.8.	<i>The variations of the total excitation (log value) with different focal depths in: (a) focused at 0μm in 2PM, and (b) focused at 0μm in 2PFMM, (c) focused at 500μm in 2PM, and (d) focused at 500μm in 2PFMM, (e) focused at 1000μm in 2PM, and (f) focused at 1000μm in 2PFMM . $l_s = 200\mu\text{m}$, $n = 1.33$, $NA = 0.566$, and $\lambda = 0.9\mu\text{m}$</i>	<i>139</i>
Fig. 6.9.	<i>The comparison of the integrated intensity of I_{bb}, I_{sb}, I_{ss}, and I_{total} in (a) 2PM, and (b) 2PFMM. $z_0 = 1000\mu\text{m}$, $l_s = 200\mu\text{m}$, $n = 1.33$, $NA = 0.566$, $g = 0.9$, and $\lambda = 0.9\mu\text{m}$</i>	<i>140</i>

Fig. 6.10.	<i>The signal to background ratio (SBR) in 2PFMM and 2PM: (a) as a function of focus depth z and (b) as a function of anisotropic factor g. $l_s=200\mu\text{m}$, $n = 1.33$, $NA = 0.566$, and $\lambda=0.9\mu\text{m}$.....</i>	143
Fig. 6.11.	<i>The ratio of SNR in 2PFMM to SNR 2PM as a function of focus depth z_0. $l_s=200\mu\text{m}$, $n=1.33$, $NA=0.56$, and $\lambda=0.9\mu\text{m}$</i>	144
Fig. 6.12.	<i>Signal level for 2PFMM with a finite-sized detector pinhole</i>	145
Fig. 7.1.	<i>The electric and magnetic fields on the surface of the reference sphere for ingoing radiation satisfying various different polarization conditions. Electric field is shown in red and magnetic field in blue.....</i>	152
Fig. 7.2.	<i>The electric field in the front focal plane of each lens for different polarization distributions. The radius of the circles corresponds to $\sin\alpha=1$. The electric field is zero at the dashed line.....</i>	152
Fig. 7.3.	<i>The variation in the parameters F, G_x, G_y, G_T, G_A, and ε with angular semi-aperture of each objective lens in a 4Pi system. The dashed line corresponds to a numerical aperture of 1.46 in oil. A is aplanatic, Mixed is mixed dipole, ED is electric dipole, TE is transverse electric TE1, and R is radial polarization.....</i>	154
Fig. 7.4.	<i>The normalized widths of the focal spot in the transverse and axial directions for 4Pi systems for different polarization cases. (t) corresponds to the transverse direction and (a) to the axial direction. The dashed line corresponds to a numerical aperture of 1.46 in oil. A is aplanatic, Mixed is mixed dipole, ED is electric dipole, TE is transverse electric 1, and R is radial polarization.....</i>	165

List of Abbreviations

2PFMM	=	Two-photon fluorescence focal modulation microscopy
2PM	=	Two-photon excitation microscopy
3D	=	Three-dimensional
AFMM	=	FMM with annular apertures
APSF	=	Amplitude point spread functions
CP	=	Display window
CTF	=	Coherent transfer function
DCM	=	Confocal microscopy with divided D-shaped apertures
DDA	=	Discrete dipole approximation
DFMM	=	FMM with divided D-shaped apertures
D/L	=	Diameter-to-length ratio
ED	=	Electric dipole
FDTD	=	Finite difference time domain method
FEM	=	Finite element method
FIEM	=	Fredholm integral equation method
FMM	=	Focal modulation microscopy
FOCSM	=	Fiber optic confocal scanning microscope
FWHM	=	Full-widths at half-maximum
HWHM	=	Half-widths at half-maximum
IPFMM	=	In-phase focal modulation microscopy
IPSF	=	Intensity point spread function
LBE	=	Laser beam expander
MPM	=	Multi-photon microscopy
NA	=	Numerical aperture
NIR	=	Near-infrared
OCT	=	Optical coherent tomography
OPFOS	=	Orthogonal-plane fluorescence optical sectioning

OTF	=	Optical transfer function
PMM	=	Point matching method
PMT	=	Photomultiplier tube
PSF	=	Point spread function
QFMM	=	FMM with divided quadrant apertures
RDG	=	Rayleigh-Debye-Gans
SAX	=	Saturated excitation microscopy
SNR	=	Signal to background ratio
SPIM	=	Selected plane illumination microscopy
SPM	=	Spatial phase modulator
SVM	=	Separation of variables method
TMM	=	T-matrix method
UV	=	Ultraviolet
W-M	=	Weierstrass-Maddelbrot

Chapter 1 Introduction

1.1 Background

Biomedical optics is a rapidly emerging field that relies on advanced technologies. Among these technologies, optical imaging is unique in its ability to span the realms of biology from microscopic to macroscopic, providing both structural and functional information and insights, with uses ranging from fundamental to clinical applications. In recent years, a variety of concepts have been introduced to improve the spatial resolution of optical imaging, including confocal microscopy (CM) [1], multi-photon microscopy (MPM) [2], 4Pi microscopy [3-4], and, most recently, fluorescence photoactivation localization microscopy (fPALM) [5], stochastic optical reconstruction microscopy (STORM) [6], and divided aperture microscopy. With some of these advanced schemes, image acquisition with subcellular-resolution can be obtained in biological tissue and cells.

However, modern biological research has been extending to the molecular scale. Thus it is significantly important to develop a high performance optical microscopy. But to build such an optical microscopy, we still have to face two challenges. The first one is that there is lack of a precise light scattering model for biological tissue and cells. A scattering model is recognized as the key factor to fundamentally improve the spatial resolution of optical microscopy.

Now, although it is recognized that the optical scattering properties of tissue and cells are related to its microstructure and refractive index, the nature of the relationship is still poorly understood. Previous investigations have focused on various aspects of this relationship, including the contribution of mitochondria to the scattering properties of the live cell [7], the spatial variations in the refractive index of cells and tissue sections [8], and the diffraction properties of single cells [9]. Still lacking, however, is a quantitative model that related the microscopic properties of cells and other tissue elements to the scattering coefficients of bulk tissue. Therefore, in order to fundamentally improve the spatial resolution of optical microscopy, we introduced a scattering model based on random nonspherical particles to study tissue optical properties.

The second challenge is that for optical microscopy there is a tradeoff between the imaging penetration depth and the spatial resolution. Thus it is difficult to build a high performance optical microscope which can obtain high spatial resolution and deep imaging penetration depth simultaneously. For instance, CM is a well established, powerful technique for biological research, mainly due to its optical sectioning properties by the use of a pinhole. In combination with fluorescence microscopy, confocal microscopy enables unprecedented studies of cells and tissue both *in vitro* and *in vivo*. However, when the focal point moves deep into the tissue, its point spread function broadens dramatically because of the effect of multi-scattering, which significantly degrades the spatial resolution, thus reducing the imaging

penetration depth [2]. MPM is an alternative method to CM, and utilizes an ultrashort laser to further localize the illumination spot. By employing nonlinear processes, such as two photon excited fluorescence or second-harmonic generation, MPM can obtain a high resolution image when the imaging depth is less than 1mm [10]. However, compared with CM the spatial resolution of MPM is not improved. Moreover, MPM is an expensive technique, and its applications are limited by its complex probes. To build a high performance optical microscope is significantly important and urgent for biological research. Therefore focal modulation microscopy was developed in our laboratory, based on angular gating technique, a novel technique that targets an imaging depth greater than 0.5 mm combined with diffraction limited spatial resolution and molecular specificity.

The subsequent sections provide an overview of high resolution microscopy and different models in tissue optics.

1.2 Motivation

Optical imaging is a powerful tool for studying biology. Compared to other imaging methods, optical imaging has the advantage of providing molecular information through, for example, Raman scattering or fluorescence.

There are two fundamental challenges in optical imaging. One is diffraction, which limits the spatial resolution of an optical imaging system.

Over the past two decades, various methods have been developed to break the diffraction limit and provide three-dimensional super-resolution images. The other challenge is scattering. Except in creatures such as jellyfish, most biological tissues are not transparent. This is mainly because of optical scattering in tissues. Despite advances in imaging technologies, tissue scattering remains a significant challenge.

Most optical imaging systems rely on an objective lens to form an optical focus or to project the image onto a camera. For either method to work, the sample being imaged must be highly transparent and the optical path length inhomogeneity within the sample must be much less than the optical wavelength (a few hundred nanometers). For tissues that are more than several hundred microns thick, scattering is a significant problem. This thesis aims to develop a new tool for millimeter-scale deep-tissue imaging.

The advance of high-resolution and high-sensitivity optical molecular imaging has revolutionized the way biological events are viewed and studied. Because many biological events happen below the surface, it is important to develop a robust, turnkey tool that biologists can use to see deeper inside tissues. My research aims to enable optical focusing inside tissues and to provide a platform to implement fluorescence and nonlinear microscopy with high sensitivity. To achieve this goal, we are focused on the following two steps. The first one is to establish a better light scattering model to describe scattering process much more precisely. This step aims to fundamentally

improve imaging performance of microscopy, such as spatial resolution and confidence. The other one is to develop a microscopy with better resolution, higher sensitivity and deeper penetration depth. This helps to observe biological events below the surface.

1.2.1 Light scattering modeling

The optical properties of tissue and cells are of key significance in optical biomedical technology, such as in optical imaging and spectroscopy. Currently, for simplicity of computation, most preliminary studies are based on two models: discrete models and fractal models. Both of them have assumed that the scatterers in biological tissue and cells are homogeneous, isotropic, and smooth [11-12]. However, microstructure in biological tissue and cells can consist of different types of particles having arbitrary shapes, size distributions [13], and orientations, as well as an overall mass density that varies spatially within them. Besides, the optical properties of real tissue differ significantly from the theoretical homogeneously distributed smooth spherical particles.

Biological tissue is composed of tightly packed groups of cells entrapped in a network of fibers through which water percolates. Viewed on a microscopic scale, the constituents of the tissue have no clear boundaries [11]. They appear to merge into a continuous structure distinguished optically only by spatial variations in the refractive index. Schmitt and Kumar [14] provided

a statistical approach to model the complicated structure of soft tissue as a collection of particles. Mourant *et al.* [15] demonstrated that there was a distribution of scatterer sizes in biological tissue. However, both of their approaches are based on Mie theory which is under three assumptions that the medium is homogeneous and isotropic, and the scattering particles are spheres. Since candidates for scattering centers in biological tissue, such as cell itself, the nucleus, other organelles, and structures within organelles, have arbitrary shapes, size distributions, and orientations, the three assumptions are far from the real case. To precisely calculate the scattering properties, some researchers have developed the *T*-matrix method [16-18]. Based on Huygens principle, the *T*-matrix method is one of the most powerful and widely used tools for rigorously computing electromagnetic scattering by single and compounded particles, and is the only method that has been used in systematic surveys of nonspherical scattering based on calculations for thousands of particles in random orientation. However, according to our knowledge, the *T*-matrix method is mainly used to analyze multiple scattering by randomly distributed dust-like aerosols in aerospace, and it has not been applied in biological research.

On a microscopic scale, the constituents of the tissue do not present clear boundaries and merge into a quasi-continuum structure. Therefore, discrete particles may be less appropriate than the tissue modeling as a continuous random medium due to weak random fluctuations of the dielectric

permittivity. Some attempts have been made to incorporate the quasi-continuum effect into tissue modeling. Moscoso et al. [12] suggested that the refractive index variations exhibit fractal behavior, and showed that by assuming an exponential correlation the scattering function can be determined. More recently, Xu and Alfano [19] modified the correlation function of the random fluctuations of the dielectric permittivity with an average of exponential functions weighted by power law distribution, and showed that the resulting scattering model gives good agreement with experimental results for liver and other tissues. This implies that when the refractive index variation in biological tissue is weak, tissue can be modeled as a continuous random medium where light scattering is not due to the discontinuities in refractive index but rather to weak random fluctuations of the dielectric permittivity. Sheppard [20] extended the fractal theory and model tissue with weak random dielectric permittivity fluctuations described by an isotropic stationary random process with fractal correlation using the K -distribution. This leads to simple expressions for the scattering function, anisotropy function, phase function, reduced scattering coefficient, and scattering power, indicating a much easier way to correlate the tissue optics properties.

From the above review, it can be seen that the fractal model attempts to consider a range of scale sizes, instead of a characteristic particle size. Therefore, it is powerful when applied to a medium with small organelles. Unfortunately, all the above studies on the fractal model for tissue optics are

based on the assumption that biological tissue is isotropic. However, biological tissue and cells always show an anisotropic behavior, which vary in different directions. Chemingui [21] proposed stochastic descriptions of anisotropic fractal media, which present the von Karman functions as a generalization to media with exponential correlation functions. However, this study is far from complete, and lacks experiments to examine the correctness. Besides, the target application of the study is on seafloor morphology, which might be greatly different from biological science. Therefore, it is of practical significance to develop a fractal model that can be applied in anisotropic medium in biological tissue and cells.

In sum, the discrete model and fractal model are introduced based on different theories. From the view of application in the microscope, the discrete particle model is useful for investigating imaging at a resolution scale much larger than the size of the scatterers, such as in diffuse optical tomography. When the resolution scale is similar to that of the structural detail, such as in confocal or multiphoton microscopy, a fractal model based on a continuous refractive index variation should be an improvement [20].

1.2.2 Angular gating techniques

Confocal microscopy (CM) has wide applications in biological research and medical diagnosis, as a consequence of its ability to exclude out-of-focus information from the image data, thus improving the fidelity of focal

sectioning and increasing the contrast of fine image details. The optical sectioning ability of confocal microscopy results from the pinhole before the detector, used to reject out-of-focus light scattered by the tissue. However, when the focal point moves deep into tissue, so that multiple scattering dominates, the selective mechanism of the pinhole is not sufficiently effective. One of the methods to enhance the background rejection utilizes an angular gating mechanism, in which the illumination and detection beams overlap only in the focal region, thus resulting in angular gating and improving the optical sectioning and rejection of scattered light.

Angular gating had its beginning with the ultramicroscope, in which the sample is illuminated perpendicular to the imaging optical axis [22]. The specular microscope, or divided aperture technique, combines different beam paths for illumination and detection with confocal imaging, so that light scattered other than in the focal region is rejected [23-26]. The ultramicroscope was also the fore-runner of confocal theta microscopy [27-28], and orthogonal-plane fluorescence optical sectioning (OPFOS) [29], also known as selected plane illumination microscopy (SPIM) [30], both of which are usually implemented in a fluorescence mode. All these techniques have in common that the illuminating and detection pupils do not overlap, so that the illumination and detection beams overlap only in the focal region.

Koester also compared theoretically the optical sectioning performance of his system with that of a confocal system with a circular detector aperture,

based on geometrical optics [25-26]. Other applications based on the D-shaped pupils were given by Török *et al* [31-32]. They modified a commercial confocal microscope with a D-shaped aperture stop to realize dark-field imaging. Although their system also employed the D-shaped aperture, it was fundamentally different from Koester's bright-field confocal microscope. They derived the one-dimensional transfer function in the direction perpendicular to the edge of the beam-stop, and later on they extended their study to the dark-field and differential phase contrast imaging with two D-shaped pupils. More recently, Dwyer *et al.* have used a similar system to investigate *in vivo* human skin [33-34]. They called their system the confocal reflectance theta line-scanning microscope, to stress that their system combines confocal line-scanning with off-axis geometry, but actually their system is very similar to that of Koester [25]. In the analysis of Dwyer *et al.*, they derived the lateral resolution and sectioning strength based on two equivalent offset non-overlapping circular pupils, as an approximation to the two D-shaped pupils. Therefore, it is of practical significance to investigate the optical properties of confocal microscope with two D-shaped pupils based on diffraction optics.

Confocal microscopy is a well established, powerful technique for biological research mainly due to its optical sectioning properties by the use of a pinhole. In combination with fluorescence microscopy, confocal microscopy enables unprecedented studies of cells and tissue both *in vitro* and *in vivo*

[35-36]. However, when the focal point moves deep into the tissue, its point spread function broadens dramatically because of the effect of multi-scattering, which significantly degrades the spatial resolution [2]. In order to retain high resolution in deep regions of the tissue, numerous techniques have emerged recently. Multi-photon microscopy (MPM) utilizes an ultra-short-pulsed laser to further concentrate the illumination spot. By employing such nonlinear processes as two-photon excited fluorescence or second-harmonic generation, MPM can obtain high resolution image when the imaging depth is less than about 1 mm [2, 10]. However, MPM is an expensive technique, and its applications are limited by its complex probes.

Another promising technique, saturated excitation microscopy, utilizes the saturation phenomenon to achieve spatial resolution beyond the diffraction limit, since this technique imposes strong nonlinearity in the relation between excitation rate and fluorescence emission [37-38]. However, this technique require strong excitation intensity, which may exhibit not only photobleaching but also other undesirable effects in observation of living biological samples, such as defunctionalization of proteins by a large temperature rise. Therefore, it is of high significance to develop a comprehensive microscope technique, which maintains the optical sectioning ability and obtains a deep penetration depth as well.

1.3 Significance of the research

The main aim of this study was to investigate the underlying optical properties of biological tissue and cells, as well as to develop a high performance microscopy for biological research. The specific objectives of this research can be divided to:

- Introduction of a nonspherical scattering model to describe the optical properties in biological tissue and cells based on the T -matrix method, which can be used to precisely calculate the scattering field.
- Introduction of a fractal model to biological research based on the structure function, which is claimed to be able to investigate anisotropic surfaces [39].
- Investigation of the imaging performance of confocal microscopy with the angular gating technique.
- Establishment of a high performance microscopy named focal modulation microscopy by the combination of angular gating technique, and modulation and demodulation techniques, to simultaneously enhance the imaging penetration depth and improve the spatial resolution.

The results of this present study have practical significance on biological research and medical diagnosis since:

- The nonspherical scattering model provides a more precise model to describe the light scattering properties in biological tissue and cells, which would fundamentally improve the imaging performance of

optical microscopy.(how can a model improve imaging performance?)

- The fractal model based on structure function is able to consider the anisotropic property in biological science and describe the directional sensitivity for an anisotropic medium, which can be an alternative model to further improve the imaging performance of optical microscopy.
- Confocal microscopy with the angular gating technique can be recognized as a method to effectively reject the background signal, and thus can further improve the imaging penetration depth.
- The introduction of focal modulation microscopy, by the combination of angular gating technique and modulation and demodulation techniques, provides a new solution, which behaves excellently in both imaging penetration depth and spatial resolution.

The validity of nonspherical scattering models has been examined in both biological tissue and cells. However, for wider applications, more experiments on other tissue and cells should be done. The penetration depth and spatial resolution of focal modulation microscopy have been analyzed in this study. However, other imaging performance and other configurations are still under investigation and hence are beyond the scope of this thesis.

1. 4 Structure of the thesis

This thesis studies light scattering properties in biological tissue and cells, and angular gating techniques in optical microscopy. Chapter 2 gives literature reviews for light scattering models and optical microscopy. Chapter 3 investigates light scattering by random non-spherical particles with rough surfaces, and the fractal mechanism applied in biological tissue. The phase function, which is an important quantity to describe the angular distribution of the scattered intensity, is estimated. In Chapter 4, the three-dimensional coherent transfer function in coherent confocal microscopy and the three-dimensional optical transfer function in incoherent confocal microscopy are derived. Imaging formation in confocal microscopy using various divided apertures such as off-axis apertures, elliptical apertures and Schwartz apertures is presented and compared. Chapter 5 introduces one-photon focal modulation microscopy (FMM). The principle and system setup in FMM are provided. The diffraction analysis for D-shaped apertures, and quadrant apertures is presented. Chapter 6 extends the one-photon FMM system to two-photon FMM, and investigates the signal to background ratio and penetration depth. Chapter 7 analyzes the polarization effects in 4Pi microscopy, which is a preparation for introducing polarization effects in focal modulation microscopy. Finally conclusions and future directions are summarized in Chapter 8.

References

1. T. Wilson, and C. J. R. Sheppard, *Theory and Practice of Scanning Optical Microscopy* (Academic, London, 1984).
2. X. Deng, and M. Gu, "Penetration depth of single-, two-, and three-photon fluorescence microscopic imaging through human cortex structures: Monte Carlo simulation," *Appl. Opt.* **42**, 3321-3329 (2003).
3. S. Hell, and E. H. K. Stelzer, "Fundamental Improvement of Resolution with a 4pi-Confocal Fluorescence Microscope Using 2-Photon Excitation," *Opt Commun* **93**, 277-282 (1992).
4. S. Hell, and E. H. K. Stelzer, "Properties of a 4pi Confocal Fluorescence Microscope," *J Opt Soc Am A* **9**, 2159-2166 (1992).
5. S. T. Hess, T. P. K. Girirajan, and M. D. Mason, "Ultra-high resolution imaging by fluorescence photoactivation localization microscopy," *Biophys J* **91**, 4258-4272 (2006).
6. M. J. Rust, M. Bates, and X. W. Zhuang, "Sub-diffraction-limit imaging by stochastic optical reconstruction microscopy (STORM)," *Nat Methods* **3**, 793-795 (2006).
7. B. Beauvoit, T. Kitai, and B. Chance, "Contribution of the Mitochondrial Compartment to the Optical-Properties of the Rat-Liver - a Theoretical and Practical Approach," *Biophys J* **67**, 2501-2510 (1994).
8. J. M. Schmitt, and G. Kumar, "Turbulent nature of refractive-index variations in biological tissue," *Opt Lett* **21**, 1310-1312 (1996).
9. A. Dunn, and R. Richards-Kortum, "Three-dimensional computation of light scattering from cells," *IEEE J. Sel. Top. Quantum Electron.* **2**, 898-905 (1996).
10. P. Theer, M. T. Hasan, and W. Denk, "Two-photon imaging to a depth of 1000 μm in living brains by use of a Ti:Al₂O₃ regenerative amplifier," *Opt. Lett.* **28**, 1022-1024 (2003).
11. R. K. Wang, "Modelling optical properties of soft tissue by fractal distribution of scatters," *J. Mod. Opt.* **47**, 103-120 (2000).
12. M. I. Moscoso, J. B. Keller, and G. Papanicolaou, "Depolarization and blurring of optical images by biological tissue," *J. Opt.Soc. Am. A* **18**, 948-960 (2001).
13. M. Xu, and R. R. Alfano, "Fractal mechanisms of light scattering in biological tissue and cells," *Opt. Lett.* **30**, 3051-3053 (2005).
14. J. M. Schmitt, and G. Kumar, "Optical scattering properties of soft tissue: a discrete particle model," *Appl Optics* **37**, 2788-2797 (1998).
15. J. R. Mourant, J. P. Freyer, A. H. Hielscher, A. A. Eick, D. Shen, and T. M. Johnson, "Mechanism of light scattering from biological cells relevant to noninvasive optical-tissue diagnostics," *Appl. Opt.* **37**, 3586-3593 (1998).
16. P. C. Waterman, "Symmetry, unitarity, and geometry in electromagnetic

- scattering," *Phys. Rev. D* **3**, 825-839 (1971).
17. M. I. Mishchenko, L. D. Travis, and A. A. Lacis, *Scattering, Absorption and Emission of light by small particles* (Cambridge, 2002).
 18. M. I. Mishchenko, "Multiple scattering, radiative transfer, and weak localization in discrete random media: unified microphysical approach," *Rev. Geophys.* **48**, doi: 10.1029/2007RG000230 (2008).
 19. M. Xu, and R. R. Alfano, "Fractal mechanisms of light scattering in biological tissue and cells," *Optics Letters* **30**, 3051-3053 (2005).
 20. C. J. R. Sheppard, "A fractal model of light scattering in biological tissue and cells," *Opt. Lett.* **32**, 142-144 (2007).
 21. N. Chemingui, "Modeling 3-D anisotropic fractal media," (Stanford University, 2001).
 22. H. Siedentopf, and R. Zsigmondy, "Über Sichtbarmachung und Größenbestimmung ultramikroskopischer Teilchen, mit besonderer Anwendung auf Goldrubingläser," *Annalen der Physik* **10**, 1-39 (1903).
 23. H. Goldman, "Spaltlampenphotographie und -photometrie," *Ophthalmologica* **98**, 257-270 (1940).
 24. D. M. Maurice, "Cellular membrane activity in the corneal endothelium of the intact eye," *Experientia* **15**, 1094-1095 (1968).
 25. C. J. Koester, "A scanning mirror microscope with optical sectioning characteristics: Applications in ophthalmology," *Appl. Opt.* **19**, 1749-1757 (1980).
 26. C. J. Koester, "Comparison of optical sectioning methods: The scanning slit confocal microscope," in *Handbook of Confocal Microscopy*, J. Pawley, ed. (Plenum Press, New York, 1990).
 27. E. H. K. Stelzer, S. Lindek, S. Albrecht, R. Pick, G. Ritter, N. J. Salmon, and R. Stricker, "A new tool for the observation of embryos and other large specimens - confocal theta-fluorescence microscopy," *J. Microsc.* **179**, 1-10 (1995).
 28. T. D. Wang, M. J. Mandella, C. H. Contag, and G. S. Kino, "Dual-axis confocal microscope for highresolution in vivo imaging," *Opt. Lett.* **28**, 414-416 (2003).
 29. A. H. Voie, D. H. Burns, and F. A. Spelman, "Orthogonal-plane fluorescence optical sectioning: threedimensional imaging of macroscopic biological specimens," *J. Microsc.* **170**, 229-236 (1993).
 30. J. Huisken, J. Swoger, F. D. Bene, J. Wittbrodt, and E. H. K. Stelzer, "Optical sectioning deep inside live embryos by selective plane illumination microscopy," *Science* **305**, 1007-1009 (2004).
 31. P. Török, C. J. R. Sheppard, and Z. Laczik, "Dark-field and differential phase contrast imaging modes in confocal microscopy using a half-aperture stop," *Optik* **103**, 101-106 (1996).
 32. P. Török, C. J. R. Sheppard, and Z. Laczik, "The effect of half-stop lateral misalignment on imaging of dark-field and stereoscopic confocal microscopes," *Appl. Opt.* **35**, 6732-6739 (1996).

33. P. J. Dwyer, and C. A. DiMarzio, "Confocal reflectance theta line scanning microscope for imaging human skin in vivo," *Opt. Lett.* **31**, 942-944 (2006).
34. P. J. Dwyer, C. A. DiMarzio, and M. Rajadhyaksha, "Confocal theta line-scanning microscope for imaging human tissues," *Appl. Opt.* **46**, 1843-1851 (2007).
35. C. Zeng, S. Vangveravong, J. Xu, K. C. Chang, R. S. Hotchkiss, K. T. Wheeler, D. Shen, Z.-P. Zhuang, H. F. Kung, and R. H. Mach, "Subcellular localization of sigma-2 receptors in breast cancer cells using two-photon and confocal microscopy," *Cancer Res.* **67**, 6708-6716 (2007).
36. J. P. Yuan, W. Zeng, M. R. Dorwart, Y. J. Choi, P. F. Worley, and S. Muallem, "SOAR and the polybasic STIM1 domains gate and regulate Orai channels," *Nature Cell Biol.* **11**, 337-343 (2009).
37. K. Fujita, M. Kobayashi, S. Kawano, M. Yamanaka, and S. Kawata, "High-resolution confocal microscopy by saturated excitation of fluorescence," *Phys. Rev. Lett.* **99**, 228105 (2007).
38. M. Yamanaka, S. Kawano, K. Fujita, N. I. Smith, and S. Kawata, "Beyond the diffraction-limit biological imaging by saturated excitation microscopy," *J. Biomed. Opt.* **13**, 050507 (2008).
39. R. S. Sayles, and T. R. Thomas, "Spatial Representation of Surface-Roughness by Means of Structure-Function - Practical Alternative to Correlation," *Wear* **42**, 263-276 (1977).

Chapter 2 Literature Review

The purpose of this chapter serves as an introduction to the relevant topics that are about to be presented and extended in the following chapters. The aim is to give the reader a quick overview of the scope of the problems. This chapter firstly reviews the conventional scattering models when light propagates through biological tissue and cells. The second review is about optical microscopy including confocal microscopy, multi-photon microscopy and 4pi microscopy, respectively. More details and past work that are attached to each specific topic are discussed at the beginning of each individual chapter.

2.1 Conventional scattering models

2.1.1 Discrete model

The scattering characteristics of the biological tissue are intimately related to the physical characteristics of particles such as size, shape, and refractive index. For homogeneous or layered spheres, the scattering properties of can be easily computed via the conventional Lorenz-Mie theory [1-2]. However, the assumption of sphericity is rarely valid in biological tissue. Furthermore, there is the overwhelming evidence that scattering properties of nonspherical particles can differ quantitatively and even qualitatively from those of volume-

or surface-equivalent spheres. To compute the scattered properties of nonspherical particles, all exact theories and numerical techniques are based on solving Maxwell's equations either analytically or numerically. The search for an exact analytical solution can be reduced to solving the vector Helmholtz equation when this equation is separable. Unfortunately, the separation of variables technique results in an analytical solution only for the few simplest cases. The solution for an isotropic homogeneous sphere was derived by Lorenz [3], Love [4], Mie [5], and Debye [6]. This solution has been extended to concentric core-mantle spheres [7], concentric multilayered spheres [8-10], radially inhomogeneous spheres [11], and optically active spheres [12]. In 1955, Wait derived a solution for electromagnetic scattering by a homogeneous, isotropic, infinite circular cylinder [13]. This solution was further extended to optically active cylinders [14] and multilayered elliptical cylinders [15]. Later on, the general solution for homogeneous, isotropic spheroids was given by Oguchi [16] and Asano and Yamamoto [17]. Indeed, the analytical solutions for the simplest finite nonspherical particles and spheroids are already very complex. Therefore, numerical solutions are always employed for complex shaped particles. Most of the numerical solutions fall into two categories: differential equation methods and integral equation methods. The differential equation methods compute the scattered field by solving the vector wave equation in the frequency or in the time domain. However, the integral equation methods are based on the volume or surface

integral counterparts of Maxwell's equations. The most commonly used numerical methods are the separation of variables method, the finite element method, the finite difference time domain method (FDTD), the point matching method, the discrete dipole approximation, the Fredholm integral equation method and the T -matrix method. The separation of variables method (SVM) for single homogenous, isotropic spheroids was pioneered by Oguchi [16] and Asano and Yamamoto [17], and then significantly improved by Voshchinnikov and Farafonov [18]. This method solves the electromagnetic scattering problem for a prolate or an oblate spheroid in the respective spheroidal coordinate system and is based on expanding the incident, internal, and scattered fields in vector spheroidal wave functions. However, for spheroids significantly larger than a wavelength or for large refractive indices, the system of linear equations becomes large and ill conditioned. Furthermore, the computation of vector spheroidal wave functions is a difficult mathematical and numerical problem, especially for absorbing particles. These factors have limited the applicability of SVM to semi-major-axis size parameters less than about 40. The obvious limitation of the method is that it is applicable only to spheroidal particles. The main advantage of SVM is that it can produce very accurate results. Furthermore, the improved version of SVM [18] is applicable to spheroids with large aspect ratios. The finite element method (FEM) is a differential equation method that computes the scattered time-harmonic electric field by solving numerically the vector

Helmholtz equation subject to boundary conditions at the particle surface [19-20]. The advantages of FEM includes that it permits the modeling of arbitrarily shaped and inhomogeneous particles, is simple in concept and execution, and avoids the singular-kernel problem. However, FEM computations are spread over the entire computational domain rather than confined to the scatterer itself. This tends to make FEM computations rather time consuming and limited to size parameters less than about 10. The FDTD calculates electromagnetic scattering in the time domain by directly solving Maxwell's time-dependent curl equations [21-24]. As in FEM, the scattering particle is embedded in a finite computational domain, and absorbing boundary conditions are employed to model scattering in the open space [25-27]. The FDTD has the advantages of conceptual simplicity and ease of implementation. The limitation lies in the accuracy, computational complexity, size parameter range, and the need to repeat all computations with changing direction of illumination. In the point matching method (PMM), the fields are matched at as many points on the surface as there exist unknown expansion coefficients [16]. However, the validity of this method is questionable and depends on the applicability of the Rayleigh hypothesis, that is, the assumption that the scattered field can be accurately expanded in the outgoing spherical waves in the region enclosed between the particle surface and the smallest circumscribing sphere [28-29]. This problem is ameliorated in the generalized PMM (GPMM) by forming an overdetermined system of

equations for the unknown expansion coefficients [30-32]. The discrete dipole approximation (DDA) is based on partitioning a particle into dipoles [33]. The electromagnetic response of the dipoles to the local electric field is assumed to be known. The field exciting a dipole is a superposition of the external field and the fields scattered by all other dipoles. The most important advantage of DDA is its applicability to arbitrarily shaped, inhomogeneous, and anisotropic particles. The limitations lie in numerical accuracy, especially for scattering matrix elements, low convergence of results with increasing of number of dipoles, and the need to repeat the entire calculation for each new direction of incidence. The scattered field obtained with the Fredholm integral equation method (FIEM) satisfies a variational principle, and is claimed to be numerically stable and convergent to the exact result even for particles with large aspect ratios [34]. The major limitation of FIEM is that the matrix elements must be evaluated analytically, thereby leading to different programs for each scatterer, and restricting computations to only a few model shapes such as spheroids, triaxial ellipsoids, and finite circular cylinders [34-36]. The *T*-matrix method (TMM) is based on expanding the incident field in vector spherical wave functions regular at the origin and expanding the scattered field outside a circumscribing sphere of the scatterer in vector spherical wave functions at infinity. TMM was first introduced by Waterman [37] for single homogeneous scatterers and was then generalized to multilayered scatterers and arbitrary clusters of nonspherical particles [38-39] and to nonspherical

chiral scatterers [40]. Mishchenko [41] developed an analytical orientation-averaging T -matrix procedure that makes computations for randomly oriented, rotationally symmetric particles as fast as those for a particle in a fixed orientation. This procedure has been further extended to arbitrary clusters of spheres [42]. The main drawback of TMM is the loss of efficiency for particles with large aspect ratios or with shapes lacking axial symmetry. The advantages of TMM are the highly accuracy, fast computational speed, and independency of the incident and scattered fields.

2.1.2 Fractal model

A fractal is a shape made of parts similar to the whole in some way.

In 1990, Falconer [43] gave a descriptive definition of a fractal:

A set F is fractal, which has the properties as follows: (a) F has a fine structure, i.e. detail on arbitrarily small scales. (b) F is too irregular to be described in traditional geometrical language, both locally and globally. (c) Often F has some form of self-similarity, perhaps approximate or statistical. (d) Usually, the “fractal dimension” of F is greater than its topological dimension. (e) In most cases of interest F is defined in a very simple way, perhaps recursively.

Mandelbrot [44] proposed to use a fractal dimension to characterize the logarithmic rate of the increase of perimeters to the decrease of size. The fractal dimension D_f can be determined by the relation,

$$\eta(a) = \eta_0 a^{3-D_f}, \quad (2.2)$$

where $\eta(a)$ is the volume fraction of the particles, η_0 is a constant. Fractals are functions which are continuous but not differentiable. They possess the property of self-similarity, that is they appear the same at any scale of magnification. There are generally two types of fractal: self-similarity fractals and self-affine fractals. Self-similarity fractals can be completely characterized by a single parameter, the fractal dimension D_f . Self-affine fractals are single-valued. When the scale of observation is changed, a scaling factor with dimensions of length must be introduced to restore the appearance of self-similarity. Therefore, the difference between self-similarity fractals and self-affine fractals are:

- ◆ Self-similarity fractals can be completely characterized by the fractal dimension D_f , while
- ◆ Self-affine fractals must be characterized by both the fractal dimension D_f and the scaling factor Λ .

Fractal dimensions may vary between the theoretical limits of 1 (a straight line) and 2 (a space-filling curve), while topographies may be represented by very short lengths. In practice, no real surface can be fractal over an infinite range of wavelengths. A real surface will be formed by several different processes each with its characteristic features – a multifractal. It typically will present a structure function as two or more straight lines of different slope, meeting at a more or less sharp discontinuity. In 1986, a combined correlation

function, including non-fractal short range order and long range fractal correlations was designed to model aggregated gold colloids [45]. In reality, objects can be scaled-invariant only over a limited range, and an understanding of the bounds of the fractal regime is crucial in the development of a complete picture, not only of aggregates, but of fractal objects in general. The properties of self-similarity and self-affine fractals were discussed by Sinha in 1989 [46]. The Weierstrass-Mandelbrot (W-M) fractal function was used by Majumdar to describe roughness characterization, which was assumed to be homogenous and isotropic [47]. W-M fractal function satisfies the properties of continuity, non-differentiability and self-affinity, and is therefore used to characterize and simulate such profiles. The W-M function has a fractal dimension D_f , between 1 and 2. Fractal aggregates made of identical spherical particles were estimated by several three dimensional off-lattice cluster-cluster algorithm by Hasmy in 1993 [48]. The structure function, characterized by a fractal dimension and the topography was used to describe and characterize anisotropy of rough surface [49]. The fractal dimension of an isotropic surface is well established to be $1 +$ the fractal dimension of any profile through the surface. For a weakly anisotropic surface, the fractal dimension of a profile will be independent of the angle of measurement, but the topography will change [50]. For a strongly anisotropic surface, both fractal dimension and topography will change; the fractal dimension along the lay will be less than that across the lay [51]. Davies and Hall predict that for a strongly

anisotropic surface, the fractal dimension will be the same in all angular directions except along the lay, where it will decrease [52]. In 2000, Filippov *et al.* described the results of numerical simulations of the mass or energy transfer between the gas and the fractal-like aggregates of N spherical particles in either the free molecular or continuum regime, as well as the light scattering properties of random fractal-like aggregates, based on Rayleigh-Debye-Gans (RDG) theory [53]. In 2003, Ortiz *et al.* introduced a multi-resolution hierarchical algorithm, which allows the study of large systems taking fully into account the long range of the interactions in multiple scattering calculations, to study the scaling properties of the light scattered by colloidal aggregates [54]. By using a probabilistic convolution model, Kolvin and Oleschko suggested that for an extended fractal medium with strong scattering cross-section, multiple scattering can affect the value of the fractal dimension estimated from the wave-field's Fourier power spectrum [55]. In 2005, Xu and Alfano [56] used the fractal continuous random media to model visible and near-infrared light scattering by biological tissue and cell suspensions, which indicated great implications for spectroscopic tissue diagnosis. Later on, Sheppard [57] employed the K distribution to extend the applicable scale of the correlation function to a sub-fractal regime.

2.2 Optical microscopy

2.2.1 Confocal microscopy

The confocal principle was first described by Minsky [58]. Based on a conventional microscopy, a very small pinhole is introduced into the system to cut off the light from the background [59-60]. The system scans a diffraction-limited spot of light and builds up the image point by point. The essential setup can be made by some mechanism for scanning the light beam relative to the specimen and appropriate photodetectors to collect the light reflected or transmitted from the specimen [61]. Because of the application of very small pinholes, out-focus light is dramatically reduced, thus allowing the confocal microscope to image the specimen section-by-section along the axis [58-63]. This optical sectioning property of confocal microscopy is considered as one of the most significant advantages over conventional microscopy, and three dimensional images can be built up from these sections each consisting of a two dimensional image. With these exciting advantages, confocal microscopy is studied widely both theoretically and experimentally. In 1979, Brakenhoff *et al.* [64] had demonstrated the optical sectioning effect experimentally with microscope objectives of the highest available numerical aperture, of the type used in cell biology, and also verified the prediction that the resolution is improved relative to the non-confocal microscope by a factor of the square root of 2, i.e. 1.414. After that, a long series of confocal

microscopes, stretching from Minsky's prototype to the scanning optical microscope system supplied commercially in Wijnaents van Resandt and Stelzer [65], relied on moving the entire specimen and its supporting stage in two directions in raster fashion relative to stationary optics. However, these microscopes were too slow and vibration sensitive to be convenient for biology. Cox then managed to obtain confocal images of cells stained with fluorescein, but the image improvements over conventional epifluorescence were unconvincing [66]. The first biologically convincing results with fluorescence confocal scanning microscopy were obtained in 1985 [67]. The confocal microscopy not only shows its super-resolution in the axial direction but also achieves better resolution in the transverse direction compared with a conventional microscope. The improvements of resolution can be simply explained by a principle given by Lukosz [68], which states that resolution can be increased at the expense of field of view. In 1971, Sheppard and Choudhury studied the point spread function and two dimensional in-focus transfer function of coherent confocal microscopy [69]. For weak scattering objects, the three dimensional transfer functions, which is the Fourier transform of the point spread function, can be used to completely describe the image formation in confocal microscope. The depth of field, which is one of the most significant features, was investigated in 1977 [62]. The two dimensional transfer functions were extended to the defocused case in 1978 [70] and to the three dimensional transfer function in 1991 [71]. The size of

pinhole is crucial not only in transverse and axial resolutions, but also in signal strength and signal to background ratio. The study on the effects of the pinhole size was given by Wilson *et al.* [72] and Cox and Sheppard [73]. The scanning slit confocal microscope with D-shaped apertures was developed for ophthalmological applications by Goldman [74], Maurice [75], and Koester [76-77]. Török *et al.* employed D-shaped apertures to achieve dark-field imaging [78]. Later, they further investigated using D-shaped apertures to achieve both dark-field and differential phase contrast imaging [79]. Dwyer *et al.* successfully applied the confocal scanning microscope with D-shaped apertures to imaging nuclear and cellular details in human epidermis *in vivo* [80-81]. The wide applicability of this geometry stems from the fact that the illumination and detection beams overlap only in the focal region, resulting in angular gating and thus improving rejection of scattered light [82]. Later, Barbastathis introduced holographic techniques into confocal microscopy [83].

2. 2. 2 Multi-photon microscopy

The invention of two-photon fluorescence light microscopy by Denk, Webb and co-workers revolutionized three-dimensional (3D) *in vivo* imaging of cells and tissues [84]. Two-photon excitation microscopy (2PM) and other nonlinear optical techniques constitute one of the most promising and fastest-growing areas in biological and medical imaging at the optical resolution level [69, 85-88]. In particular, 2PM belongs to a class of imaging

techniques that allow observation of biological specimens in conditions very close to their natural environment, increasing the possibility of understanding the complex and delicate relationship existing between structure and function [89]. Moreover, with few exceptions biological tissues strongly scatter light, making high-resolution deep imaging impossible for traditional—including confocal—fluorescence microscopy. Nonlinear optical microscopy, in particular 2PM, has overcome this limitation, providing large depth penetration mainly because even multiply scattered signal photons can be assigned to their origin as the result of localized nonlinear signal generation. Two-photon microscopy thus allows cellular imaging several hundred microns deep in biological samples, including lymphatic organs [90-91], kidney [92], heart [93], skin [94] and brain [95-96].

All 2PMs requires expensive pulsed laser systems to achieve sufficient excitation rates. Two major advantages make the investment worthwhile. First, because multiple excitation photons combine their quantum energies in nonlinear microscopy, the photons generated (or the transitions excited) have higher energies than the excitation light making emission 'bluer' than the excitation, which is different from traditional fluorescence. For commonly used fluorescent markers, multiphoton absorption occurs in the near-infrared wavelength range (700–1,000 nm), whereas emission occurs in the visible spectral range. Near-infrared light not only penetrates deeper into scattering

tissue but is also generally less phototoxic owing to the lack of significant endogenous (one-photon) absorbers in most tissues [97].

The second major advantage of two-photon absorption and, in fact, of all nonlinear contrast mechanisms, is that the signal depends supralinearly on the density of photons, that is, the light intensity. As a consequence, when focusing the laser beam through a microscope objective, multiphoton absorption is spatially confined to the perifocal region. The absence of multiphoton absorption in out-of-focus planes contrasts with confocal microscopy, where (single-photon) absorption occurs within the entire excitation light cone. The lack of out-of-focus excitation in nonlinear microscopy further reduces photodamage and thus increases tissue viability, which is crucial for long-term imaging [98]. Localization of excitation also provides excitation-based three-dimensional resolution with no need for spatially resolved detection through a confocal pinhole. By the same token, multiphoton absorption allows highly localized photomanipulations, such as photobleaching and photolytic release of caged compounds, within femtoliter volumes [98-99], which, however, is beyond the scope of this review.

Localization of excitation is maintained even in strongly scattering tissue because the density of scattered excitation photons generally is too low to generate significant signal, making nonlinear microscopy far less sensitive to light scattering than traditional microscopy. This is of paramount importance for deep imaging, because it means that all fluorescence photons are known to

originate from near the focus and thus can provide useful signal. The best detection strategy therefore becomes: collect as many photons as possible, wherever they seem to come from, but look at their color. Scattering does, however, increase the spatioangular range (the phase space) within which fluorescence light emerges from the tissue so that special detection optics is needed to optimize fluorescence collection from deep foci.

2. 2. 3 4Pi microscopy

In 1978, Christoph Cremer and Thomas Cremer proposed the creation of a perfect hologram, i.e. that carries the whole field information of the emission of a point source in all directions, a so-called 4pi hologram [100]. The first description of a practicable system of 4Pi microscopy, i.e. the setup with two opposing, interfering lenses, was invented by Stefan Hell in 1990 [101]. The experimental analysis was followed in 1994 [102]. The improvements in resolution are achieved by using two opposing objective lenses which both are focused to the same geometrical location. The difference in optical path length through each of the two objective lenses is carefully aligned to be minimal. By this, molecules residing in the common focal area of both objectives can be illuminated coherently from both sides and also the reflected or emitted light can be collected coherently, i.e. coherent superposition of emitted light on the detector is possible. The solid angle that is used for illumination and detection is increased and approaches the ideal case. In this ideal case, the sample is

illuminated and detected from all sides simultaneously. In any confocal arrangement, the point spread function of the microscope is the product of the illumination and detection point spread functions. Consequently, combining the 4Pi method with the confocal principle leads to several possible hybrid microscopies, which can be given as following:

- Type A: 4Pi illumination and conventional detection
- Type B: Conventional illumination and 4Pi detection
- Type C: 4Pi illumination and 4Pi detection

The three-dimensional imaging properties of 4Pi microscopy, based on a scalar theory, have been described in a few papers [103-104]. The point spread functions for the vectorial case with plane polarized light were given by Hell and Stelzer [105-107].

References

1. W. J. Wiscombe, "Improved Mie Scattering Algorithms," *Appl Optics* **19**, 1505-1509 (1980).
2. Z. Kam, "Absorption and Scattering of Light by Small Particles - Bohren,C, Huffman,Dr," *Nature* **306**, 625-625 (1983).
3. L. V. Lorentz, "Upon the light reflected and refracted by a transparent sphere," *Vid. Selsk. Skrift* **6**, 1 (1890).
4. A. E. H. Love, "The scattering of electric wave by a dielectric sphere," *Proc. Lond. Math. Soc.* **30** (1899).
5. G. Mie, "Articles on the optical characteristics of turbid tubes, especially colloidal metal solutions.," *Annalen der Physik* **25**, 377-445 (1908).
6. P. Debye, "The heliograph of spheres of any material," *Annalen der Physik* **30**, 57-136 (1909).
7. A. L. Aden, and M. Kerker, "Scattering of Electromagnetic Waves from 2 Concentric Spheres," *J Appl Phys* **22**, 1242-1246 (1951).
8. J. R. Wait, "Mode Theory of Vlf Radio Propagation for a Spherical Earth and a Concentric Anisotropic Ionosphere," *Can J Phys* **41**, 299-& (1963).
9. P. W. Mikulski, "On Efficiency of Optimal Nonparametric Procedures in 2 Sample Case," *Ann Math Stat* **34**, 22-& (1963).
10. R. Bhandari, "Analytic Expressions, Computational Forms for Scattering by a Multilayered Sphere," *P Soc Photo-Opt Inst* **540**, 500-511 (1985).
11. P. J. Wyatt, "Scattering of Electromagnetic Plane Waves from Inhomogeneous Spherically Symmetric Objects," *Phys Rev* **127**, 1837-& (1962).
12. C. F. Bohren, "Light-Scattering by an Optically-Active Sphere," *Chem Phys Lett* **29**, 458-462 (1974).
13. J. R. Wait, "Scattering of a Plane Wave from a Circular Dielectric Cylinder at Oblique Incidence," *Can J Phys* **33**, 189-195 (1955).
14. C. F. Bohren, "Scattering of Electromagnetic-Waves by an Optically-Active Cylinder," *J Colloid Interf Sci* **66**, 105-109 (1978).
15. C. S. Kim, and C. Yeh, "Scattering of an Obliquely Incident Wave by a Multilayered Elliptic Lossy Dielectric Cylinder," *Radio Sci* **26**, 1165-1176 (1991).
16. T. Oguchi, "Attenuation and Phase Rotation of Radio-Waves Due to Rain - Calculations at 19.3 and 34.8 Ghz," *Radio Sci* **8**, 31-38 (1973).
17. S. Asano, and G. Yamamoto, "Light-Scattering by a Spheroidal Particle," *Appl Optics* **14**, 29-49 (1975).
18. N. V. Voshchinnikov, and V. G. Farafonov, "Optical-Properties of Spheroidal Particles," *Astrophys Space Sci* **204**, 19-86 (1993).
19. M. A. Morgan, and K. K. Mei, "Finite-Element Computation of Scattering by Inhomogeneous Penetrable Bodies of Revolution," *Ieee T Antenn Propag*

- 27, 202-214 (1979).
20. P. P. Silvester, and R. L. Ferrari, *Finite elements for electrical engineers* (Press Syndicate of the University of Cambridge, Cambridge, 1996).
21. K. S. Yee, "Numerical Solution of Initial Boundary Value Problems Involving Maxwells Equations in Isotropic Media," *Ieee T Antenn Propag* **Ap14**, 302-& (1966).
22. K. S. Kunz, and R. J. Luebbers, *The Finite difference time domain method for electromagnetics* (CRC Press, 1993).
23. E. Vasilyeva, and A. Taflove, "Three-dimensional modeling of amplitude-object imaging in scanning near-field optical microscopy," *Opt Lett* **23**, 1155-1157 (1998).
24. A. Taflove, and S. C. Hagness, *Computational electrodynamics: the finite-differnce time-domain method* (Artech House, 1995).
25. J. P. Berenger, "Perfectly matched layer for the FDTD solution of wave-structure interaction problems," *Ieee T Antenn Propag* **44**, 110-117 (1996).
26. M. J. Grote, and J. B. Keller, "Nonreflecting boundary conditions for Maxwell's equations," *J Comput Phys* **139**, 327-342 (1998).
27. P. Yang, and K. N. Liou, "An efficient algorithm for truncating spatial domain in modeling light scattering by finite-difference technique," *J Comput Phys* **140**, 346-369 (1998).
28. R. F. Millar, "Rayleigh Hypothesis and a Related Least-Squares Solution to Scattering Problems for Periodic Surfaces and Other Scatterers," *Radio Sci* **8**, 785-796 (1973).
29. L. Lewin, "Restricted Validity of Point-Matching Techniques," *Ieee T Microw Theory* **Mt18**, 1041-& (1970).
30. J. A. Morrison, and M. J. Cross, "Scattering of a Plane Electromagnetic-Wave by Axisymmetric Raindrops," *Bell Syst Tech J* **53**, 955-1019 (1974).
31. T. Oguchi, and Y. Hosoya, "Scattering Properties of Oblate Raindrops and Cross Polarization of Radio-Waves Due to Rain .2. Calculations at Microwave and Millimeter Wave Regions," *J Radio Res Lab* **21**, 191-259 (1974).
32. H. M. Alrizzo, and J. M. Tranquilla, "Electromagnetic Scattering from Dielectrically Coated Axisymmetrical Objects Using the Generalized Point-Matching Technique .1. Theoretical Formulation," *J Comput Phys* **119**, 342-355 (1995).
33. E. M. Purcell, and Pennypac.Cr, "Scattering and Absorption of Light by Nonspherical Dielectric Grains," *Astrophys J* **186**, 705-714 (1973).
34. A. R. Holt, N. K. Uzunoglu, and B. G. Evans, "Integral-Equation Solution to Scattering of Electromagnetic-Radiation by Dielectric Spheroids and Ellipsoids," *Ieee T Antenn Propag* **26**, 706-712 (1978).
35. B. G. Evans, and A. R. Holt, "Scattering-Amplitudes and Cross-Polarization of Ice Particles," *Electron Lett* **13**, 342-344 (1977).
36. A. R. Holt, and J. W. Shepherd, "Electromagnetic Scattering by Dielectric

- Spheroids in the Forward and Backward Directions," J Phys a-Math Gen **12**, 159-166 (1979).
37. P. C. Waterman, "Symmetry, unitarity, and geometry in electromagnetic scattering," Phys. Rev. D **3**, 825-839 (1971).
 38. B. Peterson, and S. Strom, "T Matrix for Electromagnetic Scattering from an Arbitrary Number of Scatterers and Representations of E(3)," Phys Rev D **8**, 3661-3678 (1973).
 39. S. Strom, "T-Matrix for Electromagnetic Scattering from an Arbitrary Number of Scatterers with Continuously Varying Electromagnetic Properties," Phys Rev D **10**, 2685-2690 (1974).
 40. A. Lakhtakia, V. K. Varadan, and V. V. Varadan, "Scattering and Absorption Characteristics of Lossy Dielectric, Chiral, Nonspherical Objects," Appl Optics **24**, 4146-4154 (1985).
 41. M. I. Mishchenko, "Light-Scattering by Randomly Oriented Axially Symmetrical Particles," J Opt Soc Am A **8**, 871-882 (1991).
 42. D. W. Mackowski, and M. I. Mishchenko, "Calculation of the T matrix and the scattering matrix for ensembles of spheres," J Opt Soc Am A **13**, 2266-2278 (1996).
 43. K. J. Falconer, "On a Problem of Erdos on Fractal Combinatorial Geometry," J Comb Theory A **59**, 142-148 (1992).
 44. B. B. Mandelbrot, *Fractals: Form, Chance and Dimension* (Freeman, San Francisco, 1977).
 45. P. Dimon, S. K. Sinha, D. A. Weitz, C. R. Safinya, G. S. Smith, W. A. Varady, and H. M. Lindsay, "Structure of Aggregated Gold Colloids," Phys Rev Lett **57**, 595-598 (1986).
 46. S. K. Sinha, "Scattering from Fractal Structures," Physica D **38**, 310-314 (1989).
 47. A. Majumdar, and C. L. Tien, "Fractal Characterization and Simulation of Rough Surfaces," Wear **136**, 313-327 (1990).
 48. A. Hasmy, M. Foret, J. Pelous, and R. Jullien, "Small-Angle Neutron-Scattering Investigation of Short-Range Correlations in Fractal Aerogels - Simulations and Experiments," Phys Rev B **48**, 9345-9353 (1993).
 49. T. R. Thomas, B. G. Rosen, and N. Amini, "Fractal characterisation of the anisotropy of rough surfaces," Wear **232**, 41-50 (1999).
 50. J. C. Russ, *Fractal Surfaces* (Plenum, New York, 1994).
 51. T. R. Thomas, and A. P. Thomas, "Fractals and engineering surface roughness," Surface Topography **1**, 1 (1988).
 52. S. Davies, and P. Hall, "Fractal analysis of surface roughness by using spatial data," J Roy Stat Soc B **61**, 3-29 (1999).
 53. A. V. Filippov, M. Zurita, and D. E. Rosner, "Fractal-like aggregates: Relation between morphology and physical properties," J Colloid Interf Sci **229**, 261-273 (2000).
 54. G. P. Ortiz, and W. L. Mochan, "Scaling condition for multiple scattering in fractal aggregates," Physica B **338**, 103-106 (2003).

55. G. Korvin, and K. Oleschko, "Multiple wave scattering from fractal aggregates," *Chaos Soliton Fract* **19**, 421-425 (2004).
56. M. Xu, and R. R. Alfano, "Fractal mechanisms of light scattering in biological tissue and cells," *Opt. Lett.* **30**, 3051-3053 (2005).
57. C. J. R. Sheppard, "A fractal model of light scattering in biological tissue and cells," *Opt. Lett.* **32**, 142-144 (2007).
58. M. Minsky, "Microscopy Apparatus," (1957).
59. Mccutche.Cw, "Superresolution in Microscopy and Abbe Resolution Limit," *J Opt Soc Am* **57**, 1190-& (1967).
60. E. A. Ash, and G. Nicholls, "Super-Resolution Aperture Scanning Microscope," *Nature* **237**, 510-& (1972).
61. T. Wilson, and C. J. R. Sheppard, *Theory and Practice of Scanning Optical Microscopy* (Academic, London, 1984).
62. C. J. R. Sheppard, and T. Wilson, "Depth of field in the scanning microscope," *Opt. Lett.* **3**, 115-117 (1978).
63. D. K. Hamilton, T. Wilson, and C. J. R. Sheppard, "Experimental-Observations of the Depth-Discrimination Properties of Scanning Microscopes," *Opt Lett* **6**, 625-626 (1981).
64. G. J. Brakenhoff, P. Blom, and P. Barends, "Confocal Scanning Light-Microscopy with High Aperture Immersion Lenses," *J Microsc-Oxford* **117**, 219-232 (1979).
65. R. W. W. Vanresandt, H. J. B. Marsman, R. Kaplan, J. Davoust, E. H. K. Stelzer, and R. Stricker, "Optical Fluorescence Microscopy in 3 Dimensions - Microtomoscopy," *J Microsc-Oxford* **138**, 29-34 (1985).
66. I. J. Cox, "Scanning Optical Fluorescence Microscopy," *J Microsc-Oxford* **133**, 149-154 (1984).
67. G. J. Brakenhoff, H. T. M. Vandervoort, E. A. Vanspronsen, W. A. M. Linnemans, and N. Nanninga, "3-Dimensional Chromatin Distribution in Neuro-Blastoma Nuclei Shown by Confocal Scanning Laser Microscopy," *Nature* **317**, 748-749 (1985).
68. W. Lukosz, "Optical Systems with Resolving Powers Exceeding Classical Limit," *J Opt Soc Am* **56**, 1463-& (1966).
69. C. J. R. Sheppard, and M. Gu, "Imaging formation in two-photon fluorescence microscopy," *Optik* **86**, 104-106 (1990).
70. C. J. R. Sheppard, D. K. Hamilton, and I. J. Cox, "Optical Microscopy with Extended Depth of Field," *P Roy Soc Lond a Mat* **387**, 171-& (1983).
71. C. J. R. Sheppard, M. Gu, and X. Q. Mao, "Three-dimensional coherent transfer function in a reflection-mode confocal scanning microscope," *Optics Comm.* **81**, 281-284 (1991).
72. T. Wilson, and A. R. Carlini, "3-Dimensional Imaging in Confocal Imaging-Systems with Finite Sized Detectors," *J Microsc-Oxford* **149**, 51-66 (1988).
73. I. J. Cox, and C. J. R. Sheppard, "Information Capacity and Resolution in an Optical-System," *J Opt Soc Am A* **3**, 1152-1158 (1986).

74. H. Goldman, "Spaltlampenphotographie und -photometrie," *Ophthalmologica* **98**, 257-270 (1940).
75. D. M. Maurice, "Cellular membrane activity in the corneal endothelium of the intact eye," *Experientia* **15**, 1094-1095 (1968).
76. C. J. Koester, "A scanning mirror microscope with optical sectioning characteristics: Applications in ophthalmology," *Appl. Opt.* **19**, 1749-1757 (1980).
77. C. J. Koester, "Comparison of optical sectioning methods: The scanning slit confocal microscope," in *Handbook of Confocal Microscopy*, J. Pawley, ed. (Plenum Press, New York, 1990).
78. P. Török, C. J. R. Sheppard, and Z. Laczik, "The effect of half-stop lateral misalignment on imaging of dark-field and stereoscopic confocal microscopes," *Appl. Opt.* **35**, 6732-6739 (1996).
79. P. Török, C. J. R. Sheppard, and Z. Laczik, "Dark-field and differential phase contrast imaging modes in confocal microscopy using a half-aperture stop," *Optik* **103**, 101-106 (1996).
80. P. J. Dwyer, and C. A. DiMarzio, "Confocal reflectance theta line scanning microscope for imaging human skin in vivo," *Opt. Lett.* **31**, 942-944 (2006).
81. P. J. Dwyer, C. A. DiMarzio, and M. Rajadhyaksha, "Confocal theta line-scanning microscope for imaging human tissues," *Appl. Opt.* **46**, 1843-1851 (2007).
82. C. J. R. Sheppard, W. Gong, and K. Si, "The divided aperture technique for microscopy through scattering media," *Opt Express* **16**, 17031-17038 (2008).
83. G. Barbastathis, M. Balberg, and D. J. Brady, "Confocal microscopy with a volume holographic filter," *Optics Letters* **24**, 811-813 (1999).
84. W. Denk, J. H. Strickler, and W. W. Webb, "Two-photon laser scanning fluorescence microscopy," *Science* **248**, 73-76 (1990).
85. J. B. Pawley, *Handbook of biological confocal microscopy* (Springer, New York, NY, 2006).
86. S. W. Hell, K. Bahlmann, M. Schrader, A. Soini, H. Malak, I. Gryczynski, and J. R. Lakowicz, "Three-photon excitation in fluorescence microscopy," *J. Biomed. Opt.* **1**, 71-74 (1996).
87. P. T. C. So, "Two-photon fluorescence microscopy: A new tool for tissue imaging and spectroscopy," *J Histotechnol* **23**, 221-228 (2000).
88. P. T. C. So, C. Y. Dong, B. R. Masters, and K. M. Berland, "Two-photon excitation fluorescence microscopy," *Annu Rev Biomed Eng* **2**, 399-429 (2000).
89. W. Carring, *Imaging live cells in 3D using wide-field microscopy with imaging restoration In: Confocal and Two-photon Microscopy; Foundations, Applications and Advances* (New York: Wiley-Liss, 2002).
90. M. D. Cahalan, I. Parker, S. H. Wei, and M. J. Miller, "Real-time imaging of lymphocytes in vivo," *Curr Opin Immunol* **15**, 372-377 (2003).

91. P. Bousso, and E. A. Robey, "Dynamic behavior of T cells and thymocytes in lymphoid organs as revealed by two-photon microscopy," *Immunity* **21**, 349-355 (2004).
92. B. A. Molitoris, and R. M. Sandoval, "Intravital multiphoton microscopy of dynamic renal processes," *Am J Physiol-Renal* **288**, F1084-F1089 (2005).
93. M. Rubart, "Two-photon microscopy of cells and tissue," *Circ Res* **95**, 1154-1166 (2004).
94. L. H. Laiho, S. Pelet, T. M. Hancewicz, P. D. Kaplan, and P. T. C. So, "Two-photon 3-D mapping of ex vivo human skin endogenous fluorescence species based on fluorescence emission spectra," *J Biomed Opt* **10**, - (2005).
95. W. Denk, and K. Svoboda, "Photon upmanship: Why multiphoton imaging is more than a gimmick," *Neuron* **18**, 351-357 (1997).
96. F. Helmchen, and W. Denk, "New developments in multiphoton microscopy," *Curr Opin Neurobiol* **12**, 593-601 (2002).
97. K. Svoboda, and S. M. Block, "Biological Applications of Optical Forces," *Annu Rev Bioph Biom* **23**, 247-285 (1994).
98. J. M. Squirrell, D. L. Wokosin, J. G. White, and B. D. Bavister, "Long-term two-photon fluorescence imaging of mammalian embryos without compromising viability," *Nat Biotechnol* **17**, 763-767 (1999).
99. K. Svoboda, D. W. Tank, and W. Denk, "Direct measurement of coupling between dendritic spines and shafts," *Science* **272**, 716-719 (1996).
100. C. Cremer, and T. Cremer, "Considerations on a Laser-Scanning-Microscope with High-Resolution and Depth of Field," *Microsc Acta* **81**, 31-44 (1978).
101. S. W. Hell, "Double-scanning microscope," (1990).
102. S. W. Hell, E. H. K. Stelzer, S. Lindek, and C. Cremer, "Confocal Microscopy with an Increased Detection Aperture - Type-B 4pi Confocal Microscopy," *Opt Lett* **19**, 222-224 (1994).
103. M. Gu, and C. J. R. Sheppard, "3-Dimensional Transfer-Functions in 4pi Confocal Microscopes," *J Opt Soc Am A* **11**, 1619-1627 (1994).
104. M. Gu, and C. J. R. Sheppard, "Optical Transfer-Function Analysis for 2-Photon 4pi Confocal Fluorescence Microscopy," *Opt Commun* **114**, 45-49 (1995).
105. S. W. Hell, S. Lindek, and E. H. K. Stelzer, "Enhancing the Axial Resolution in Far-Field Light-Microscopy - 2-Photon 4pi Confocal Fluorescence Microscopy," *J Mod Optic* **41**, 675-681 (1994).
106. S. Hell, and E. H. K. Stelzer, "Fundamental Improvement of Resolution with a 4pi-Confocal Fluorescence Microscope Using 2-Photon Excitation," *Opt Commun* **93**, 277-282 (1992).
107. S. Hell, and E. H. K. Stelzer, "Properties of a 4pi Confocal Fluorescence Microscope," *J Opt Soc Am A* **9**, 2159-2166 (1992).

Chapter 3 Modeling optical properties in biological tissue

3.1 Introduction

The optical properties of tissue and cells are of key significance in optical biomedical technology, such as in optical imaging and spectroscopy. Currently, for the simplicity of computation, most of the preliminary studies were proposed based on the three assumptions that the scatterers in biological tissue and cells are homogeneous, isotropic and smooth [1-3]. However, microstructure in biological tissue and cells can consist of different types of particles having arbitrary shapes, size distributions [4], and orientations, as well as an overall mass density that varies spatially within them. Besides, the optical properties of real tissue differ much from the theoretical homogeneously distributed smooth spherical particles. Therefore, creating an appropriate model for light scattering by biological tissue and cells is important not only for theoretical interest but also for practical reasons. In this chapter, two models are proposed. In section 3.2, we extend a discrete model based on rough surface nonspherical particles from biological tissue to cells. Section 3.3 introduces a fractal model based on the structure function.

3.2 Discrete model with rough surface nonspherical particles

Recently, we introduced a method based on random nonspherical particles to study tissue optical properties [5]. In a previous paper, we proposed to use slightly rough surface cylinders to model fresh mouse muscle, since the sample is cut in a cross-sectional direction. Theoretical analyses based on the T -matrix method were carried out, showing interesting results summarized as follows: (i) In the exact forward scattering region, the nonspherical and spherical model display only slight differences. In other words, the phase function for biological tissue is insensitive to particle nonsphericity in the exact forward scattering region. (ii) In both side and back scattering regions, the nonspherical model can describe the phase functions better than the spherical model.

To analyze light scattering in biological tissue with randomly non-spherical rough-surface particles, an appropriate approach is needed to explicitly describe the shape of the particles. According to our previous work [5], the shape of the particles is approximately determined by the shape parameter K , the variance τ , and the center point of the “display window” (denoted as “ CP ”), while the roughness of the particle is determined by the roughness parameter σ . Changing the values of K , τ and CP , a variety of random rough surface particles can be obtained, including rough surface spherical, cylindrical, prolate and oblate particles. The scattering properties of

biological tissue and cells [6] are modeled using slightly rough particles, with size not too large compared with the incident wavelength. Therefore, a small value of σ is selected to represent slightly rough surfaces. ε is the aspect ratio of the maximum-to-minimum particle dimensions for a spheroid, or is the diameter-to-length ratio (D/L) for a cylinder.

The basic quantities that fully describe the scattering process are the ensemble-averaged extinction C_{ext} and scattering C_{sca} cross-section and the elements of the so-called normalized Stokes scattering matrix $S(\theta)$ given by [7]:

$$S(\theta) = \begin{bmatrix} P(\theta) & b_1(\theta) & 0 & 0 \\ b_1(\theta) & a_2(\theta) & 0 & 0 \\ 0 & 0 & a_3(\theta) & b_2(\theta) \\ 0 & 0 & -b_2(\theta) & a_4(\theta) \end{bmatrix}. \quad (3.1)$$

Here, $\theta \in [0^\circ, 180^\circ]$ is the scattering angle. The well-known block-diagonal structure of this matrix is confirmed by the T -matrix results and is mainly caused by averaging over the uniform orientation distribution of a multi-particle group coupled with sufficient randomness of particle positions. The (1,1) element $P(\theta)$, which is called the phase function, is an important quantity used to describe the angular distribution of the scattered intensity. Traditionally, the phase function has been calculated directly for a large set of scattering angles, which causes an unbearable computation time. To accelerate the T -matrix technique, the phase function is explicitly represented as a Legendre polynomial expansion [8]:

$$P(\theta) = \sum_{i=0}^{i_{\max}} \omega_i P_i(\cos \theta), \quad (3.2)$$

where $P_i(\cos \theta)$ are Legendre polynomials, the value of the upper summation limit i_{\max} determines on the desired numerical accuracy of computations, and ω_i is the ensemble-average expansion coefficient which can be calculated with T -matrix method [9]:

$$\omega_i = \frac{1}{MC_{sca}} \sum_{m=1}^M \sum_{n=1}^N f'(r_n) \omega_i(r_n) C_{sca}^m(r_n) w_n, \quad (3.3)$$

where $f'(r)$ is the size distribution function, and r is the radius for spherical particles or radius of the equal-projected-area sphere for nonspherical particles, C_{sca} is the scattering cross section, the index $m=1, \dots, M$ numbers the aspect ratios, and r_n and w_n ($n=1, \dots, N$) are quadrature division points and weights, respectively.

The anisotropy factor, which is the mean cosine of the scattering angle, used to measure the scattering retained in the forward direction following a scattering event [6], can be expressed as:

$$g = \int \mu P(\theta) d\Omega / \int P(\theta) d\Omega, \quad (3.4)$$

where $\mu \equiv \cos \theta$. Isotropic scattering can be described by the reduced scattering coefficient μ'_s , which is related to the anisotropic factor by $\mu'_s = \mu_s(1-g)$. In an average sense, this relationship equates the number of anisotropic scattering steps, given by $1/(1-g)$, with one isotropic scattering event [6]. A more explicit formula is given as follows:

$$\mu'_s = \int (1 - \mu) P(\theta) d\Omega. \quad (3.5)$$

For non-spherical particles, the phase function is related to the equal-projected-area sphere size parameter r [7]. In order to average the light scattering characteristics over particles sizes, a size distribution $f(r)$ must be applied. Since currently there is no clear consensus as to the size distribution best describing biological tissue, we compare three size distributions of power law, normal, and skewed logarithmic distributions with our experiments. The power law distribution can be written as [3-4]:

$$f_1(r) = c_0 r^{3-D_f}, \quad (3.6)$$

where D_f is the fractal dimension and c_0 is the normalization constant. The normal distribution can be given by [10]:

$$f_2(r) = 1/(\sqrt{2\pi}\sigma_m) \cdot \exp[-(r - r_m)^2 / (2\sigma_m^2)], \quad (3.7)$$

where r_m and σ_m are the mean and standard variation, respectively. The general form of skewed logarithmic distribution can be expressed as [11-13]:

$$f_3(r) = c_n r^n \exp[-(\ln r - \ln r_n)^2 / (2\sigma_n^2)], \quad (3.8)$$

where c_n is a normalizing factor, and the quantities r_n and σ_n set the center and width of the distribution, respectively. For $n = -1$ and $n = 0$, the distribution function is called the logarithmic normal distribution and

zeroth-order logarithmic distribution, respectively. Both distributions are used extensively in particle-size analysis.

Considering practical particle size and the T -matrix computation, the minimum and maximum particle size should be limited. Thus we modify the distribution functions to avoid the infinity while still remaining smooth:

$$f'_i(r) = \begin{cases} c_i, & \text{for } r \leq r_{\min} \\ f_i(r), & \text{for } r_{\min} \leq r \leq r_{\max} \end{cases}, i = 1, 2, 3, \quad (3.9)$$

where $f_i(r)$ represents the three size distributions, c_i is a constant used to normalize the distribution function. r_{\min} and r_{\max} refer to the maximum and minimum particle size parameters. Accordingly, the effective radius and effective variance of a size distribution are defined as:

$$r_{\text{eff}} = \frac{1}{S} \int_{r_{\min}}^{r_{\max}} \pi r^3 f'_i(r) dr, \quad (3.10)$$

and the effective variance given by

$$v_{\text{eff}} = \frac{1}{S \cdot r_{\text{eff}}^2} \int_{r_{\min}}^{r_{\max}} \pi r^2 (r - r_{\text{eff}})^2 f'_i(r) dr, \quad (3.11)$$

where S is the average cross-sectional area

$$S = \int_{r_{\min}}^{r_{\max}} \pi r^2 f'_i(r) dr. \quad (3.12)$$

The effective size parameter is $S_{\text{eff}} = k \cdot r_{\text{eff}}$, where $k = 2\pi n_0 / \lambda$ is the wave number in the surrounding medium, and n_0 is the background refractive index.

Slightly rough surface random nonspherical particles are applied to simulate scattering centers in biological tissue and cells. Since the candidates for scattering centers in biological tissue and cells are the cell itself, the nucleus, and other organelles, and their microstructures range from peroxisomes and lysosomes 0.2-0.5 μm or smaller, to mitochondria approximately 0.3-0.7 μm in diameter and 1-4 μm in length, to nuclei 3-10 μm in diameter [14-15]. We assume the size of the random particles is not too large compared with the incident wavelength and the particle orientation is uniform distributed. Figure 3.1 illustrates phase functions computed by randomly oriented slight rough surface cylinders [5] with three size distributions at wavelength of 1100 nm. Parameters are selected to retain the same values of r_{eff} and v_{eff} , which are 3.36 μm and 0.12, respectively.

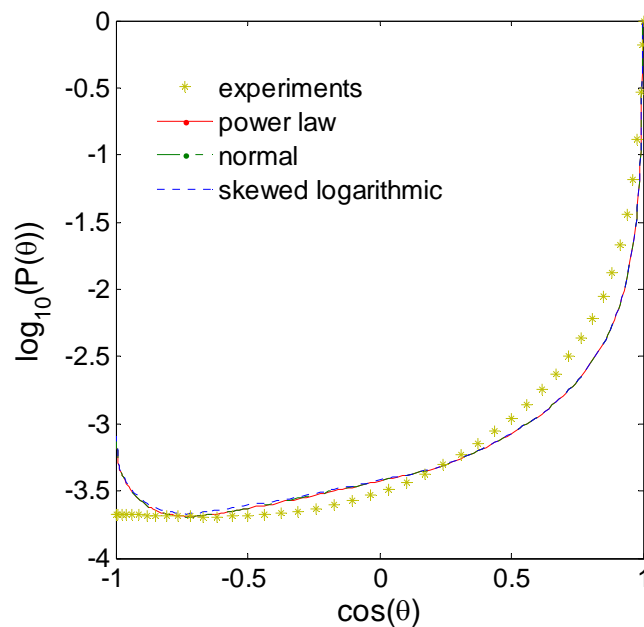


Figure 3.1 Phase functions with different size distribution functions with same $r_{eff} = 3.36\mu\text{m}$ and $v_{eff} = 0.12$, and same shape parameters ($K = 2$, $\tau = 0.7$, $CP = -0.5$), at incident wavelength 1100 nm.

It is interesting to notice that different size distributions have similar phase functions providing the values of r_{eff} and v_{eff} are the same. The result is quite practical and important, since only two key parameters can provide a unified classification of all distributions, and the same result can be obtained for many different analytical parameterizations of natural size distributions [16]. Currently the size distribution best describing biological tissue is not clear, because of the complicated structure of tissue, composed of tightly packed groups of cells entrapped in a network of fibers through which water percolates. The two key parameters r_{eff} and v_{eff} provide an effective approach to describe the scattering properties of the biological tissue.

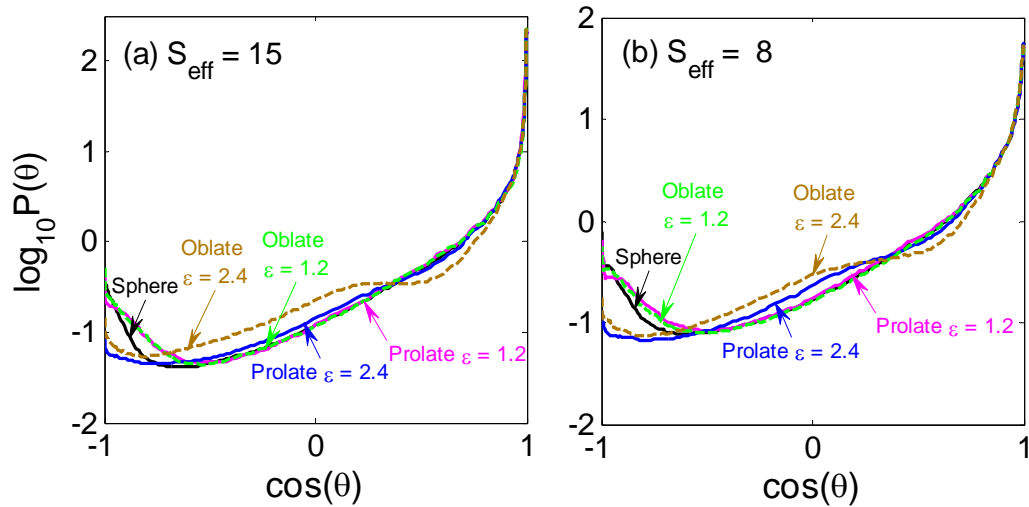


Figure 3.2 Phase functions for randomly oriented slight rough prolate (solid curves) and oblate (dash curves) spheroids with different aspect ratios of 1.2, 2.4, and equal-projected-area spheres with different effective size parameter S_{eff} . (a) $S_{eff} = 15$; (b) $S_{eff} = 8$;

Here slightly rough surface spheroids, including both oblate and prolate spheroids, are used to model light scattering properties of rat embryo fibroblast cells (M1) and mitochondria *in vitro*. Experimental data were

reported by Mourant *et al.* [17]. According to Schmitt [12], the refractive index variation for the scatterers in M1 cells and the media are 1.4 and 1.35, respectively. Here we take the complex refractive index as $1.38 + 0.008i$, and characterize the size of the random spheroids with the radius of the equal-projected-area sphere. Figure 3.2 compares the phase functions of prolate and oblate rough surface spheroids, with those of equal-projected-area spheres, at different effective size parameters after size and orientation averaging. It shows that phase functions of nonspherical particles are quite different from those of equal-projected-area sphere, especially in the side-scattering and backscattering region. Even for a single rough surface spheroid, it produces a unique, shape-specific phase function. Similar results can be found in the literature of Macke *et al.* [18] and Muinonen [19]. However, in Figure 3.2, the phase functions are similar for prolate and oblate spheroids with small aspect ratios. This is understandable, because for small aspect ratios, the shape difference between prolate and oblate spheroids is negligible.

Figures 3.3 and 3.4 compare the phase functions measured by experiments with those calculated by a spherical model and a nonspherical model which is mixture of prolate and oblate slightly rough surface spheroids. The theoretical computations are obtained by averaging over a wide aspect-ratio distribution of prolate and oblate spheroids. To simplify the calculation, we assume the aspect ratios are uniformly distributed, centered at the aspect ratio 2 for both

prolate and oblate spheroids. while the incident wavelength is taken as 760 nm. Note that in the exact forward scattering region, the phase function is insensitive to particle nonsphericity and the equal-projected-area spheres can be used to characterize the randomly oriented nonspherical particles. It means that Mie theory can be used to analyze transmittance measurements of biological tissue and cells in microscope without causing significant errors. However, the difference between spherical and non-spherical models becomes quite obvious in the side-scattering and backscattering regions, and therefore the results from Mie theory would cause serious errors in biological image detection when applied to analyze reflectance measurements in a microscope.

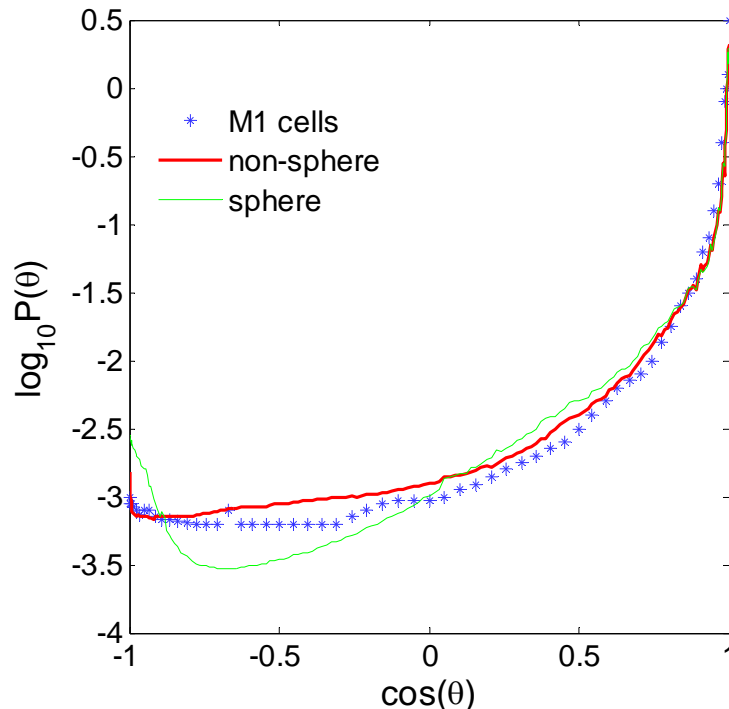


Figure 3.3 Phase functions for suspensions of rat embryo fibroblast cells (M1) with spherical and nonspherical model with the effective size parameter

$S_{eff} = 15.5$ and experimental results.

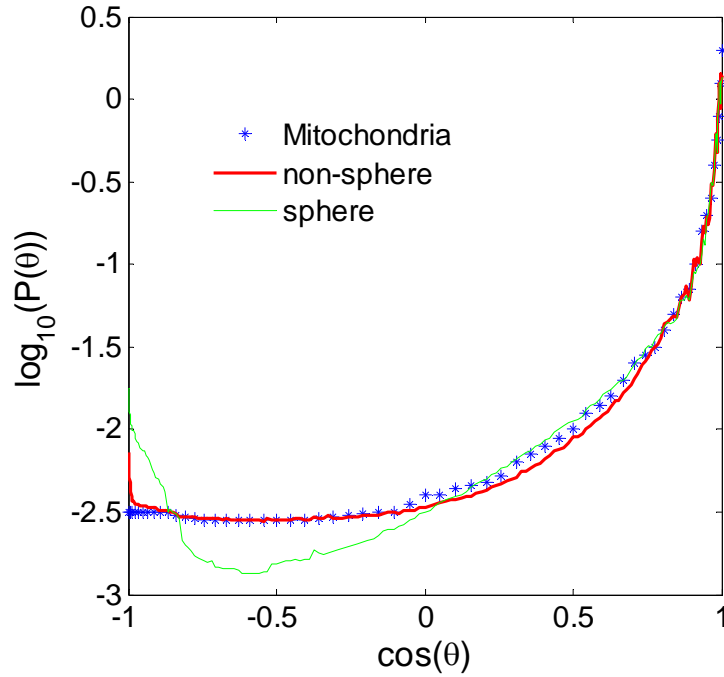


Figure 3.4 Phase functions for suspensions of mitochondria with random non-spherical model, spherical model with the effective size parameter $S_{eff} = 10.3$ and experimental results. The particles are chosen as a combination of Figure 1(c) and (d) in Ref.[5].

Table 3.1 demonstrates the anisotropy factors g and reduced scattering coefficients μ'_s from experiment data, and computations with nonspherical and spherical models, respectively. Compared with the experiment data, the difference of g between nonspherical and spherical models is small, which confirms our conclusion that forward scattering is least sensitive to particle nonsphericity. The same phenomenon can be found in μ'_s , which means that in the diffusion regime, the number of anisotropic steps of both nonspherical and spherical models are similar.

In sum, slightly rough surface spheroids are used to model scatter center in biological cells. Experimental results corroborate that scattering properties of non-spherical particles can be significantly different from those of equivalent

spheres in both biological tissue and biological cells. To understand better the light-scattering mechanism, it is necessary to substitute the spherical model with the random non-spherical model. Finally, we note that our experimental results are limited to M1 cells and mitochondria and the computational results pertain to a specific refractive index scale of biological tissue. To extrapolate our conclusions to other kinds of tissue, additional laboratory experiments and additional calculations are necessary.

	Experiments		Spheroids		Sphere	
	g	μ'_s	g	μ'_s	g	μ'_s
M1 cell	0.90	1.21	0.87	1.32	0.88	1.27
Mitochondria	0.78	3.65	0.79	3.49	0.80	3.52

Table 3.1 Anisotropy factors and reduced scattering coefficients for M1 cells and mitochondria.

3.3 Fractal model in biological tissue

Light propagation in biological tissue and cells is fundamental to biomedical imaging for both diagnosis and therapy. The conventional models are based on a distribution of discrete scatters [3, 12]. However, on a microscopic scale, the constituents of the tissue do not present clear boundaries and merge into a quasi-continuum structure. Therefore, discrete particles may be less appropriate than the tissue modeling as a continuous

random medium due to weak random fluctuations of the dielectric permittivity. Recently, a number of researches have been carried out to characterize the optical properties of biological tissue and cells using the autocorrelation function of the dielectric permittivity. Moscoso *et al.* suggested a fractal behavior of the tissue and determined the scattering function by an exponential correlation [1]. Xu and Alfano modified the correlation function with a power law volume fraction [4]. Sheppard simplified the Xu's correlation function by using K distribution and extend the applicable scale of the correlation function to a subfractal regime [2]. However, all of the above researches are based on the assumption of statistically space homogeneous and isotropic media, which is not realistic in many cases. Isotropic assumption implies that the aggregates have the same microgeometric properties, while many biological tissues are directionally sensitive.

Although the autocorrelation function has been widely applied to description of the refractive index variations, it suffers from a number of disadvantages. For example, many different refractive index variations can produce the same autocorrelation function. More seriously, the autocorrelation function will not cope well with a non-stationary mean, which is a common feature of living tissue and cells. Besides, many biological tissue and cells are anisotropic, *i.e.* they have a pronounced lay, and the autocovariance function, which should have a variance at the origin common to all profiles, can only be

obtained if all profiles are measured from the same mean plane. If they are not, singularities are created at the origin of the function [20].

In this section, we employ the mathematical model of the structure function to describe the interaction of light and fractal aggregates. The structure function was originally introduced in fluid mechanics to analyze the fine structure of turbulence[21-22]. The structure function is related simply to the autocorrelation function but is without some of its disadvantages.

The m -th order structure function of refractive index $n(r)$ can be expressed as:

$$s_m(\tau) = \lim_{L \rightarrow \infty} \frac{1}{L} \int_0^{L-\tau} [n(r) - n(r + \tau)]^m dx. \quad (3.13)$$

In the case of fractal aggregates, we employ the 2-nd order structure function to describe the refractive index fluctuations:

$$s_2(\tau) = \lim_{L \rightarrow \infty} \frac{1}{L} \int_0^{L-\tau} [n(r + \tau) - n(r)]^2 dx. \quad (3.14)$$

The power spectrum of the structure function is given by [23]

$$P(kL) = -\lim_{\alpha \rightarrow 0} \int_0^{\infty} s_2(\tau) \cos(2\pi k\tau) \exp(-\alpha\tau) d\tau. \quad (3.15)$$

where k is the frequency and L is the correlation length of the fractal structure.

One possible solution of the power spectrum of the fractal aggregates is described by Micali *et al.* [24]:

$$P(kL) = \frac{A \sin[n \arctan(kL)]}{(1 + k^2 L^2)^{n/2} n k L}. \quad (3.16)$$

where $D_f = 5.5 - n$ is the fractal dimension of the structure, and A is a constant coefficient.

Figure 3.5 shows the power spectrum normalized to unity for low frequencies. The power spectral density variation has a similar shape to those of Xu's model and Sheppard's model with a break point and a power-law decay.

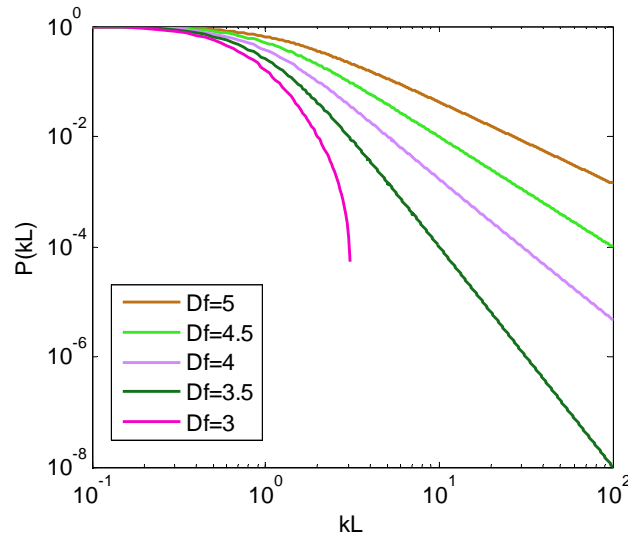


Figure 3.5 Power spectrums, normalized to unity for low frequencies

The amplitude scattering function $AS(\theta)$ now can be written as:

$$\begin{aligned}
 |AS(\mu)|^2 &\propto P^2[kL(1-\mu)^{1/2}] \\
 &= \frac{A^2 \sin^2[n \arctan(kL(1-\mu)^{1/2})]}{(1+k^2L^2(1-\mu))^n n^2 k^2 L^2 (1-\mu)}.
 \end{aligned} \tag{3.17}$$

where $\mu = \cos \theta$. The anisotropy factor (the mean cosine of the scattering angle) is given by:

$$g = \int \frac{(1 + \mu^2)\mu |AS(\theta)|^2}{2k^2} d\Omega / \int \frac{(1 + \mu^2) |AS(\theta)|^2}{2k^2} d\Omega. \quad (3.18)$$

The anisotropy factor for different fractal dimension is illustrated in Figure

3.6:

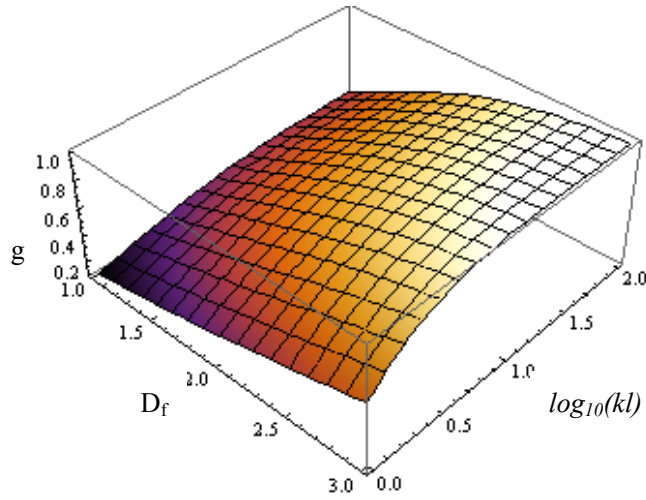


Figure 3.6 Anisotropy factor as a function of kL and fractal dimension D_f

The reduced scattering coefficient $\mu'_s = \mu_s(1 - g)$ is:

$$\mu'_s = \int d\Omega \frac{(1 + \mu^2)(1 - \mu) |AS(\theta)|^2}{2k^2}, \quad (3.19)$$

shown in Figure 3.7.

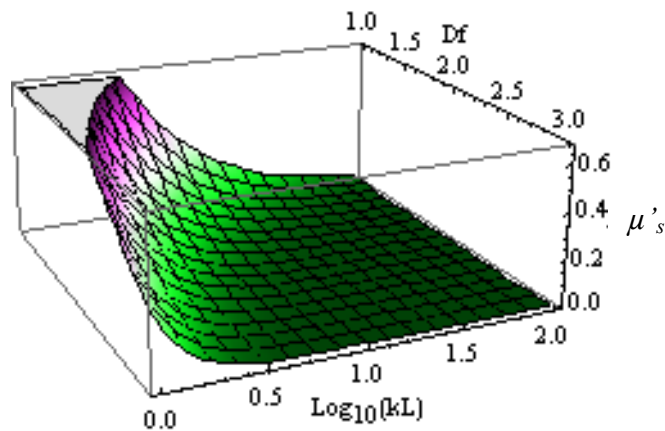
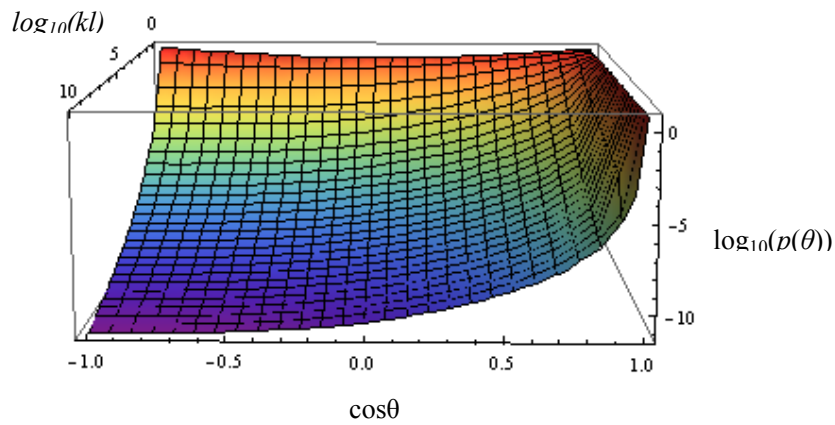


Figure 3.7 Reduced scattering coefficient for different fractal dimensions

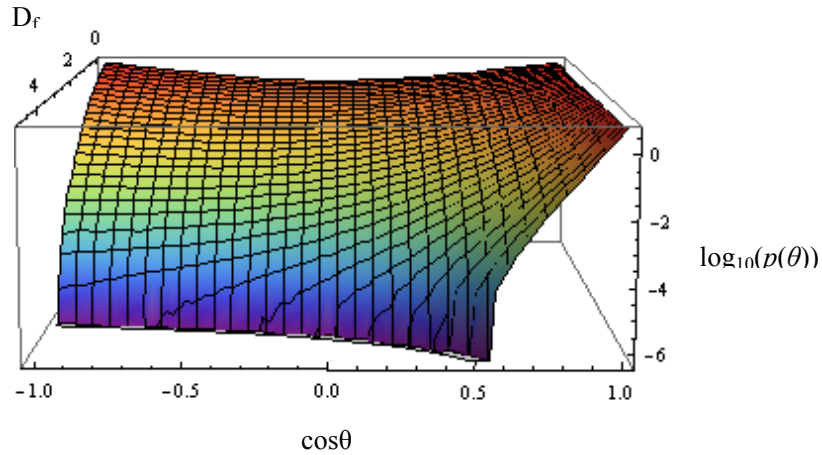
The phase function is given by:

$$\begin{aligned}
 P(\theta) &= \frac{(1 + \mu^2) |AS(\theta)|^2}{2k^2} \\
 &= \frac{(1 + \mu^2) A^2 \sin^2[n \arctan(kL(1 - \mu)^{1/2})]}{2k^2 (1 + k^2 L^2 (1 - \mu))^n n^2 k^2 L^2 (1 - \mu)}.
 \end{aligned}
 \tag{3.20}$$

The three dimensional phase functions according to the variations of kL and D_f are demonstrated in Figure 3.8, respectively:



(a)



(b)

Figure 3.8 Phase function as a function for: (a) given D_f ; (b) given kL

In sum, we propose a general structure function to describe the light scattering characteristics of the fractal aggregates. This structure function can

be applied to both isotropic and anisotropic scale of the biological tissue. For $kL \ll 1$, the power spectrum can be further reduced to:

$$P(kL) = \frac{A}{[1 + (kL)^2]^{n/2}}, \quad (3.21)$$

and the power spectrum is the same as the expression described in the previous paper [25].

3.4 Conclusion

In this chapter, we explored tissue optics modeling in biological tissue and cells. Two different models, which are nonspherical model and fractal model, are described. In the nonspherical model, the general functions of random non-spherical rough-surfaced particles with axially-symmetric properties were introduced. It was found that with a series of generation functions restricted by the “display window”, the medium can be characterized by a cluster of random non-spherical particles. An important feature of this generation function is that generally all kinds of shapes can be described completely with five parameters. This method can thus greatly reduce the complexity of the calculation and facilitate the process of tissue optics modeling in biological science. The *T*-matrix method was proposed to model the tissue optics properties in biological science. The good agreement between theoretical predictions with non-spherical model and experimental data confirms our hypothesis that the particles’ shapes are the key contributor to tissue optics

modeling. The simulation results have slight differences with the experimental results in the forward scattering region and back scattering region. This may be attributed to the existing of multiple scattering. The phase function for surface-equivalent spheres showed larger discrepancy with experiments, especially in the side-scattering and backscattering regions. This suggests that the scattering properties of non-spherical particles can be significantly different from those of equivalent spheres. Therefore, the random non-spherical model has the power to simulate biological tissue better than the spherical model. This random non-spherical model can thus contribute to the accurate and efficient optical property description for biological science and medical diagnosis.

The fractal mechanism is also studied to model the optical properties in biological tissue. The structure function is developed to describe the interaction of light and fractal aggregates. It is found that the second order structure function is related to the fractal dimension directly. The structure function is different from the correlation function that was discussed by Xu *et al.* [26] and Sheppard [25]. The relationship is of importance since it should help to predict the fractal properties from the second order structure function, which is also related to the correlation function $R(r)$. The fractal model with structure function has a wider scale of applications, since it can be applicable to a medium containing fractal-type aggregates; however, the correlation function cannot be used for the finite form of fractal surfaces.

References

1. M. Moscoso, J. B. Keller, and G. Papanicolaou, "Depolarization and blurring of optical images by biological tissue," *J Opt Soc Am A* **18**, 948-960 (2001).
2. C. J. R. Sheppard, "Fractal model of light scattering in biological tissue and cells," *Optics Letters* **32**, 142-144 (2007).
3. R. K. Wang, "Modelling optical properties of soft tissue by fractal distribution of scatters," *J. Mod. Opt.* **47**, 103-120 (2000).
4. M. Xu, and R. R. Alfano, "Fractal mechanisms of light scattering in biological tissue and cells," *Optics Letters* **30**, 3051-3053 (2005).
5. W. Gong, K. Si, and C. J. R. Sheppard, "Modeling phase functions in biological tissue," *Opt. Lett.* **33**, 1599-1601 (2008).
6. V.D.Tuan, *Biomedical Photonics Handbook* (CRC, 2003).
7. M. I. Mishchenko, L. D. Travis, and A. A. Lacis, *Scattering, Absorption and Emission of light by small particles* (Cambridge, 2002).
8. H. C. Van de Hulst, *Multiple Light Scattering* (Academic, 1980).
9. M. I. Mishchenko, L. D. Travis, R. A. Kahn, and R. A. West, "Modeling phase functions for dustlike tropospheric aerosols using a shape mixture of randomly oriented polydisperse spheroids," *J Geophys Res-Atmos* **102**, 16831-16847 (1997).
10. G. I. Ruban, S. M. Kosmacheva, N. V. Goncharova, D. Van Bockstaele, and V. A. Loiko, "Investigation of morphometric parameters for granulocytes and lymphocytes as applied to a solution of direct and inverse light-scattering problems," *J Biomed Opt* **12**, - (2007).
11. M. Kerker, *The Scattering of Light and other electromagnetic Radiation* (Academic, 1969).
12. J. M. Schmitt, and G. Kumar, "Optical scattering properties of soft tissue: a discrete particle model," *Appl Optics* **37**, 2788-2797 (1998).
13. Y. S. Fawzy, M. Petek, M. Terceelj, and H. S. Zeng, "In vivo assessment and evaluation of lung tissue morphologic and physiological changes from non-contact endoscopic reflectance spectroscopy for improving lung cancer detection," *J Biomed Opt* **11**, - (2006).
14. A. Alberts, D. Bray, J. Lewis, M. Raff, K. Roberts, and J. D. Watson, *Molecular Biology of the Cell* (Garland, New York, 1994).
15. G. E. Palade, "An electron microscope study of the mitochondrial structure," in *Mitochondria*, E. Sato, ed. (University Park Press, Baltimore, 1972).
16. J. Lenoble, and C. Brogniez, "A comparative review of radiation aerosol model," *Beitr, Phys. Atmos.* **57** (1984).
17. J. R. Mourant, J. P. Freyer, A. H. Hielscher, A. A. Eick, D. Shen, and T. M. Johnson, "Mechanisms of light scattering from biological cells relevant to noninvasive optical-tissue diagnostics," *Appl Optics* **37**, 3586-3593 (1998).

18. A. Macke, "Scattering of Light by Polyhedral Ice Crystals," *Appl Optics* **32**, 2780-2788 (1993).
19. K. L. K. Muinonen, J. Peltoniemi, and W. M. Irvine, "Light scattering by randomly oriented crystals," *Appl. Opt.* **28**, 3051-3060 (1989).
20. R. S. Sayles, and T. R. Thomas, "Spatial Representation of Surface-Roughness by Means of Structure-Function - Practical Alternative to Correlation," *Wear* **42**, 263-276 (1977).
21. B. K. Shivamoggi, and P. Mulser, "Dielectric screening in the Thomas-Fermi model," *Phys Rev A* **54**, 4830-4836 (1996).
22. P. L. Van'yan, "Structure function of the velocity field in trubelent flows," *Jetp Lett+* **82**, 580-586 (1996).
23. I. A. Popov, L. A. Glushchenko, and J. Uozumi, "The study of fractal structure of ground glass surface by means of angle resolved scattering of light," *Opt Commun* **203**, 191-196 (2002).
24. N. Micali, V. Villari, L. M. Scolaro, A. Romeo, and M. A. Castriciano, "Light scattering enhancement in an aqueous solution of spermine-induced fractal J-aggregate composite," *Phys Rev E* **72**, - (2005).
25. C. J. R. Sheppard, "A fractal model of light scattering in biological tissue and cells," *Opt. Lett.* **32**, 142-144 (2007).
26. M. Xu, and R. R. Alfano, "Fractal mechanisms of light scattering in biological tissue and cells," *Opt. Lett.* **30**, 3051-3053 (2005).

Chapter 4 Confocal microscopy using angular gating techniques

4.1 Introduction

There has been renewed interest recently in the divided aperture technique, as in the so-called specular microscope, for imaging through scattering media such as biological tissue [1, 2]. This technique is based on the principle of angular gating, one of several gating mechanisms that can be used to eliminate multiply-scattered light. Other gating mechanisms include confocal, coherence, nonlinear and polarization gates.

Angular gating had its beginning with the ultramicroscope, in which the sample is illuminated perpendicular to the imaging optical axis [3]. The specular microscope, or divided aperture technique, combines different beam paths for illumination and detection with confocal imaging, so that light scattered other than in the focal region is rejected [4-8]. The ultramicroscope can be regarded as the fore-runner of confocal theta microscopy [9, 10], and selected plane illumination microscopy (SPIM) (also called orthogonal-plane fluorescence optical sectioning, OPFOS) [11, 12], both of which can also be implemented in a fluorescence mode. KEM Equipment Company (Elk Grove Village, IL) and Irvine Optical Corporation (Burbank, CA) both manufactured deep field photographic microscope systems in the 1980s. All of these

techniques have in common the fact that the illumination and detection pupils do not overlap, so that the illumination and detection beams cross only in the focal region.

In divided aperture microscopy, light scattered by a single scattering event in the focal region can be detected, but light scattered by a single scattering event outside of the focal region will not be able to pass through both the collection pupil and the confocal pinhole (or slit). Multiply-scattered light can get through the collection pupil, but is unlikely to pass through the confocal pinhole. Most published work on the divided aperture technique have used two D-shaped apertures (segments of circles) one each for illumination and detection, respectively [7]. The width of the region between the two Ds can be adjusted in size to reject cross-talk from multiple scattering. For this geometry, light reflected specularly from a surface with normal parallel to the optical axis can be detected, hence the name specular microscope. It has been shown that the system can be used in surface profiling applications to select the specular reflection from a spherical surface, while rejecting a reflection that comes from the centre of the sphere [13]. Other alternative geometries are possible. It is interesting to note that Dwyer *et al.*[2] based their analysis on two offset non-overlapping circles, but they used this only as an approximation to the D-shaped case. Another alternative geometry is to use a circular pupil and a non-overlapping annulus.[14, 15] This arrangement is fundamentally different from the previously mentioned examples, as in this

case specular reflections from a normal surface are not detected. It was shown using geometrical optics that such a combination of a circular and an annular pupil with a finite-sized detector pinhole gives an axial response from a planar object that drops identically to zero at a particular defocus distance. So in some cases with a finite sized pinhole the axial resolution can be increased by use of an annular pupil, which is contrary to our normal expectation that the depth of focus is increased for an annular pupil [16].

Although theory on imaging in a system with D-shaped apertures based on geometrical optics has been presented by Maurice and Koester [6-8], a diffraction theory had not yet been given. In this chapter we first consider the imaging of a point object in a confocal system (point source and point detector) with D-shaped apertures. 3D coherent transfer function (CTF) and 3D optical transfer function (OTF) are considered. Later we extend our research to off-axis apertures, elliptical apertures and Schwartz apertures. The axial response from a planar, integrated intensity, as well as the signal level is presented.

4.2 Confocal scanning microscope with D-shaped apertures

The geometry of the confocal microscope with two D-shaped pupils is given by Figure 4.1. Section 4.2.1 investigates the 3D imaging performance in confocal bright-field microscopy with D-shaped apertures and a point detector.

In this case, the imaging is purely coherent. Section 4.2.2 introduces the 3D incoherent imaging performance for confocal one-photon fluorescence microscopy with D-shaped apertures.

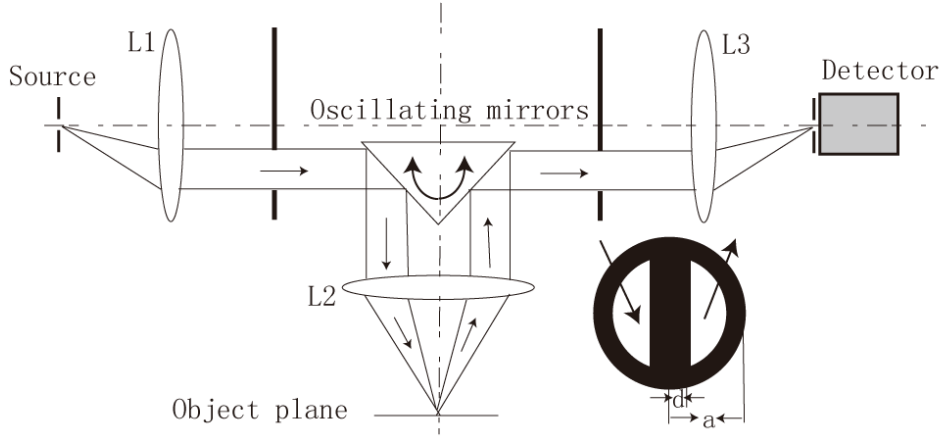


Figure 4.1 Geometry of the confocal microscope with two centro-symmetric D-shaped pupils.

4.2.1 Coherent transfer function

For weakly scattering objects, 3-D transfer functions can be used to completely describe image formation of confocal system. Consider a single D-shaped pupil with outer radii a and distance parameter d ($-1 \leq d \leq 1$) (Figure 4.1). The width of the separator between the two D shapes is then $2d$. The defocused pupil function under the paraxial approximation can be expressed as:

$$P(\rho, \theta, u) = \begin{cases} \exp[-i(u/2)\rho^2], & d \leq \rho \leq 1 \text{ \& } -\cos^{-1}(\rho/d) \leq \theta \leq \cos^{-1}(\rho/d) \\ 0, & \text{otherwise} \end{cases}, \quad (4.1)$$

in cylindrical coordinates, where $\rho = r/a$ denotes the normalized radial coordinate, r is the real radial coordinate, and u is the axial optical coordinate defined as

$$u = (8\pi n / \lambda) z \sin^2(\alpha / 2). \quad (4.2)$$

Here λ and $n \sin \alpha$ are the incident wavelength and the numerical aperture (NA) of the objective, respectively, and z is the defocus distance from the focal plane.

According to Fourier transform theory, the 3D CTF can be expressed as:

$$c(l, \psi, s) = \int [P(\rho, \theta, u) \otimes_2 P(\rho, \theta + \pi, u)] \exp(-ius) du, \quad (4.3)$$

where \otimes_2 represents the 2-D convolution operation with respect to l . After mathematical manipulations, the 3D CTF $c(l, \psi, s)$ normalized by the value of $c(l=0, \psi=0, s=0)$ at $d=-1$ (corresponding to the circular pupils), can be derived as:

$$c(l, \psi, s) = \begin{cases} c_A(l, \psi, s), & \text{when } \tan^{-1}[\sqrt{1-d^2} / (1-d)] \leq \psi \leq \pi / 2, \\ c_A(l, \psi, s) + c_B(l, \psi, s), & \text{when } 0 < \psi < \tan^{-1}[\sqrt{1-d^2} / (1-d)], \\ c_B(l, \psi, s), & \text{when } \psi = 0. \end{cases} \quad (4.4)$$

where

$$\begin{cases} c_A(l, \psi, s) = \frac{1}{2\pi} \int_{\theta_0}^{\theta_1} \int_{(d+m/2)/\cos\theta}^{\rho_0} \delta(s - \rho^2 - l^2 / 4) \rho d \rho d \theta, \\ c_B(l, \psi, s) = \frac{1}{2\pi} \int_{\theta_0}^{\theta_2} \int_{(d+m/2)/\cos\theta}^{\rho_0} \delta(s - \rho^2 - l^2 / 4) \rho d \rho d \theta, \end{cases} \quad (4.5)$$

with

$$\begin{cases} \vartheta_0 = -\tan^{-1}\{[\sqrt{1-(d+m)^2} - n/2]/(d+m/2)\}, \\ \vartheta_1 = \tan^{-1}\{[\sqrt{1-d^2} - n/2]/(d+m/2)\}, \\ \vartheta_2 = \tan^{-1}\{[\sqrt{1-(d+m)^2} + n/2]/(d+m/2)\}, \\ \rho_0 = -l|\cos(\psi+\theta)|/2 + \sqrt{1-l^2\sin^2(\psi+\theta)}/4. \end{cases} \quad (4.6)$$

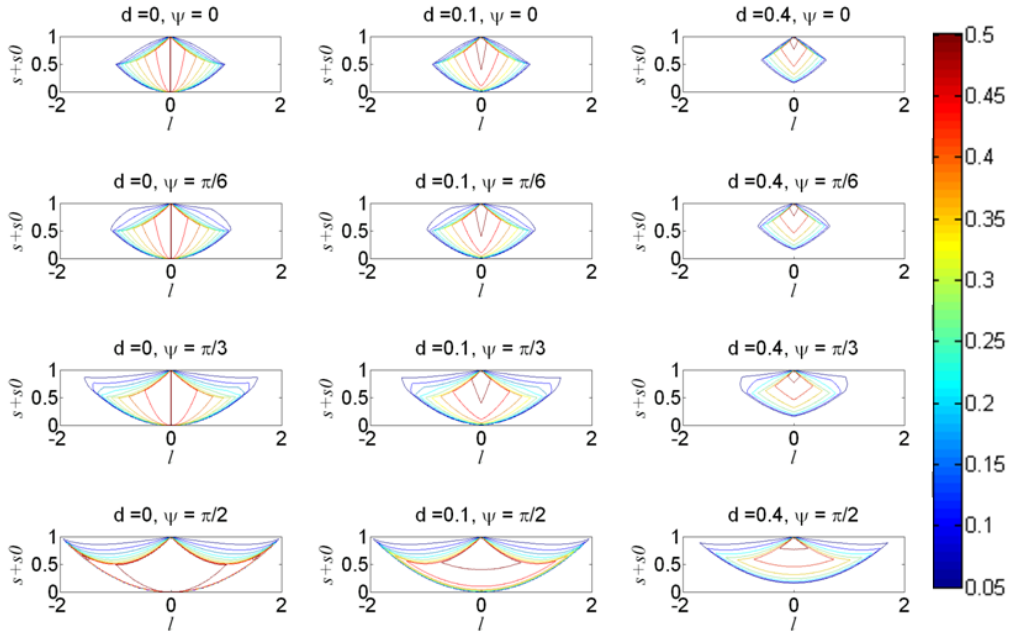


Figure 4.2 The 3-D coherent transfer functions with different distance parameters d and different angles ψ . For $d = 0$ and $\psi = \pi/2$, the 3-D CTF is the same as the conventional confocal microscope with two circular pupils.

Figure 4.2 gives the complete view of the 3-D CTF $c(l, \psi, s)$ in the reflection-mode confocal scanning microscope with two D-shaped pupils for different distance parameter d and different angular parameter ψ . At the special case of $d = 0$ and $\psi = \pi/2$, the 3-D CTF is the same as the conventional confocal microscope with two circular pupils. It is interesting to note that the transverse cut-off frequency $l_{cutoff}(d, \psi)$ depends on both d and

ψ ; while the axial cut-off frequency $s_{cutoff}(d)$ only depends on d . For a given ψ , as d is increased, both the axial cut-off frequency and the transverse cut-off frequency reduce. However, for a given d , as ψ increases, only the transverse cut-off frequency increases and reaches the maximum of $l_{cutoff}(\pi/2, \psi) = 2\sqrt{1-d^2}$ at $\psi = \pi/2$; while the axial cut-off frequency remains at $s_{cutoff}(d) = d^2$. Therefore, in the region $0 \leq s + s_0 \leq d^2$, the value of the CTF is zero, which indicates that the image information in this region is missing, thus the low axial frequency region cannot be imaged.

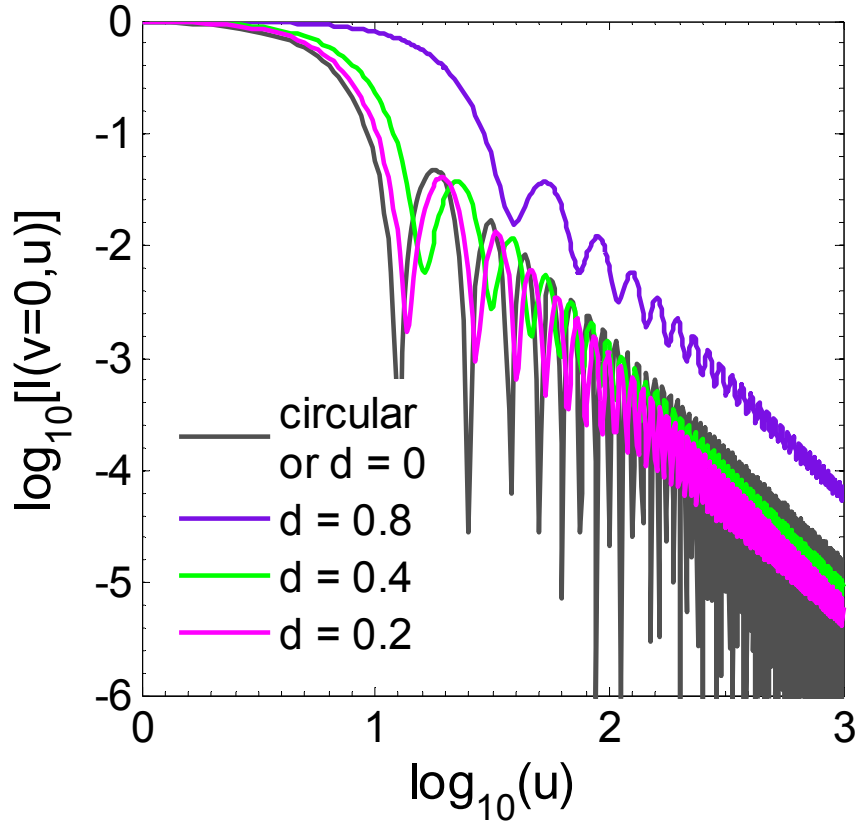


Figure 4.3 The intensity along the axis for a D-shaped pupil shown as a log-log plot.

In confocal microscopy, the concept of the integrated intensity was introduced to quantify the background produced by a scattering medium [17,

18]. If the intensity image of a point object is $I(v_x, v_y, u)$, then the contribution to the background in the focal plane from a distribution of particles a distance z away is

$$I_{\text{int}}(u) = \int I(v_x, v_y, u) dv_x dv_y. \quad (4.7)$$

Figure 4.3 shows the integrated intensity $I_{\text{int}}(u)$ for a confocal microscope with two D-shaped pupils and a point detector as a log-log plot. For a confocal microscope with two circular pupils, $I_{\text{int}}(u)$ falls off as $1/u^2$, and for one circular and one narrow annular pupil it falls off roughly as $1/u$. [17] For the divided aperture system, $I_{\text{int}}(u)$ falls off more quickly, for $d=0$ as $1/u^{2.54}$, becoming close to $1/u^{3.2}$ for larger values of d . This demonstrates the advantage of the divided aperture technique for imaging through scattering media.

4.2.2 Optical transfer function

The divided aperture technique can be also used with a confocal fluorescence modality. In this study, we propose the use of the divided aperture technique in confocal fluorescence, and extend our study to the performance of a system with divided D-shaped apertures (DCM), based on incoherent image formation theory. This system has potential applications in any area of fluorescence microscopy into scattering media such as tissue.

The corresponding effective intensity point spread function (IPSF) for confocal single-photon fluorescence microscopy with divided apertures is

$$h(v_x, v_y, u) = |h_{ill}(v_x, v_y, u)|^2 \left(|h_{dec}(v_x, v_y, u)|^2 \otimes_2 D(v_x, v_y) \right), \quad (4.8)$$

where \otimes_2 denotes the two-dimensional convolution operation. $D(v_x, v_y)$ is the intensity sensitivity of the finite-size detector. $h_{ill}(v_x, v_y, u)$ and $h_{dec}(v_x, v_y, u)$ are the 3D amplitude point spread functions (APSF) of the illumination and detection objective lenses, respectively. They are defined by

$$h_{ill,dec}(v_x, v_y, u) = \frac{1}{\pi} \iint_p P_{ill,dec}(\rho_x, \rho_y) \exp \left\{ i \left[v_x \rho_x + v_y \rho_y - \frac{1}{2} u (\rho_x^2 + \rho_y^2) \right] \right\} d\rho_x d\rho_y, \quad (4.9)$$

where $P_{ill,dec}$ are the pupil functions for illumination and detection wave path, respectively. v_x , v_y , and u are optical coordinates. They are related to the true distance from the focal point by $v_x = 2\pi x n \sin \alpha / \lambda$, $v_y = 2\pi y n \sin \alpha / \lambda$, and $u = 8\pi z n \sin^2(\alpha/2) / \lambda$, with λ the excitation or emission wavelength, α the semi-angular aperture of the lens, and n the refractive index of the immersion medium. The coordinates ρ_x , and ρ_y are distances in the pupil plane, normalized by the pupil radius a . Note that in this paper, we neglect the Stokes' shift, and thus assume that the system has equal fluorescence and incident wavelengths. In practice, the longer fluorescence wavelength may result in a small degradation of the imaging performance. The Stokes' shift for practical dyes is often around 6%.

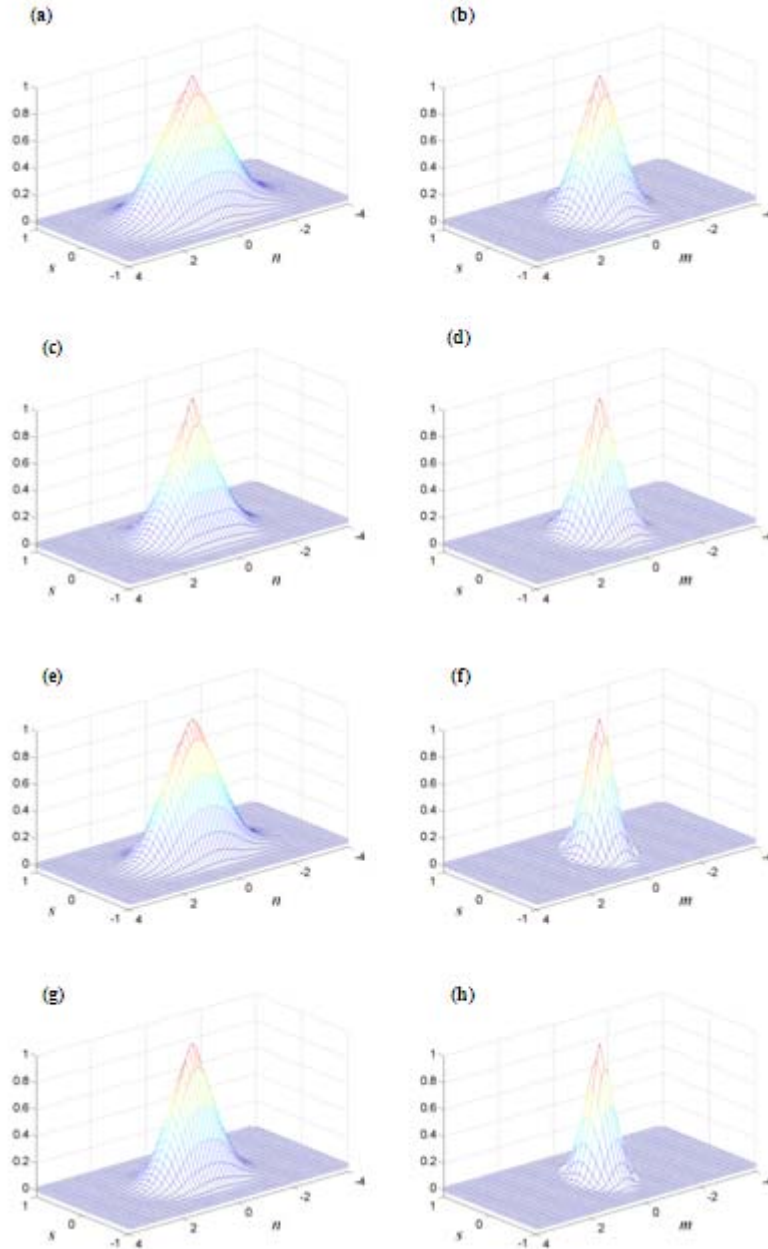


Figure 4.4 3D OTFs for confocal one-photon fluorescence microscopy with D -shaped apertures with various d and v_d . (a) $C(m=0,n,s)$ with $v_d=0,d=0$ and circular apertures with $v_d=0$; (b) $C(m,n=0,s)$ with $v_d=0,d=0$ (c) $C(m=0,n,s)$ with $v_d=4,d=0$ and circular apertures with $v_d=4$; (d) $C(m,n=0,s)$ with $v_d=4,d=0$; (e) $C(m=0,n,s)$ with $v_d=0,d=0.4$; (f) $C(m,n=0,s)$ with $v_d=0,d=0.4$; (g) $C(m=0,n,s)$ with $v_d=4,d=0.4$; (h) $C(m,n=0,s)$ with $v_d=4,d=0.4$.

The corresponding 3D optical transfer functions (OTF), $C(m,n,s)$, is given by the 3D Fourier transform of the 3D IPSF. Here m , n , and s are spatial frequencies in the x , y , z directions, normalized by $n \sin \alpha / \lambda$, $n \sin \alpha / \lambda$, and

$4n\sin^2(\alpha/2)/\lambda$, respectively. In the following we use l to describe the transverse spatial frequency, defined by $l = \sqrt{m^2 + n^2}$. Since the D-shaped aperture is not circularly symmetrical, we consider two special cases: $C(m=0, n, s)$ and $C(m, n=0, s)$.

In practice, the detector is not a single point but has a finite size to increase the signal strength. Figure 4.4 illustrates the 3D OTF of DCM with different values of d and v_d , compared with that of CM. Note that for CM a well-known missing cone of spatial frequencies appears around the origin [19]. However, as the width of the divider strip increases, this cone gradually disappears.

Figure 4.5 illustrates the integrated intensity of a point object for CM and DCM with various values of detector size. It is shown that for a point object with a point detector, $I_{\text{int}}(u)$ falls quickest for DCM with $d=0$ in the region of small values of u . As d increases, $I_{\text{int}}(u)$ becomes gradually broader, and eventually broader than the case for CM. For large values of u , $I_{\text{int}}(u)$ in CM falls off according to an inverse-square law. However, $I_{\text{int}}(u)$ for DCM falls off more quickly, for $d=0$ as $1/u^{2.53}$, becoming close to $1/u^{3.2}$ for larger values of d [20]. For a finite-size detector, in the region of small values of u , as d increases the rate of decay of $I_{\text{int}}(u)$ for DCM first increases then decreases, leading to an optimum value of d to achieve the maximum rate of decay. However, for larger values of u , the rate of decay of $I_{\text{int}}(u)$ for DCM increases as d increases. For instance, when $v_d = 4$, $I_{\text{int}}(u)$

for DCM falls off for $d = 0$ as $1/u^{2.33}$, becoming close to $1/u^{2.5}$ for $d = 0.2$, compared with $1/u^{1.9}$ for CM. The fast decay of the integrated intensity demonstrates the advantage of the divided aperture technique in imaging through scattering media.

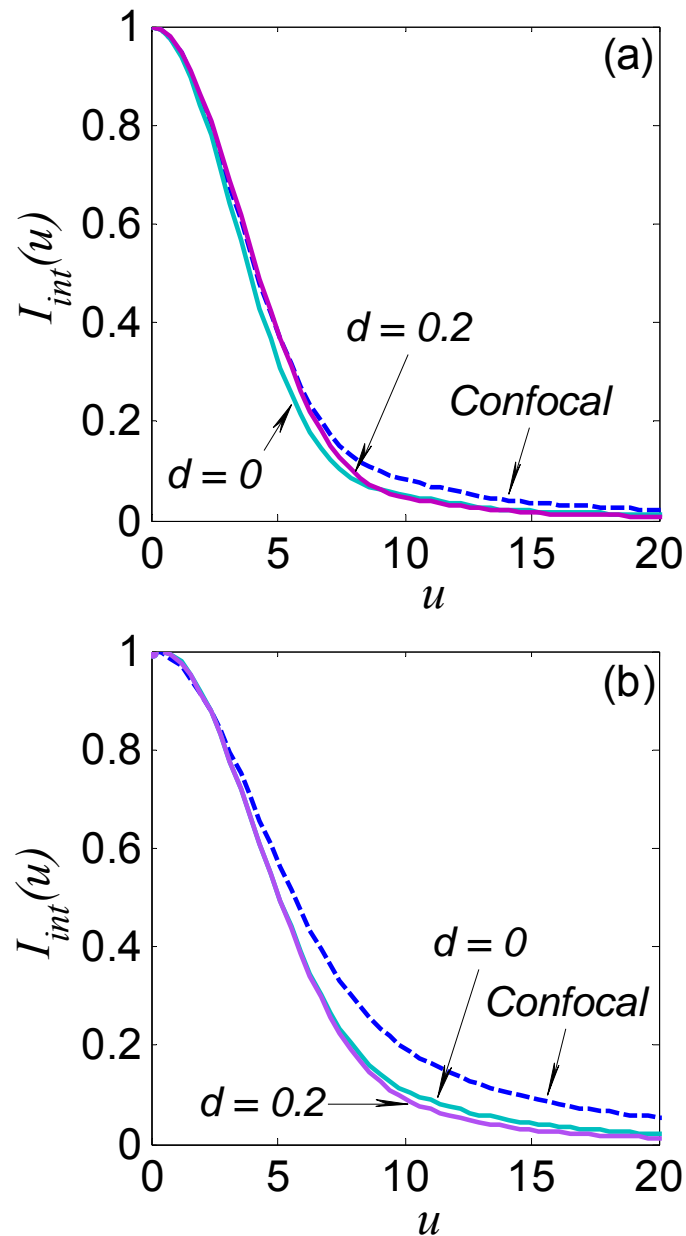


Figure 4.5 Integrated intensities of CM (solid lines) and DCM (dash lines) for (a) $\nu_d=0$, and (b) $\nu_d=4$, respectively.

4.3 Confocal scanning microscope with off-axis apertures

We have seen how I_{int} for D-shaped apertures decays as only $1/u^{2.53}$ for $d = 0$. We attribute this to the strong diffraction peak on the optical axis caused by the circular edge of the aperture, a phenomenon similar to the Poisson spot. We therefore consider other shapes of aperture, which avoid this effect. In this section, the 3D coherent transfer function (3D) for two off-axis circular apertures in a reflection-mode confocal scanning microscope is analytically derived under the paraxial approximation. The properties of axial response and integrated intensity are compared with two D-shaped apertures.

The system diagram is similar as Figure 4.1. However, we use two off-axis circular apertures instead of two D-shaped apertures, shown in Figure 4.6.

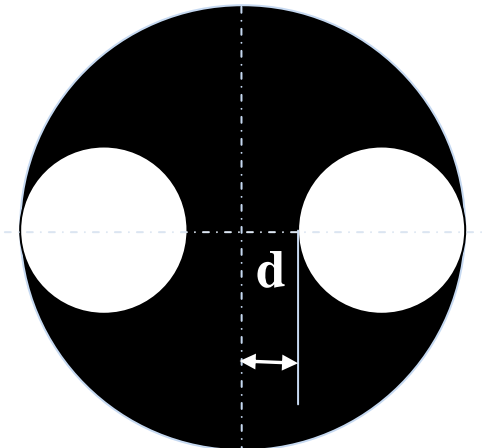


Figure 4.6 Two off-axis circular apertures: one for illumination, and the other for detection

The corresponding 3D CTF calculated by Eq. 4.3 is shown in Figure 4.7.

Compared with the CTF of D-shaped apertures (shown in Figure 4.2), given the same value of d , although the axial cut-off frequency remains, the absolute value in the high frequency region reduces, implying that the axial resolution will be degraded. Moreover, it is also shown that the transverse cut-off

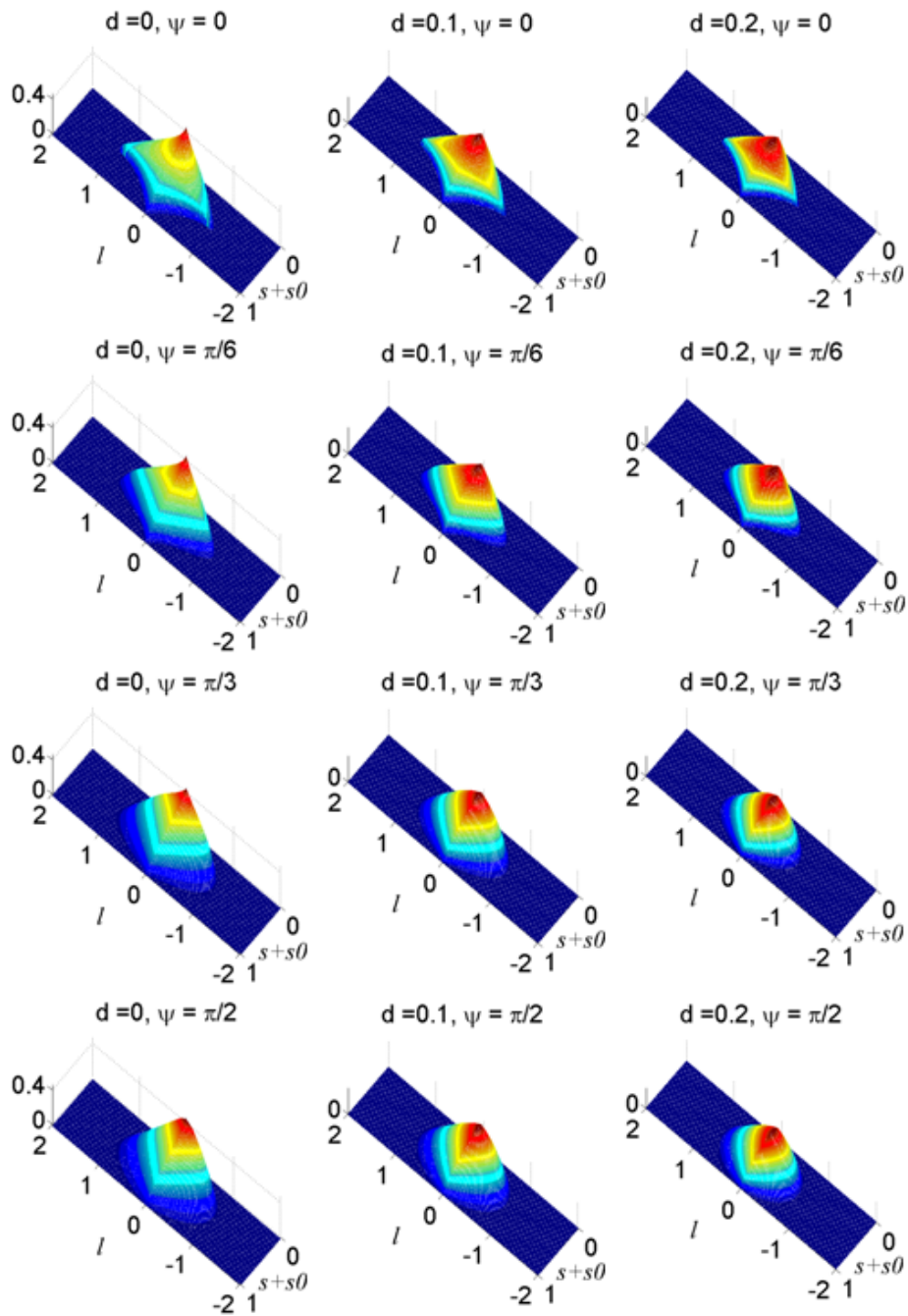


Figure 4.7 The 3-D amplitude coherent transfer functions in the reflection-mode confocal scanning microscope with two off-axis circular apertures

frequency is reduced for two off-axis circular apertures, which means that the transverse resolution will be also degraded. This phenomenon is mainly caused by the effective pupil area. Given the same value of d , the effective pupil area of off-axis apertures is smaller than D-shaped apertures, and thus the spatial resolution degraded.

The intensity along the axis can be calculated by transforming to polar coordinates ρ, θ where $\rho^2 = t = \rho_x^2 + \rho_y^2$ and performing the integration in θ first, to give the integrated pupil function

$$P_\theta(t) = \int_0^{2\pi} P(\rho, \theta) d\theta, \quad (4.10)$$

where $P(\rho, \theta)$ is the pupil function. Then the amplitude along the axis is

$$U(u) = \frac{2}{\pi} \int P_\theta(t) e^{-iut/2} dt. \quad (4.11)$$

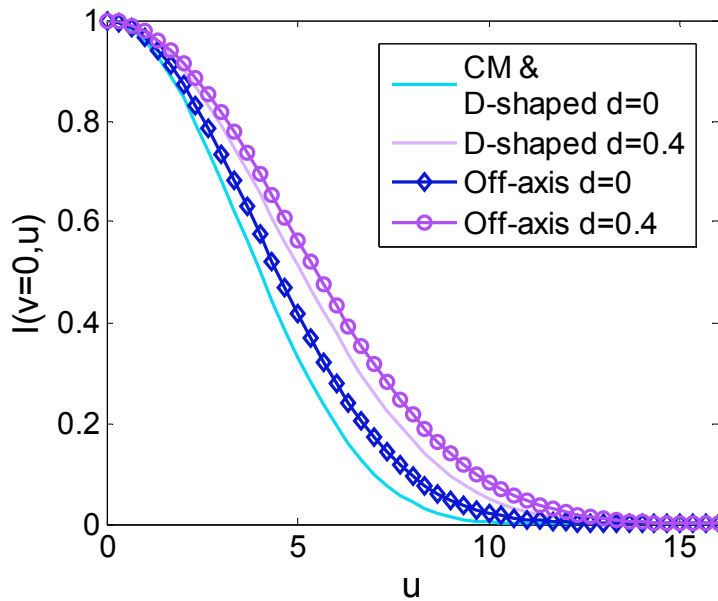


Figure 4.8 Axial responses of reflection-mode confocal scanning microscope with a point detector with traditional two circular apertures (CM), with two D-shaped apertures, and with two off-axis apertures, respectively.

Figure 4.8 illustrates the axial responses for reflection-mode confocal scanning microscope with a point detector for various kinds of apertures. It shows that given the same value of d , the axial response for D-shaped apertures is better than off-axis apertures. However, both of them are worse than traditional confocal microscopy (CM).

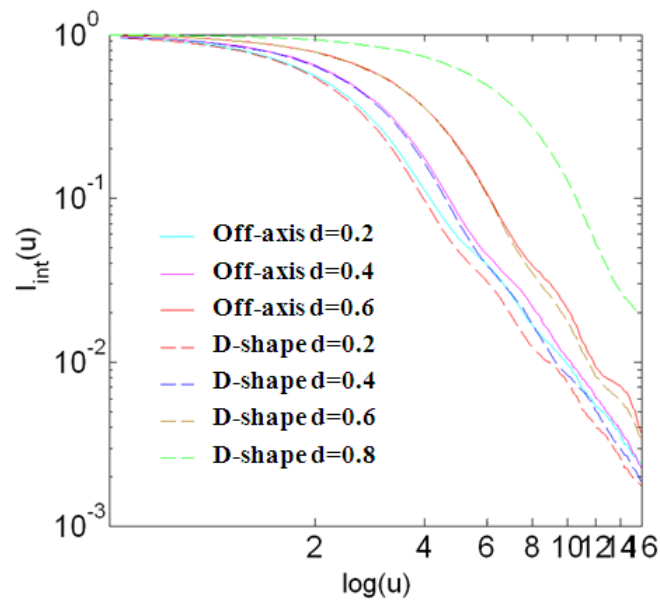


Figure 4.9 Integrated intensity of a reflection-mode confocal scanning microscope with a point detector using D-shaped and off-axis apertures.

Figure 4.9 compares the integrated intensities for D-shaped apertures and off-axis apertures. For same value of d , the integrated intensity of D-shaped aperture decays more quickly than off-axis apertures. However, as d increases, the difference of the decay rate becomes smaller and smaller. This because given the same value of d , the aperture area of D-shaped aperture is larger than off-axis aperture. As d increases, the difference of aperture area between the two kinds of apertures reduces. It suggests that the area of the aperture plays an important role in background rejection capability.

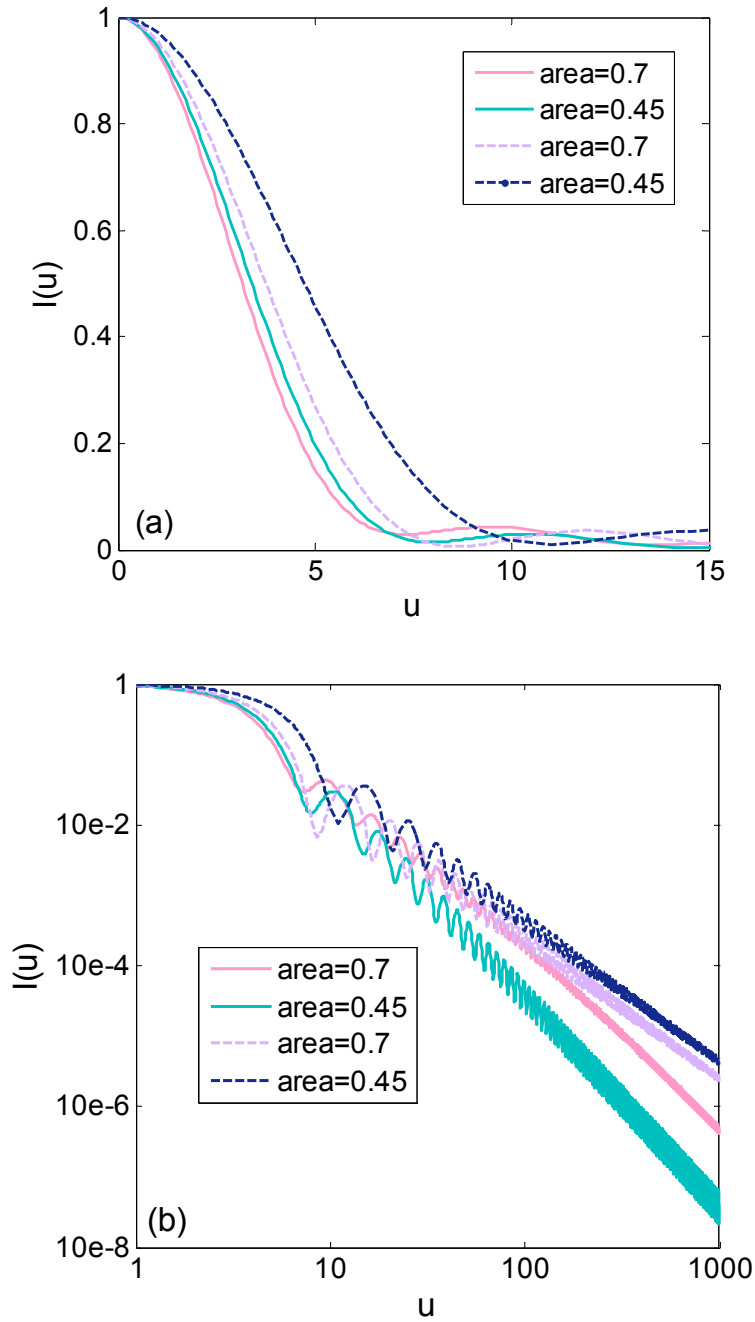


Figure 4.10 Axial response of a reflection-mode confocal scanning microscope with a point detector using D-shaped (dash lines) and off-axis apertures (solid lines) with equal area: (a) near focal plane; (b) far from the focal plane.

Consider the D-shaped and off-axis apertures have same area. The axial response for a point detector is displayed in Figure 4.10. It shown that compared with D-shaped apertures, the main lobe of axial response is

improved for off-axis apertures. As the area of the apertures is reduced, the improvement becomes more obvious. When defocus distance (u) increases, axial response decays more quickly for off-axis apertures than for D-shaped apertures. Moreover, for off-axis apertures, as the area decreases, decay rate of the axial response increases in the region for larger u , which implies that when the distance between two off-axis aperture increases, the background generated by the defocus plane far from the focal plane decreases.

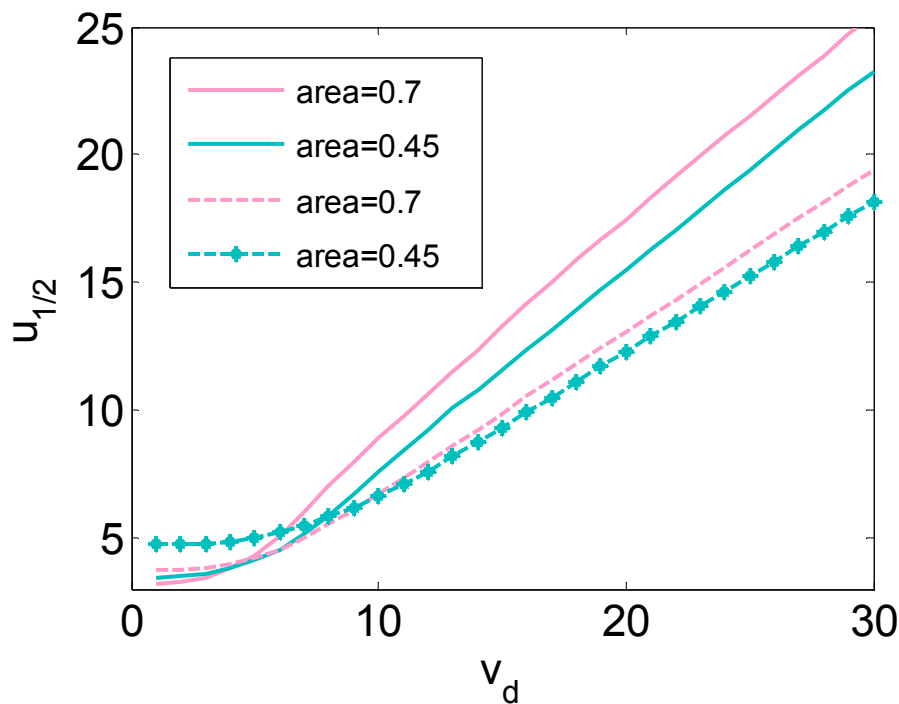


Figure 4.11 Half-width-half-maximum of the axial response as a function of normalized detector size for D-shaped apertures (dash lines) and off-axis apertures (solid lines).

The half-width-half-maximum (HWHM) of the axial response as a function of detector size is shown in Figure 4.11. It is interesting to note that given same aperture area, for a small value of detector size, the axial response of off-axis apertures is superior to D-shaped apertures. However, as the

detector size increases to a certain value, for example, when $\text{area} = 0.7$, $\nu_d = 4.5$, D-shaped apertures becomes superior to off-axis apertures.

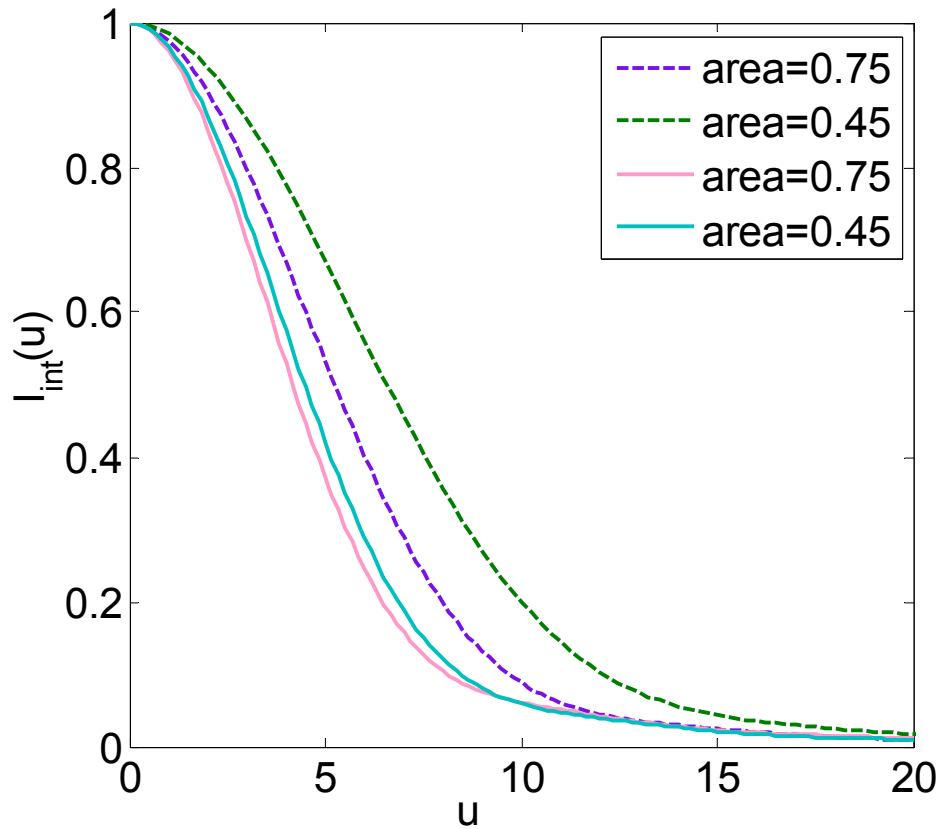


Figure 4.12 Integrated intensity of a reflection-mode confocal scanning microscope with a point detector for D-shaped (dash lines) and off-axis apertures (solid lines).

Figure 4.12 shows the integrated intensity for D-shaped and off-axis apertures with equal area. Compared with D-shaped apertures, given same pupil area, the integrated intensity of off-axis aperture is smaller in the near focal plane region, and decays faster when the defocus distance is larger (see Figure 10b), which suggests that given same aperture area, off-axis apertures can reject more background than D-shaped apertures.

In practice, a finite-sized pinhole is always used to enhance the detected signal strength. However, the amount of unwanted scattered light is also increased. Therefore, in order to fully understand the overall performance, it is necessary to introduce the signal level defined as the measured energy divided by that which enters the entrance pupil [21]. The detected intensity on the focal plane can be expressed as:

$$I_{u=0} = \iint D(v_x, v_y) \left| \iint P(\rho, \theta, 0) \exp[-i(v_x \rho \cos \theta + v_y \rho \sin \theta)] \rho d\rho d\theta \right|^2 dv_x dv_y. \quad (4.12)$$

The signal level for a given system can be given by:

$$\eta = \frac{I_{u=0}}{\varepsilon}, \quad (4.13)$$

where ε is the energy entering the illumination aperture. Figure 4.13 presents the signal level, normalized to unity for a large area detector, as a function of pinhole size for D-shaped and off-axis apertures, respectively. It is notes that for same shape of apertures, either D-shaped or off-axis apertures, the signal level increases as the aperture area increases. For apertures with different shapes, given same aperture area, signal level for off-axis aperture is higher than D-shaped apertures, especially when $4 \leq v_d \leq 10$.

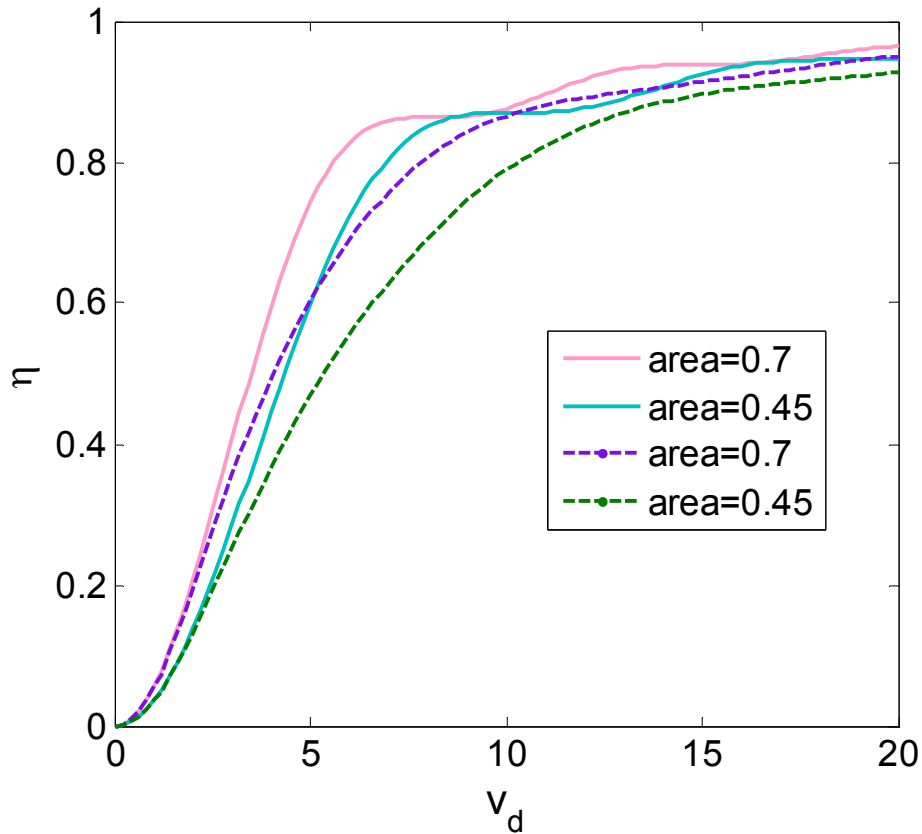


Figure 4.13 Signal level as a function of detected pinhole size for D-shaped (dash lines) and off-axis apertures (solid lines).

4.4 Confocal scanning microscope with elliptical apertures

In the section, we analyze a confocal microscope with a pair of half-elliptical apertures: one for illumination and the other for detection, shown in Figure 4.14. The axial response and integrated intensity is investigated. The signal level is also demonstrated.

According to Eq. 4.10 and 4.11, the axial response can be simply expressed by the Fourier transform of the integrated pupil function $P_\theta(t)$.

Therefore, the broader $P_\theta(t)$ is, the narrower the main lobe of the axial response becomes, consequently, the bigger the side lobes appears.

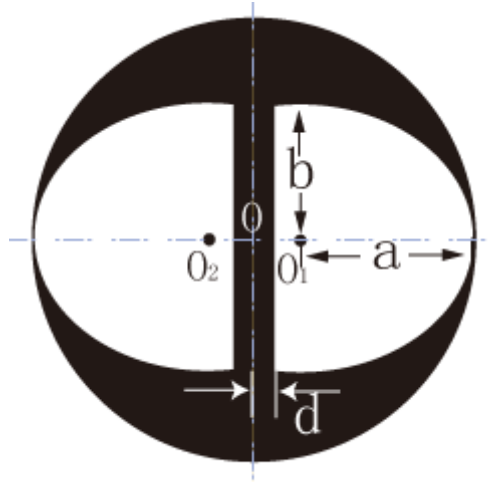


Figure 4.14 Two elliptical apertures: one for illumination and the other for detection

Figure 4.15 displays the integrated pupil function $P_\theta(t)$ for different values of a , b and d . The axial response for larger value of u is depicted in Figure 4.15. For given values of a and b , which means the shape of the ellipse is fixed, as d increases, $P_\theta(t)$ becomes narrower shown in Figure 4.15(a), which causes the optical sectioning properties to be degraded. However, the axial response decays more quickly. For given values of a and d , as the b increases, although the cut-off frequency of $P_\theta(t)$ is maintained (from d^2 to 1), the value in the high frequency region increases (Figure 4.15b), thus improving the optical sectioning properties. However, when b is equal to a , the fast decay rate of the axial response in the region for larger u is reached. This phenomenon suggests that: i). in order to obtain the best optical sectioning property and fast decay for larger defocus distances, the D-shaped

apertures are always the best choice when d is given; ii) although increasing d will broaden the main lobe of the axial response, it increases the decay rate of the axial response for larger defocus distances. These properties are confirmed in Figure 4.16, which is a log-log plot of the axial response.

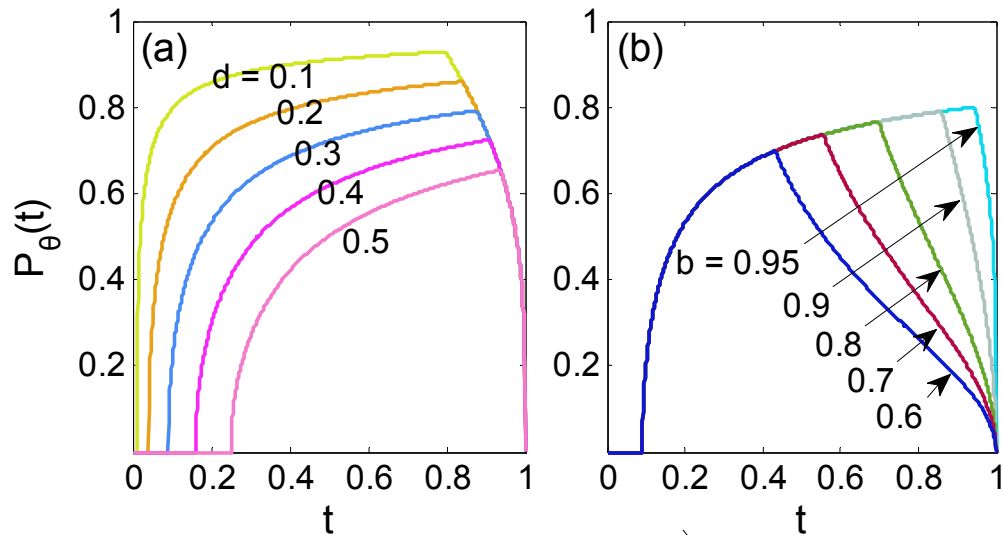


Figure 4.15 Integrated pupil function $P_\theta(t)$ for (a) given $a = 0.8$ and $b = 0.89$; (b) $a = 0.9$ and $d = 0.3$.

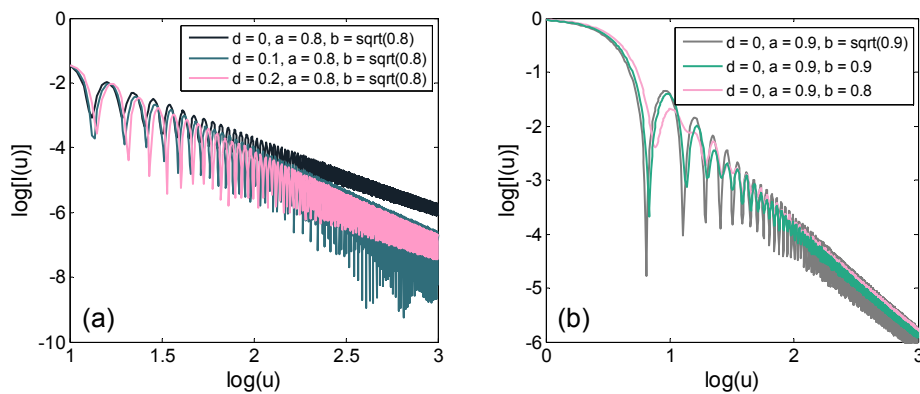


Figure 4.16 Axial response for elliptical apertures when u is large.

Figure 4.17 gives the comparison of integrated intensities for elliptical apertures with given d . Note that for same value of d , the integrated intensity of D-shaped apertures decays fastest, implying D-shaped performs best in the

view of background rejection. As the aperture area decreases, the background rejection capability is degraded.

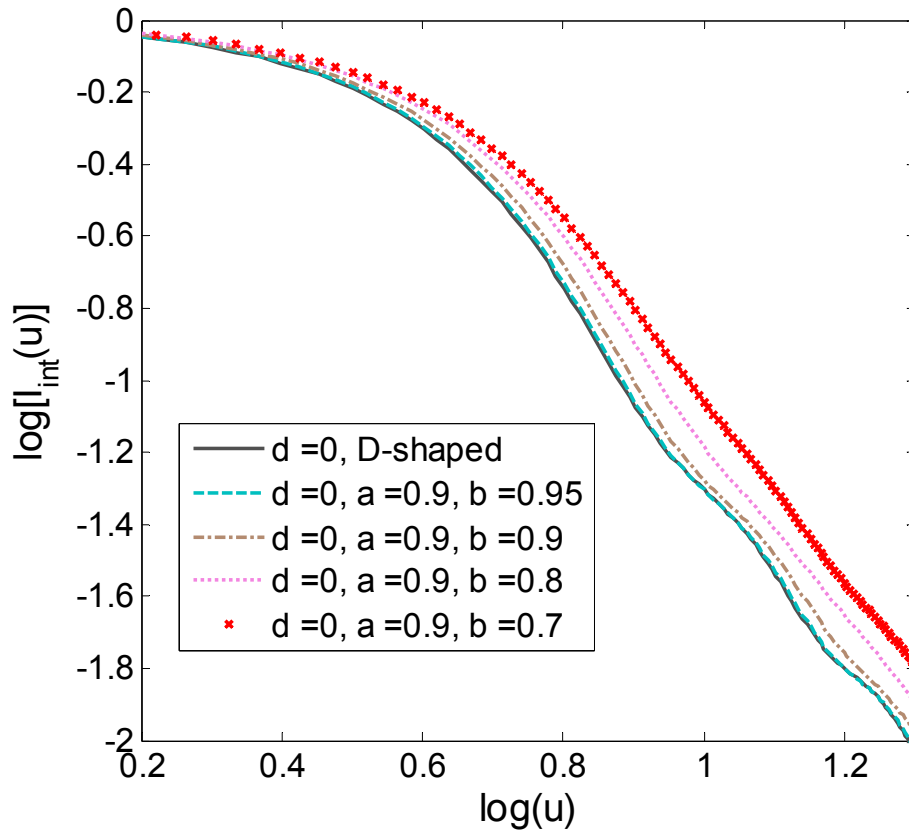


Figure 4.17 Integrated intensity for elliptical apertures with given value of d

Figure 4.18 compares the signal level for various value of b . It shows that given d , D-shaped apertures can obtain the high signal level. This is mainly due to the fact that given the values of d , a D-shaped aperture has the biggest aperture area.

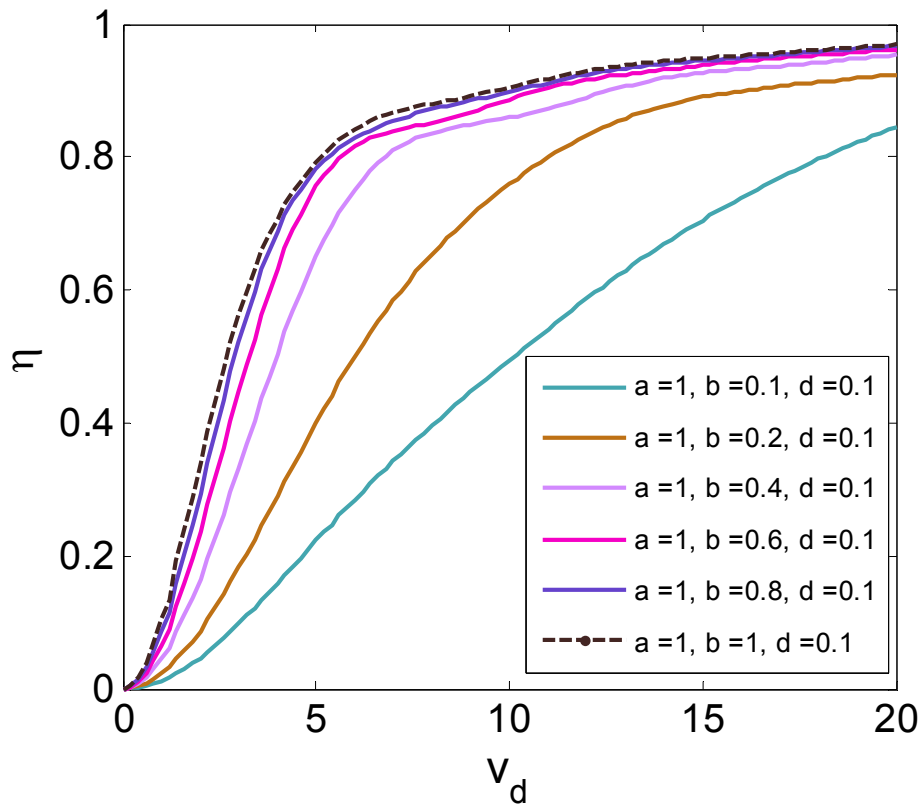


Figure 4.18 Signal level as a function of normalized detector pinhole size for elliptical apertures.

From above analysis, we understand that size of the aperture area plays a significantly important role in determining the optical sectioning properties, background rejection capability and signal level. The bigger the aperture area is, the better these performances are. Thus D-shaped aperture is always the best choice for high optical sectioning and background rejection. We further extend our research to the case when D-shaped and elliptical apertures with equal areas. Figure 4.19 compares the axial response for elliptical and D-shaped apertures with equal area. The HWHM of the axial response for D-shaped apertures is slightly narrower than elliptical apertures (Figure 4.19a). However, if we select the parameters in a certain way, for example, $a =$

b and $2a + d < 1$, the elliptical apertures then turn to off-axial circular apertures, which has the narrowest HWHM (see section 4.4). The HWHM of the axial response is defined by the broadness of the integrated pupil function, as well as the value in the high frequency region. Note that in the large u region, the axial responses of elliptical apertures decay faster than D-shaped apertures. As the distance between a pair of elliptical apertures ($2d$) increases, the decay spread increases.

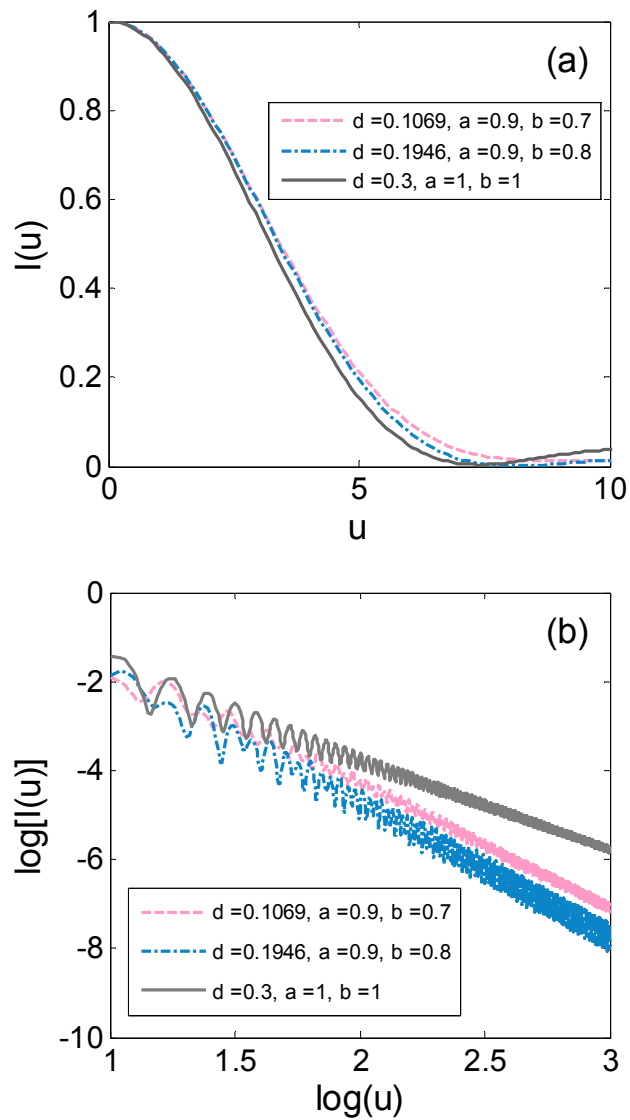


Figure 4.19 Axial response for elliptical and D-shaped aperture ($a=b=1$) with equal area.

Figure 4.20 provides the integrated intensity for elliptical and D-shaped apertures with equal area, showing D-shaped apertures is superior to elliptical apertures, but inferior to off-axis circular apertures (see section 4.4) in rejecting background from deep defocus plane.

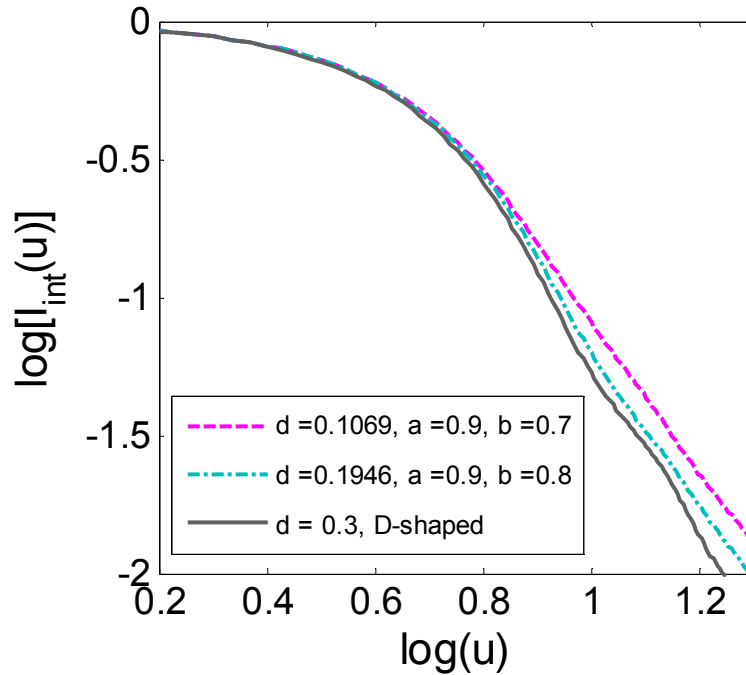


Figure 4.20 Integrated intensity for elliptical and D-shaped ($a = b = 1$) apertures with equal area.

Figure 4.21 illustrates the signal level as a function of detector pinhole size for elliptical and D-shaped apertures with equal area. It suggests that given equal aperture area, as the distance between the pair of apertures ($2d$) increases, the signal level decreases.

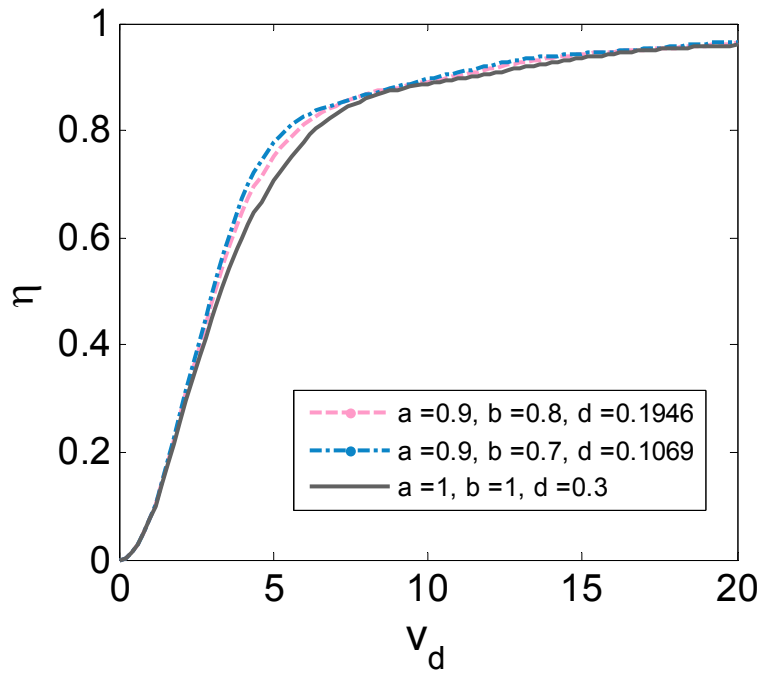


Figure 4.21 Signal level for elliptical and D-shaped ($a = b = 1$) apertures with equal area.

4.5 Confocal scanning microscope with Schwartz apertures

In above analysis, we propose a simple method to estimate the optical sectioning properties of a confocal system by using the integrated pupil function $P_\theta(t)$ (Eq 4.10 and 4.11), whose Fourier transform is the amplitude along the optical axis of the system.

In order to suppress the background, we always want the signal generated by defocus to decay as fast as possible. According to Fourier transform theory, if the k th derivative of a function becomes impulsive, its Fourier transform behaves as $|s|^{-k}$ at infinity, where s is in frequency domain [22]. Thus from the

derivative of the integrated pupil function, we can estimate the background decay rate of the confocal system. For example, for a traditional confocal microscope, the integrated pupil function is a rectangular function, whose first derivative is a pulse function. The amplitude along the axis decays as $1/u$, thus the intensity along the axis (axial response) behaves as the well-known $1/u^2$ for large u [23].

In this section, we propose a kind of special function introduced by Schwartz and Temp, which has all derivatives and furthermore is zero outside of a finite range, to generate an integrated pupil function. To our knowledge, this is the first time that the Schwartz function is introduced into the pupil function, named Schwartz aperture, in confocal microscopy. With Schwartz apertures, the signal generated by a defocused plane decays extremely fast as the defocus distance increases. An example of Schwartz function is given by

$$f_{schwartz}(x, \tau) = \begin{cases} e^{-\tau^2/(\tau^2-x^2)} & |x| < \tau, \\ 0 & |x| \geq \tau. \end{cases} \quad (4.14)$$

In order to make the aperture area as large as possible, we modify the Schwartz function by integrating it, which also has all derivatives zero and is zero outside a finite range (0-1):

$$P_{\theta}(t) = \int_{-\infty}^t f_{schwartz}(x - \tau_L, \tau_L) dx + \int_{-\infty}^t f_{schwartz}(1 - x - \tau_R, \tau_R) dx. \quad (4.15)$$

An example for integrated pupil functions of Schwartz aperture is shown in Figure 4.22.

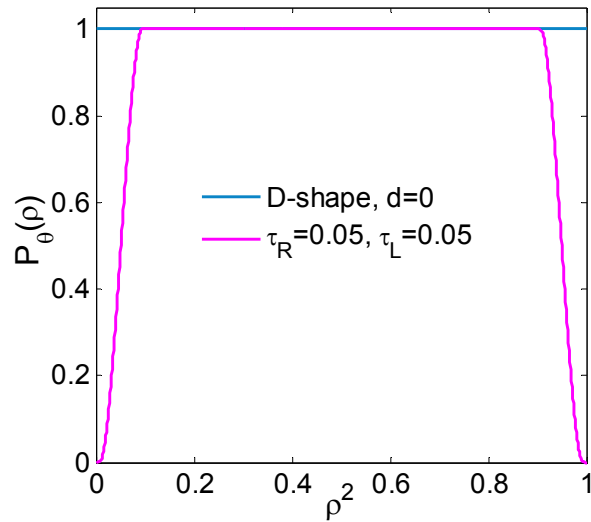


Figure 4.22. Integrated pupil function of Schwartz aperture.

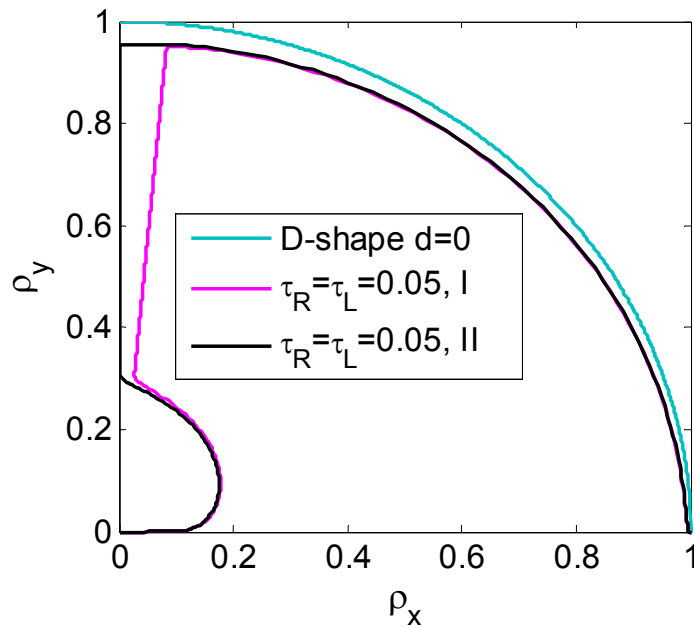


Figure 4.23 A set of Schwartz apertures with the same integrated pupil function.

For the same integrated pupil function, the reconstructed Schwartz aperture may have different kinds of shapes. One possible solution is using annular apertures whose transmittance amplitude is controlled by the Schwartz aperture function. Another possibility is shown on Figure 4.23. Note that one

integrated pupil function can reconstruct a set of Schwartz apertures with different pupil area.

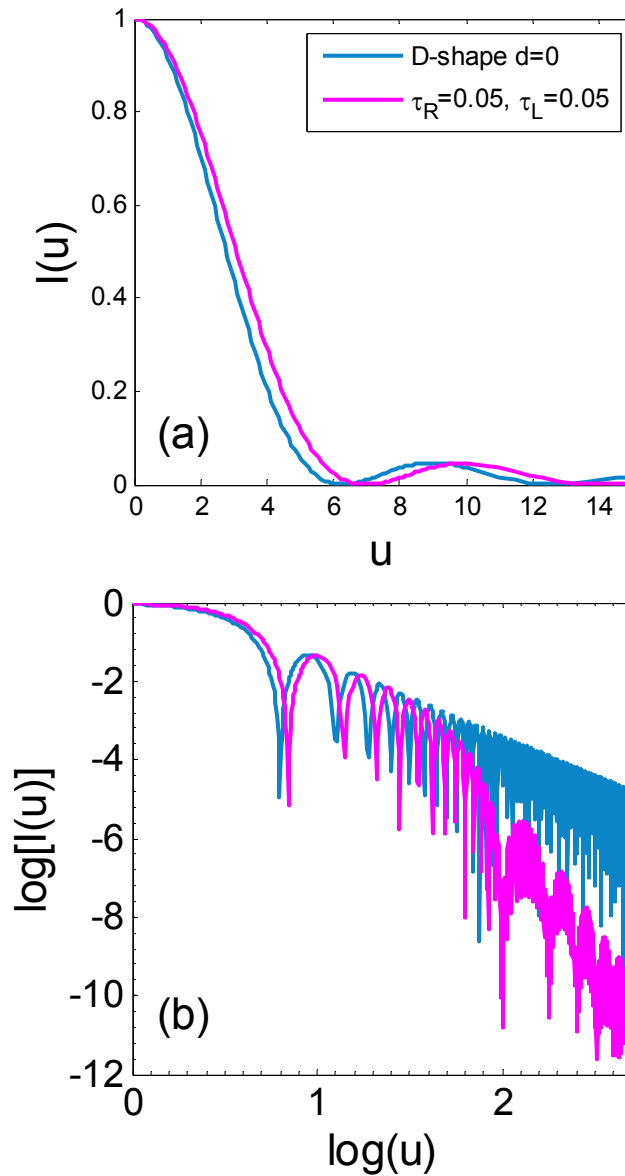


Figure 4.24 Axial response for Schwartz apertures

Figure 4.24 compares the axial response for D-shaped apertures and Schwartz apertures. We found that although the HWHM of the axial response for Schwartz apertures is degraded, in the deep defocus plane the axial response decays dramatically faster than D-shaped apertures. We believe that

the properties of Schwartz function will have wide application, for example, in focal modulation microscopy whose imaging penetration depth mainly depends on the ballistic light at the surface.

4.6 Conclusion

The application of angular gating techniques in confocal scanning microscope with divided apertures is discussed. Compared with traditional confocal scanning microscope, the main advantage of a confocal scanning microscope with divided apertures is that it can reject more background. Besides, using a finite-sized detector pinhole, it is also possible to improve the axial resolution [24].

The three-dimensional coherent transfer function and three-dimensional optical transfer function are investigated when a pair of D-shaped apertures is used. The optical sectioning property (shown by the axial response), background rejection capability (shown by integrated intensity) and signal level are studied when different kinds of divided apertures are used, including off-axis apertures, elliptical apertures and Schwartz apertures. If the pupils are separated by a strip of width $2d$, from the performance comparison among D-shaped, off-axis and elliptical apertures, we find that: i) given the same value of d , D-shaped apertures can obtain the best optical section properties and background rejection capability, as well as the highest signal level. This is

because D-shaped apertures have the largest aperture area. However, above three properties can be further improved by using serrated D-shape aperture, because the Poisson spot is suppressed by the serrated edge [25]; ii) given the same kind of divided apertures, as d increases, the background decay speed increases in deep defocus plane; iii) given equal area, off-axis apertures can obtain the best optical section properties and background rejection capability, as well as the highest signal level.

A simple method is proposed to estimate the optical sectioning and background rejection properties of a confocal system by using the integrated pupil function $P_\theta(t)$, given by the integration of the pupil function $P(\rho, \theta)$ with respect to the angle θ . The Fourier transform of $P_\theta(t)$ determines the optical sectioning property, while the derivative of $P_\theta(t)$ determines the background decay rate. According to this approach, Schwartz apertures, to our knowledge, are proposed for the first time, to dramatically reject the background. We believe Schwartz apertures will have wide application in deep penetration imaging, for example, focal modulation microscopy [26-28].

Reference

1. P. J. Dwyer, and C. A. DiMarzio, "Confocal reflectance theta line scanning microscope for imaging human skin in vivo," *Optics Letters* **31**, 942-944 (2006).
2. P. J. Dwyer, C. A. DiMarzio, and M. Rajadhyaksha, "Confocal theta line-scanning microscope for imaging human tissues," *Applied Optics* **46**, 1843-1851 (2007).
3. H. Siedentopf, and R. Zsigmondy, "Über Sichtbarmachung und Grössenbestimmung ultramikroskopischer Teilchen, mit besonderer Anwendung auf Goldrubingläser," *Annalen der Physik* **10**, 1-39 (1903).
4. H. Goldman, "Spaltlampenphotographie und -photometrie," *Ophthalmologica* **98**, 257-270 (1940).
5. D. M. Maurice, "Cellular membrane activity in the corneal endothelium of the intact eye," *Experientia* **15**, 1094-1095 (1968).
6. D. M. Maurice, "A scanning slit optical microscope," *Investigative Ophthalmology* **13**, 1033-1037 (1974).
7. C. J. Koester, "A scanning mirror microscope with optical sectioning characteristics: Applications in ophthalmology," *Applied Optics* **19**, 1749-1757 (1980).
8. C. J. Koester, "Comparison of optical sectioning methods: The scanning slit confocal microscope," in *Handbook of Confocal Microscopy*, J. Pawley, ed. (Plenum Press, New York, 1990).
9. E. H. K. Stelzer, S. Lindek, S. Albrecht, R. Pick, G. Ritter, N. J. Salmon, and R. Stricker, "A new tool for the observation of embryos and other large specimens - confocal theta-fluorescence microscopy," *Journal of Microscopy* **179**, 1-10 (1995).
10. T. D. Wang, M. J. Mandella, C. H. Contag, and G. S. Kino, "Dual-axis confocal microscope for high-resolution in vivo imaging," *Optics Letters* **28**, 414-416 (2003).
11. A. H. Voie, D. H. Burns, and F. A. Spelman, "Orthogonal-plane fluorescence optical sectioning: three-dimensional imaging of macroscopic biological specimens," *Journal of Microscopy* **170**, 229-236 (1993).
12. J. Huisken, J. Swoger, F. Del Bene, J. Wittbrodt, and E. H. K. Stelzer, "Optical sectioning deep inside live embryos by selective plane illumination microscopy," *Science* **305**, 1007-1009 (2004).
13. J. F. Aguilar, M. Lera, and C. J. R. Sheppard, "Imaging of spheres by confocal microscopy," *Applied Optics* **39**, 4621-4628 (2000).
14. M. Gu, C. J. R. Sheppard, and H. Zhou, "Optimization of axial resolution in confocal imaging using annular pupils," *Optik* **93**, 87-90 (1993).

15. M. Gu, T. Tannous, and C. J. R. Sheppard, "Effect of numerical aperture, pinhole size and annular pupil on confocal imaging through highly scattering media," *Optics Letters* **21**, 312-314 (1996).
16. E. H. Linfoot, and E. Wolf, "Diffraction images in systems with an annular aperture," *Proc. Phys. Soc. B* **66**, 145-149 (1953).
17. C. J. R. Sheppard, and T. Wilson, "Depth of field in the scanning microscope," *Optics Letts.* **3**, 115-117 (1978).
18. C. J. R. Sheppard, and M. D. Sharma, "Integrated intensity, and imaging through scattering media," *Journal of Modern Optics* **48**, 1517-1525 (2001).
19. M. Gu, and C. J. R. Sheppard, "Three-dimensional imaging in confocal fluorescent microscopy with annular lenses," *J. Mod. Opt.* **38**, 2247-2263 (1991).
20. C. J. R. Sheppard, W. Gong, and K. Si, "The divided aperture technique for microscopy through scattering media," *Optics Express* **16**, 17031-17038 (2008).
21. M. Gu, C. J. R. Sheppard, and H. Zhou, "Optimization of axial resolution in confocal imaging using annular pupils," *Optik* **93**, 87-90 (1993).
22. R. N. Bracewell, *The Fourier Transform and its Applications* (McGraw-Hill, New York, 1965).
23. C. J. R. Sheppard, and T. Wilson, "Depth of field in the scanning microscope," *Opt. Lett.* **3**, 115-117 (1978).
24. W. Gong, K. Si, and C. J. R. Sheppard, "Optimization of axial resolution in confocal microscope with D-shaped apertures," *Appl. Opt.* **48**, 3998-4002 (2009).
25. W. Gong, K. Si, and C. J. R. Sheppard, "Improvements in confocal microscopy imaging using serrated divided apertures," *Opt. Commun.* **282**, 3846-3849 (2009).
26. W. Gong, K. Si, N. G. Chen, and C. J. R. Sheppard, "Improved spatial resolution in fluorescence focal modulation microscopy," *Optics Letters* **34**, 3508-3510 (2009).
27. N. G. Chen, C. H. Wong, and C. J. R. Sheppard, "Focal modulation microscopy," *Opt Express* **16**, 18764-18769 (2008).
28. K. Si, W. Gong, N. G. Chen, and C. J. R. Sheppard, "Penetration depth in two-photon focal modulation microscopy," *Optics Letters* (submitted).

Chapter 5 One-photon focal modulation microscopy

5.1 Introduction

The principle of confocal microscopy is to physically reject out-of-focus light with the use of a small pinhole. Due to the optical sectioning capability, confocal microscopy can be utilized to construct the three-dimensional (3D) images, using a scanning system. With these advantages, confocal microscopy has wide applications in biological science and medical imaging [1-3]. However, confocal microscopy has the essential weakness of low penetration depth compared with some other modalities. When applied to thick tissue where multi-scattering dominates, the mechanism of confocal microscopy for rejection of out-of-focus light is insufficient. To enhance background rejection, several technologies have been developed to either increase the penetration depth or improve the spatial resolution. One of these technologies is multi-photon microscopy (MPM), which utilizes long-wavelength light to excite fluorophores within the specimen being observed. In MPM, excitation is effectively restricted to a tiny focal volume, resulting in a high degree of rejection of out-of-focus light [4-6]. This selection mechanism is effective when the imaging depth is less than 1mm [7]. Mertz *et al.* developed a differential-aberration two-photon microscope, which utilizes a subtraction of an aberrated image generated by a deformable mirror from an unaberrated

image, to further reject the background [8-9]. However, MPM is a very expensive technique that uses an ultra-short pulsed laser source. Besides, single-photon excitation is preferred over multi-photon excitation in some situations in which nonlinear photo-damage and availability of fluorescence probes are of concern. Another technique with deep penetration is optical coherence tomography (OCT), which utilizes the coherence gating mechanism to reject the background [10-11]. In OCT, only the backscattered or reflected light, which has a well defined optical path length and polarization state, generates the fringe signal for image formation. However, OCT is not compatible with fluorescence, which limits its applications in molecular imaging [12-15]. Recently, our group has proposed a method, named focal modulation microscopy (FMM), to maintain diffraction-limited resolution in deep regions of biological tissue (up to 600 μm) [16-21].

In the following paragraph, we theoretically investigate image formation in one-photon fluorescence focal modulation microscopy (FMM) based on scalar diffraction theory. Two kinds of objective apertures are considered, including D-shaped apertures and quadrant apertures. The three-dimensional (3D) optical transfer function (OTF) is investigated. The spatial resolution, including both axial and transverse resolution, is studied. The signal level and background rejection capability are also presented.

5.2 Principle of focal modulation microscopy

In FMM, the illumination beam is divided into two mutually parallel but spatially separated beams, one of which is then subjected to a phase delay periodically by an acoustic-optic modulator. The background rejection capability introduced by a confocal pinhole is first enhanced by angular gating technique, then further by phase modulation and demodulation procedure.

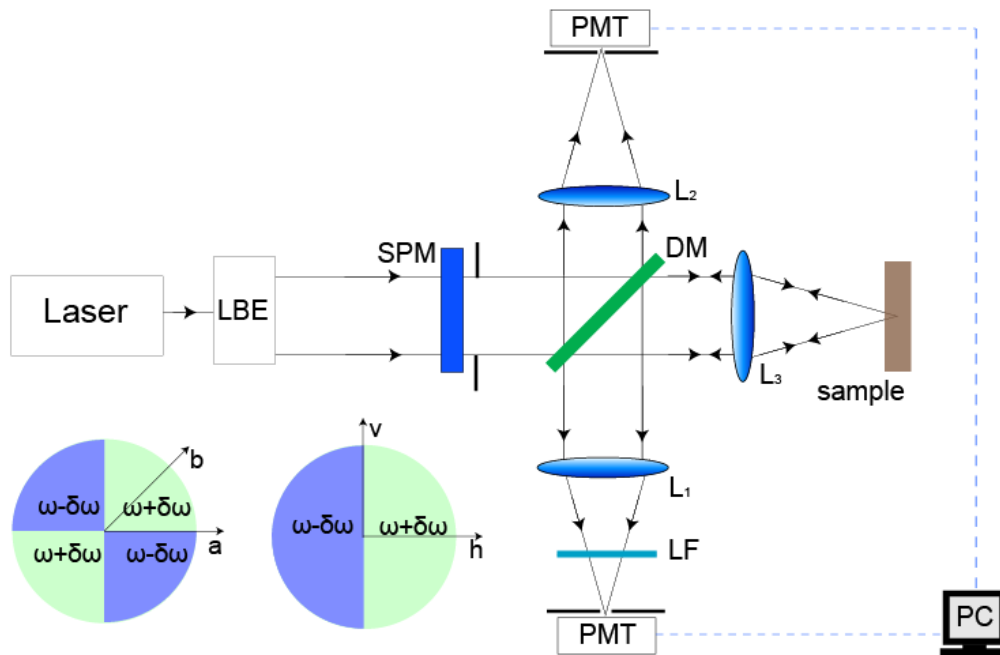


Figure 5.1 Schematic diagram of the focal modulation microscope. LBE: laser beam expander. SPM: spatial phase modulator. DM: dichroic mirror. LF: long-pass filter. PMT: photomultiplier tube. L_1 and L_2 : collection lenses. L_3 : objective lens.

A solid state single frequency laser beam is expanded by a laser beam expander (LBE). After passing through a spatial phase modulator, the two spatially separated half-beams have a relative phase shift periodically ($2\delta\omega t$)

between 0 and π . The phase modulated beam then passes through a dichroic mirror to an objective and a photomultiplier tube with a very small size pinhole in front of it for reference signal. Fluorescence emission, if any, is collected by the same objective, and the excitation light is rejected by a long-pass filter. Another photomultiplier tube is applied to convert the detected weak light signal to an electrical signal, which is further enhanced by an amplifier before being digitized into a personal computer. The resulting FMM signal as well as the reference signal are collected and demodulated by a lock-in amplifier. Note that the layout of FMM is identical to that of a standard confocal fluorescence microscope except that a spatial phase modulator (SPM) is inserted in the illumination laser beam path. As illustrated, two geometries of SPM can be applied to FMM, introducing D-shaped and quadrant..

To simplify the theoretical analysis, we assume that the emission and excitation light have the same wavelength λ . According to scalar diffraction theory, the illumination pattern can be expressed as:

$$\begin{aligned}
 I_{ill}(v_x, v_y, u) &= \left| h_{1A}(v_x, v_y, u) + h_{1B}(v_x, v_y, u) e^{i2\delta\omega t} \right|^2 \\
 &= \left(|h_{1A}|^2 + |h_{1B}|^2 \right) + 2 \operatorname{Re} \left(h_{1A} h_{1B}^* \right) \cos 2\delta\omega t + 2 \operatorname{Im} \left(h_{1A} h_{1B}^* \right) \sin 2\delta\omega t,
 \end{aligned} \tag{5.1}$$

Thus, the corresponding 3D time-varying image of a point object with a point detector can be described as [19-20]:

$$I(v_x, v_y, u) = \left(|h_{1A}|^2 + |h_{1B}|^2 \right) |h_2|^2 + 2 \operatorname{Re} \left(h_{1A} h_{1B}^* \right) |h_2|^2 \cos 2\delta\omega t + 2 \operatorname{Im} \left(h_{1A} h_{1B}^* \right) |h_2|^2 \sin 2\delta\omega t, \quad (5.2)$$

where * denotes the conjugate operation. Re and Im denote the real part and imaginary part, respectively. Here $2\delta\omega t$ is the instantaneous relative phase shift of the two beams. h_{1A} and h_{1B} are the 3D amplitude point spread functions (APSF) of the quadrant illumination apertures. h_2 is the APSF of the collection lens. According to scalar diffraction theory, they are defined by

$$h_{1A,1B,2}(v_x, v_y, u) = \iint P_{1A,1B,2}(\rho_x, \rho_y) e^{iu(\rho_x^2 + \rho_y^2)/2} e^{-i(v_x \rho_x + v_y \rho_y)} d\rho_x d\rho_y, \quad (5.3)$$

where P_{1A} and P_{1B} are the pupil functions of the objective lenses, respectively, and P_2 is the pupil function of the collection lens. These expressions can also be applied to other non-overlapping geometries for the pupils P_{1A} and P_{1B} . Here the optical coordinates are related to the true distances from the focal point x , y , z by $v_x = (2\pi/\lambda)xn \sin \alpha$, $v_y = (2\pi/\lambda)yn \sin \alpha$, $u = (8\pi/\lambda)zn \sin^2(\alpha/2)$, with λ the excitation or emission wavelength, α the semi-angular aperture of the lens, and n the refractive index of the immersion medium. The coordinates ρ_x , ρ_y are distances in the pupil plane, normalized by the pupil radius r .

The detected image signal is then sent to a lock-in amplifier. After demodulation, two signals, the in-phase signal I_{in} and quadrature signal I_{qu} , can be obtained. They can be expressed as [19]:

$$I_{in} = 2 \operatorname{Re} \left(h_{1A} h_{1B}^* \right) |h_2|^2, \quad (5.4)$$

$$I_{qu} = 2 \operatorname{Im}(h_{1A} h_{1B}^*) |h_2|^2. \quad (5.5)$$

Note that the in-phase signal I_{in} can be also simply expressed as the difference between two confocal signals obtained when the two spatial separated illumination beams are in-phase and anti-phase,

$$\begin{aligned} I_{in} &= 2 \operatorname{Re}(h_{1A} h_{1B}^*) |h_2|^2 \\ &\propto |h_{1A} + h_{1B}|^2 |h_2|^2 - |h_{1A} - h_{1B}|^2 |h_2|^2. \end{aligned} \quad (5.6)$$

Because of the linear form of Eq. 5.4 and Eq. 5.5, image formation is linear in intensity, and hence the image of a point object can be regarded as an intensity point spread function (IPSF). However, in focal modulation microscopy at present we only use the in phase signal I_{in} . However, we believe that by certain clever combinations of the in-phase signal I_{in} and quadrant signal I_{qu} , the performance of FMM can be further improved.

5.3 Optical transfer function

The 3D optical transfer function (OTF) for FMM is given by the 3D Fourier transform of IPSF, which can be expressed as [20]

$$C(m, n, s) = F_3 \left[\operatorname{Re}(h_{1A}(v_x, v_y, u) h_{1B}^*(v_x, v_y, u)) \left(|h_2(v_x, v_y, u)|^2 \otimes_2 D(v_x, v_y) \right) \right], \quad (5.7)$$

where m and n are the radial spatial frequencies normalized by $n \sin \alpha / \lambda$, and s is the axial spatial frequency normalized by $n \sin^2(\alpha/2) / \lambda$. F_3 denotes the 3D Fourier transform operation. $D(v_x, v_y)$ is the intensity sensitivity of the detector,

which is restricted to the area within a normalized radius v_d . Figure 5.2 compares the 3D OTFs of confocal microscopy (CM) with FMM with D-shaped apertures (DFMM) and with quadrant apertures (QFMM) for various values of the detector radii v_d . The 3D OTFs are normalized to unity by $C(0,0,0)$. For a point detector, as expected, the transverse and axial cut-off spatial frequencies of both CM and QFMM systems are 4 and 1, respectively. However, the high spatial frequency region where the 3D OTF has appreciable values for both DFMM and QFMM is broader than for CM. This phenomenon becomes more obvious when the detector size v_d increases. The broadening of the 3D OTF results in a superior response at high spatial frequencies, which implies that more energy is distributed at higher angles of diffraction in both DFMM and QFMM than in CM. Thus, an improved spatial resolution can be achieved. It can be noticed that in DFMM the high frequency region is much broader in the horizontal (m) direction than in the vertical (n) direction, which is due to the asymmetric geometry of D-shaped apertures, while in QFMM, the 3D OTF behaves nearly the same in different directions for a point detector. As v_d increases, the difference in the 3D OTF in directions a and b of QFMM remains relatively small compared with DFMM, resulting in a less imaging asymmetry.

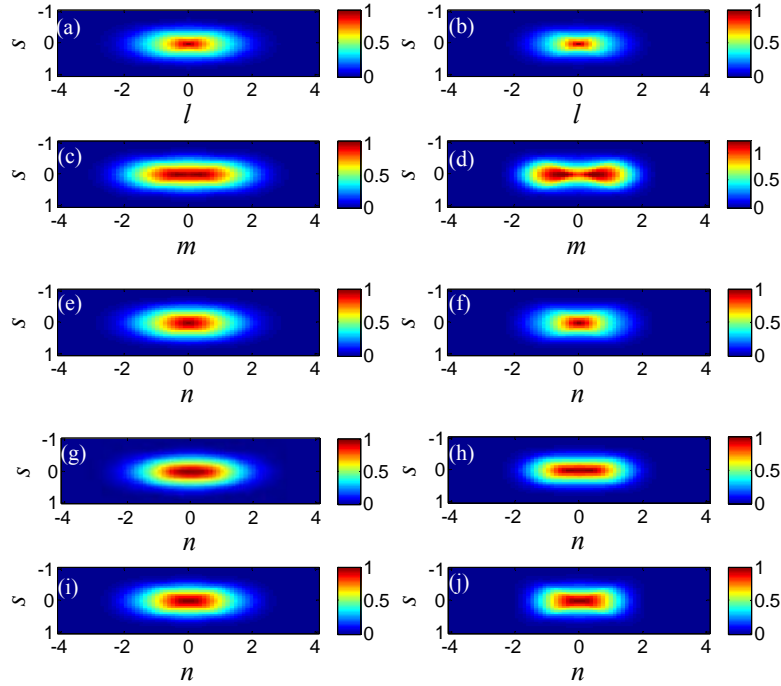


Figure 5.2 Three dimensional optical transfer functions for: (a) CM with a point detector; (b) CM with $v_d = 3$; (c) DFMM in horizontal direction with a point detector; (d) DFMM in horizontal direction with $v_d = 3$; (e) DFMM in vertical direction with a point detector; (f) DFMM in vertical direction with $v_d = 3$; (g) QFMM in direction a with a point detector; (h) QFMM in direction a with $v_d = 3$; (i) QFMM in direction b with a point detector; (j) QFMM in direction b with $v_d = 3$.

5.4 Axial resolution

In confocal fluorescence microscopy, the axial resolution can be characterized by the measurement of the axial response of an infinitely-thin fluorescent layer. The axial response is the Fourier transform of the axial cross-section of the 3D OTF with respect to s , giving the strength of optical sectioning: the narrower the axial response, the less the cross-talk between two adjacent sections of the images and therefore the higher the axial resolution [22].

The axial cross-sections of the 3D OTF of CM, DFMM and QFMM, $C(0,0,s)$, normalized by $C(0,0,s)$ are shown in Figure 5.3, for a point detector and finite-size detector, respectively. When $v_d = 0$, as expected, all the $C(0,0,s)$ are cut off at the frequency of 1. However, the ones for DFMM and QFMM overlap each other and are broader than CM, implying that compared with CM, the improvement of axial resolution of DFMM and QFMM are the same. As v_d increases, $C(0,0,s)$ of QFMM becomes even slightly broader than for DFMM, showing that the optical sectioning property of QFMM can be better than DFMM.

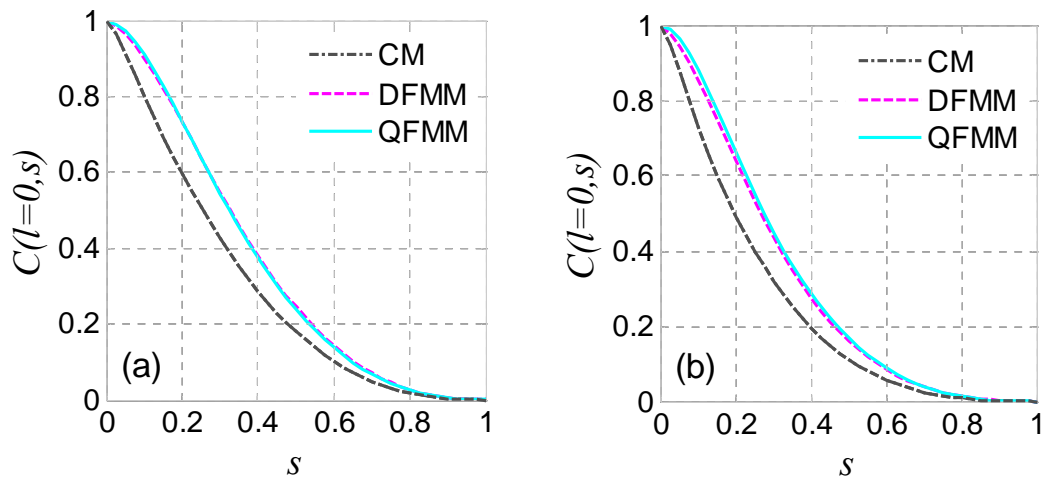


Figure. 5.3 The axial cross-sections of the 3D OTF of CM, DFMM and QFMM for (a) a point detector; (b) a finite size detector with $v_d = 3$.

An alternative model for the determination of the axial resolution is to image a thick uniform fluorescent layer scanned in the axial direction [23]. In this case, the sharper axial response of the layer corresponds to a higher axial resolution. In practice, this model is more useful as it is easier to prepare a

thick fluorescent layer. For a thick fluorescent layer, the corresponding object function $O_f(x,y,z)$ is

$$O_f(x,y,z) = \begin{cases} 1, & z \geq 0 \\ 0, & z < 0 \end{cases}, \quad (5.8)$$

and its spatial spectrum $O(m,n,s)$ is given by

$$O(m,n,s) = \delta(m)\delta(n) \left(\frac{\delta(s)}{2} + \frac{1}{2\pi i s} \right). \quad (5.9)$$

The fluorescence image can be calculated by the 3D Fourier transform of the 3D OTF multiplied by the spatial spectrum of the object. Therefore, the image intensities of the thick fluorescent layer can be expressed as [20]

$$I(u) = \frac{1}{2} + \frac{1}{\pi} \int_0^{s_c} C(m=0, n=0, s) \frac{\sin(us)}{s} ds, \quad (5.10)$$

where s_c is the axial cut-off spatial frequency. Here $s_c=1$.

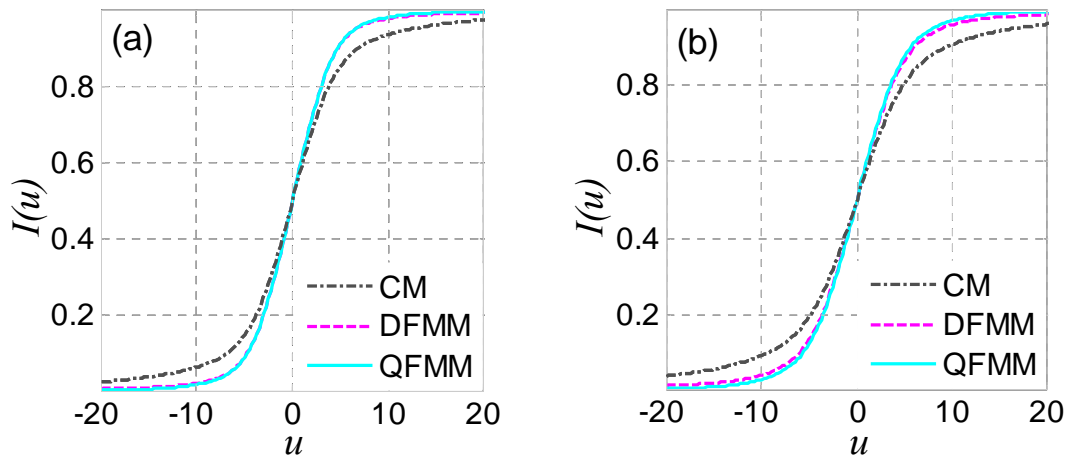


Figure 5.4 Images of a thick fluorescent layer for CM, DFMM and QFMM with (a) a point detector; (b) a finite size detector with $v_d = 3$.

Figure 5.4 describes the images of a thick fluorescent layer for CM, DFMM and QFMM with various detector sizes. It can be noticed that both DFMM and QFMM can obtain a better axial resolution than CM, irrespective of the detector size. Also, for a point detector the axial resolution is the same for DFMM and QFMM. When the detector size increases, the axial resolution of QFMM becomes slightly superior to DFMM. For example, when $v_d = 3$, compared with CM, the gradient of the image at $u = 0$ is improved by 23.4% and 27.2% for DFMM and QFMM, respectively.

5.5 Transverse resolution

The image performance of FMM can be demonstrated by simulating the image of a radial spoke pattern. Assume that a thin radial spoke pattern can emit fluorescence light with a strength $o_f(v_x, v_y, u = 0)$. The image of the radial spoke pattern is then given by [24]

$$I(v_x, v_y, u) = I_m(v_x, v_y, u) \otimes_3 o_f(v_x, v_y, u = 0), \quad (5.11)$$

where \otimes_3 denotes the 3-D convolution operation. Fig. 5.5 compares the images of a radial spoke pattern at the focal plane for CM, DFMM and QFMM, respectively, for various values of the detector radii v_d . It can be noticed that the transverse resolution of DFMM is asymmetric due to the asymmetric property of the two D-shaped illumination apertures. In DFMM, super-transverse resolution can be obtained in the horizontal direction.

However, it is gradually degraded when deviating from the horizontal direction to the vertical direction. The different resolution in horizontal and vertical direction may cause a confusing inspection in biological science or medical diagnosis. However, in QFMM, when $v_d = 3$ the transverse resolution remains nearly the same in different directions, both of which are superior to CM.

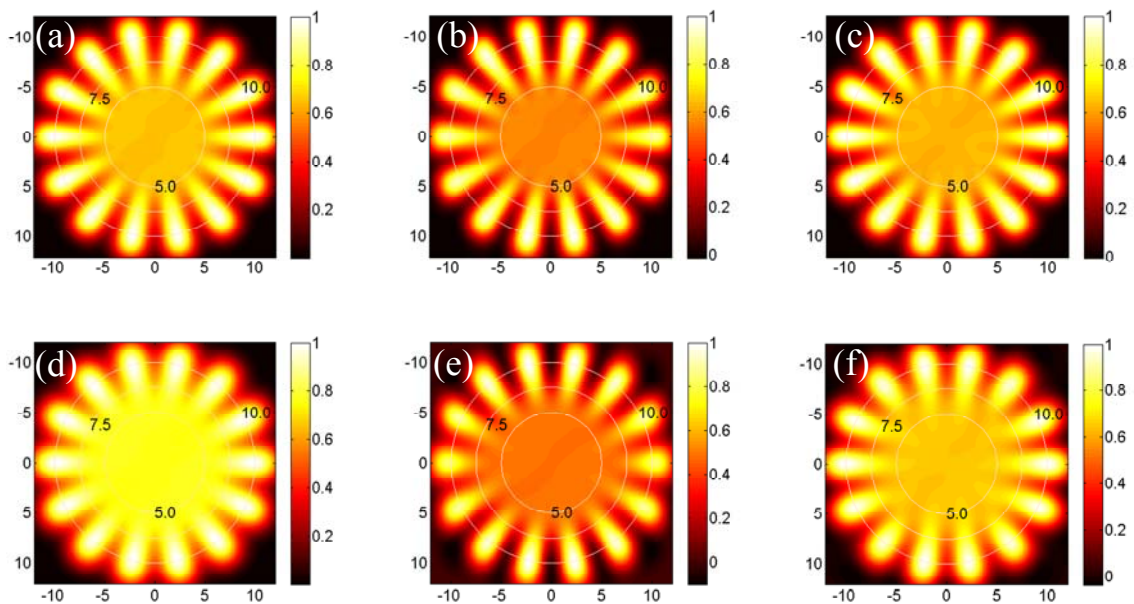


Figure 5.5 Images of a radial spoke pattern at the focal plane for (a) CM with a point detector; (b) DFMM with a point detector; (c) QFMM with a point detector; (d) CM with $v_d = 3$; (e) DFMM with $v_d = 3$; (f) QFMM with $v_d = 3$. The horizontal and vertical axes are in units of v .

Theoretically, the transverse resolution in confocal fluorescence imaging is determined by the transverse cutoff spatial frequency and transverse response of the 3D OTF. One of the methods for quantitatively characterizing the transverse resolution is to consider the image of a sharp and straight edge scanned in the focal plane [25]. Here we first consider the image of a thick, straight and sharp fluorescent edge, then move to a thin, straight and sharp

fluorescent edge. Since the 3D OTF for FMM is not central-symmetrical, we consider the images of an edge oriented along the vertical (I_y) and horizontal (I_x) directions for DFMM, and the images of edge oriented along the a direction (I_a) and b direction (I_b) for QFMM (in Figure 5.1).

Consider a thick, straight and sharp fluorescent edge scanned in the focal plane. The corresponding image intensities of the edges of DFMM [20] can be expressed as:

$$\begin{cases} I_y(v) = \frac{1}{2} + \frac{1}{\pi} \int_0^{l_c} C(m, n=0, s=0) \frac{\sin(vm)}{m} dm, \\ I_x(v) = \frac{1}{2} + \frac{1}{\pi} \int_0^{l_c} C(m=0, n, s=0) \frac{\sin(vn)}{n} dn, \end{cases} \quad (5.12)$$

where l_c is the transverse cut-off spatial frequency. The expression for I_a is same as for I_x , while I_b can be expressed in the same form as for I_y by turning $C(m, n, s)$ through 45 degrees.

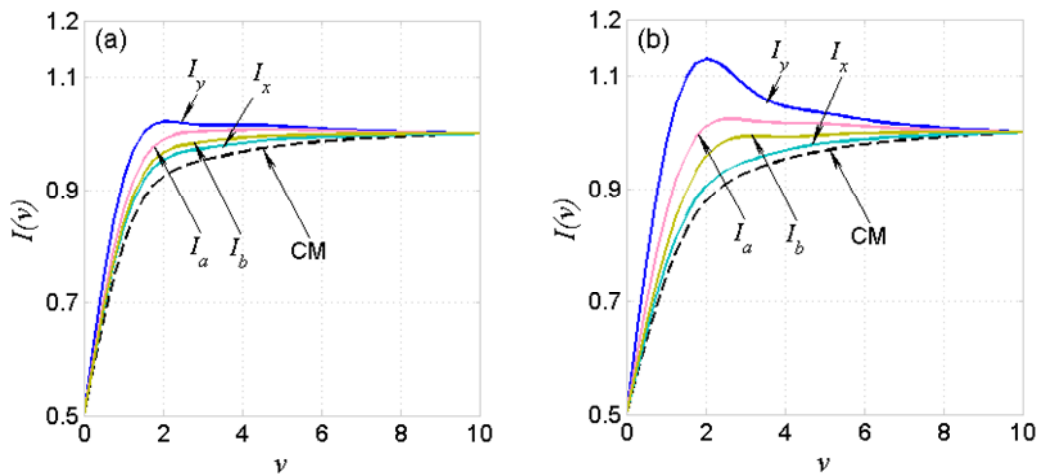


Figure 5.6 Image of a thick fluorescent edge in CM, DFMM and QFMM for (a) a point detector and (b) a finite size detector with $v_d = 3$.

The single-photon fluorescence images of a thick edge in QFMM, compared with CM and DFMM, for a point detector and a finite size detector with $v_d = 3$, respectively, are shown in Figure 5.6. The value of the image intensity is normalized to unity by its value far from the edge. The intensity at the edge is one half of its value far from the edge, as is expected for incoherent imaging [20]. It can be seen that for a given size of detector, the images obtained by either DFMM or QFMM are sharper than by CM, despite the orientation of the edge. For DFMM, when the edge is orientated along the vertical direction (I_y), super-resolution can be obtained. Compared with CM, the gradient of the image at $v = 0$ is improved from 45.9% for a point detector to 108.8% for $v_d = 3$. However, when the edge is oriented along the horizontal direction (I_x), only a slight improvement in transverse resolution can be obtained. In this case, the improvements of the gradient of the image at $v = 0$ is only 10.4% and 10.3% for a point detector and $v_d = 3$, respectively. The asymmetric property of the DFMM system sometimes may cause confusion for imaging. However, for QFMM, a high transverse resolution can also be obtained, meanwhile keeping the resolution nearly the same in different directions when the normalized detector size is smaller than 3, which is always the case in practice. The mean improvement of the gradient of QFMM in different directions is 17% and 37.5% for $v_d = 0$ and $v_d = 3$, respectively. Notes that as v_d increases, I_y and I_x become sharper at the cost of increasing the strength of a hump near the edge. This phenomenon is mainly caused by the

modulation and demodulation process. However, compared with DFMM, the strength of the hump near the edge for QFMM is dramatically reduced, thus further improving the image quality.

For the case of a thin, straight and sharp fluorescent edge scanned in the focal plane, the corresponding image intensities of the edges in the focal plane for DFMM can be derived as [20]:

$$\begin{cases} I_y(v) = \frac{1}{2} + \frac{1}{\pi} \int_0^{l_c} C_2(m, n=0) \frac{\sin(vm)}{m} dm, \\ I_x(v) = \frac{1}{2} + \frac{1}{\pi} \int_0^{l_c} C_2(m, n=0) \frac{\sin(vm)}{m} dm, \end{cases} \quad (5.13)$$

where $C_2(m, n)$ denotes the two-dimensional in-focus OTF of the DFMM, given by the projection of the 3D OTF $C(m, n, s)$ in the focal plane. The expression for I_a is the same as for I_x , while I_b can be expressed in the same form as I_y by turning $C_2(m, n)$ through 45 degrees.

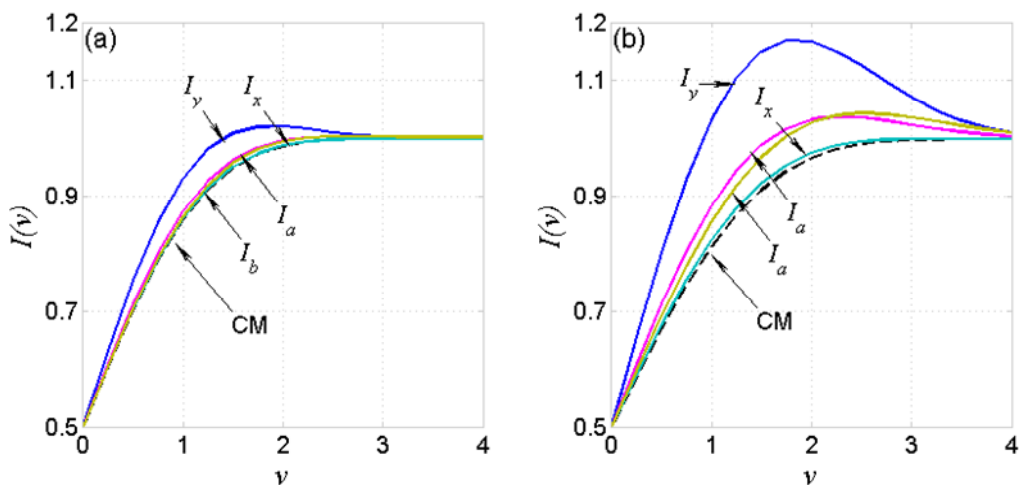


Figure 5.7 Image of a thin fluorescent edge in CM, DFMM and QFMM for (a) a point detector and (b) a finite size detector with $v_d = 3$.

Figure 5.7 compares the single-photon fluorescence images of a thin edge obtained by CM, DFMM and QFMM, for a point detector and a finite-sized detector, respectively. The value of the image intensity is normalized to unity by its value far from the edge. When the edge is orientated along the horizontal direction, the image (I_a) is slightly sharper in QFMM than CM and DFMM (I_x) for a point detector. As the detector size increases, I_a becomes much sharper in QFMM than CM and DFMM (I_x), indicating a better transverse resolution can be obtained with QFMM in vertical direction. Again, it should be noticed that the transverse resolution of DFMM is not equal in different directions due to the asymmetric properties of the D-shaped apertures. This phenomenon may cause asymmetric image deformation and confusion in biological research and medical diagnosis. As the detector size increases, the resolution difference for different directions becomes larger, indicating a larger imaging asymmetry. However, in QFMM, the transverse resolution is the same in the horizontal direction and the transverse direction, but has a small difference in the 45 degree direction. It is noted that if $v_d < 3$, which is usually used in practice, the difference between I_a and I_b remains sufficiently small, thus the transverse resolution improvement of QFMM can remain nearly the same in different directions.

5.6 Background rejection capability

The measurement of background signal is one of the methods to characterize imaging penetration depth. In this section, a scattering model called integrated intensity is introduced to quantitatively characterize the capability of background rejection for an optical system. In this model, we only consider single scattering and neglect the multi-scattering [19, 26]. If the intensity image of a point is $I(v, u)$, then the contribution to the background in the focal plane from a distribution of particles a distance u away is [19]

$$I_{\text{int}}(u) = \int_0^{\infty} I(v, u) v dv. \quad (5.14)$$

For a thick object focused at the top with thickness u_0 , the total background detected can be given by:

$$I_{\text{bgd}}(u_0) = \int_0^{u_0} I_{\text{int}}(u) du. \quad (5.15)$$

The total background detected by different optical systems with various detector sizes are compared directly in Figure 5.8, normalized by the intensity at the focal point. It can be noticed that compared with CM, the background signal can be suppressed by either DFMM or QFMM. For instance, given $u_0 = 15$ when $v_d = 0$, the background signal is reduced to 84.1% and 72.6% for DFMM and QFMM, respectively. As the detector size increase to $v_d = 3$, the background signal is further reduced to 53.6% and 67.3%, respectively. It should be pointed out that compared with DFMM, QFMM can nearly maintain

the system to be centro-symmetric at the cost of reducing the background rejection capability. However, as v_d increases, the relative reduction of background rejection becomes smaller.

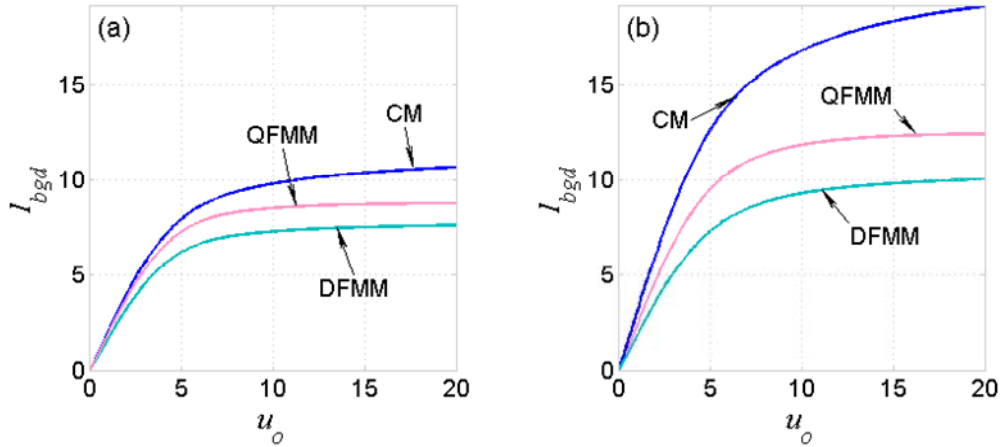


Figure 5.8 The total background normalized by intensity at focal point for CM, DFMM and QFMM at different values of v_d : (a) a point detector; (b) a finite size detector with $v_d = 3$.

5.7 Signal Level

When the detector pinhole size increases, both the signal and background increase. Therefore, in practice, the concept of signal level is introduced to describe the imaging properties [27]. The signal level for a planar object can be derived by considering the object to be a thin uniform fluorescent sheet in the focal plane [28], and is given by:

$$\eta(v_d) = \int_0^{s_c} C(m=0, n=0, s) ds, \quad (5.16)$$

where s_c is the axial cut-off spatial frequency.

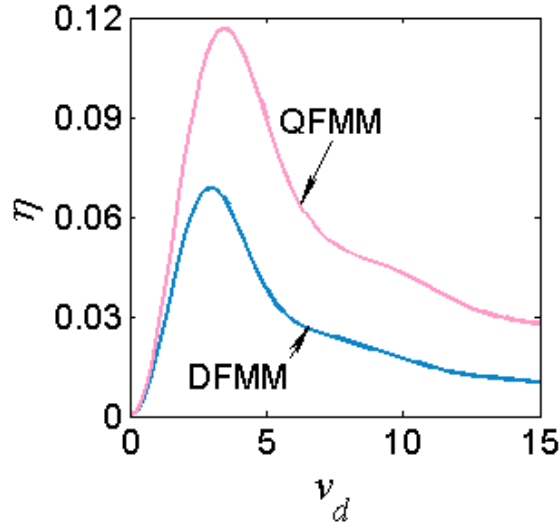


Figure 5.9 Signal level from a thin fluorescent sheet for DFMM and QFMM as a function of detector sizes.

Figure 5.9 compares the signal level η in QFMM with DFMM, as a function of normalized detector radius v_d . It can be seen that as the detector size increases, the signal level in both DFMM and QFMM first increases then decreases. The maximal value occurs at v_d around 2.8 in DFMM, while it is around 3.8 in QFMM. The reason for the occurrence of the peak signal level is because as the detector size increases, the negative value of both DFMM and QFMM becomes large enough to affect the image formation. Thus in practice, to obtain high transverse resolution, the normalized detector pinhole radius should not exceed 2.8 in DFMM and 3.6 in QFMM. In addition, the signal level in QFMM is much bigger than that in DFMM, especially with larger detector sizes. For example, when $v_d = 1$, the signal level for QFMM is increased by 31.8% compared with DFMM, while it is increased to 58.9% when $v_d = 2.8$. The signal level from a sheet is higher for QFMM because the

pupil is more spread out, so IPSTF is more concentrated. This indicates that to obtain the same amount of signal, QFMM can reduce the illumination intensity, thus can effectively reduce photon-damage and photo-bleaching. Besides, when the detector pinhole size is larger than 2.8, it is better to utilize quadrant apertures than D-shaped apertures.

5.8 Conclusion

In this chapter, we introduce one-photon focal modulation microscopy with quadrant apertures (QFMM) and D-shaped apertures (DFMM). Their imaging performance is analyzed based on diffraction theory. Numerical simulation results show that QFMM can simultaneously provide better axial resolution and transverse resolution than normal confocal microscopy. Besides, due to the symmetric geometry of the quadrant apertures, the spatial resolution in QFMM is identical in both horizontal direction and vertical direction. When the normalized detector pinhole size is smaller than 3, which is usually used in practice, QFMM can maintain the system as centro-symmetric. Thus, QFMM can greatly reduce the confusion caused in DFMM, which has a transverse resolution in horizontal direction superior to that in vertical direction. Additionally, the investigation of the background rejection capability demonstrates that compared with confocal microscopy, both DFMM and QFMM can enhance the background rejection, thus increasing the imaging

penetration depth. Note that compared with DFMM, the background rejection capability of QFMM is slightly reduced. However, the relative reduction is decreased as the detector pinhole size increases. Finally, the analysis of signal level shows that compared with DFMM, QFMM can effectively improve the signal level, implying that QFMM can reduce photon-damaging and photon-bleaching in biological science and medical diagnosis.

References

1. A. Abdelkader, E. S. M. Elewah, and H. E. Kaufman, "Confocal Microscopy of Corneal Wound Healing After Deep Lamellar Keratoplasty in Rabbits," *Arch Ophthalmol-Chic* **128**, 75-80 (2010).
2. M. A. Yaseen, V. J. Srinivasan, S. Sakadzic, W. Wu, S. Ruvinskaya, S. A. Vinogradov, and D. A. Boas, "Optical monitoring of oxygen tension in cortical microvessels with confocal microscopy," *Opt Express* **17**, 22341-22350 (2009).
3. D. S. Gareau, S. Abeytunge, and M. Rajadhyaksha, "Line-scanning reflectance confocal microscopy of human skin: comparison of full-pupil and divided-pupil configurations," *Optics Letters* **34**, 3235-3237 (2009).
4. W. Denk, J. H. Strickler, and W. W. Webb, "Two-photon laser scanning fluorescence microscopy," *Science* **248** (1990).
5. M. Oheim, E. Beaurepaire, E. Chaigneau, J. Mertz, and S. Charpak, "Two-photon microscopy in brain tissue: parameters influencing the imaging depth," *J Neurosci Meth* **111**, 29-37 (2001).
6. P. Theer, M. T. Hasan, and W. Denk, "Two-photon imaging to a depth of 1000 μm in living brains by use of a Ti:Al₂O₃ regenerative amplifier," *Opt. Lett.* **28**, 1022-1024 (2003).
7. X. Deng, and M. Gu, "Penetration depth of single-, two-, and three-photon fluorescence microscopic imaging through human cortex structures: Monte Carlo simulation," *Appl. Opt.* **42**, 3321-3329 (2003).
8. A. Leray, K. Lillis, and J. Mertz, "Enhanced background rejection in thick tissue with differential-aberration two-photon microscopy," *Biophys J* **94**, 1449-1458 (2008).
9. A. Leray, and J. Mertz, "Rejection of two-photon fluorescence background in thick tissue by differential aberration imaging," *Opt Express* **14**, 10565-10573 (2006).
10. D. Huang, E. A. Swanson, C. P. Lin, J. S. Schuman, W. G. Stinson, W. Chang, M. R. Hee, T. Flotte, K. Gregory, C. A. Puliafito, and J. G. Fujimoto, "Optical Coherence Tomography," *Science* **254**, 1178-1181 (1991).
11. J. G. Fujimoto, "Optical coherence tomography for ultrahigh resolution in vivo imaging," *Nat. Biotechnol.* **21**, 1361-1367 (2003).
12. M. R. Hee, J. A. Izatt, E. A. Swanson, D. Huang, J. S. Schuman, C. P. Lin, C. A. Puliafito, and J. G. Fujimoto, "Optical Coherence Tomography of the Human Retina," *Arch Ophthalmol-Chic* **113**, 325-332 (1995).
13. W. Drexler, A. Baumgartner, O. Findl, C. K. Hitzenberger, H. Sattmann, and A. F. Fercher, "Submicrometer precision biometry of the anterior segment of the human eye," *Invest Ophth Vis Sci* **38**, 1304-1313 (1997).

14. G. J. Tearney, M. E. Brezinski, B. E. Bouma, S. A. Boppart, C. Pitris, J. F. Southern, and J. G. Fujimoto, "In vivo endoscopic optical biopsy with optical coherence tomography," *Science* **276**, 2037-2039 (1997).
15. X. D. Li, S. A. Boppart, J. Van Dam, H. Mashimo, M. Mutinga, W. Drexler, M. Klein, C. Pitris, M. L. Krinsky, M. E. Brezinski, and J. G. Fujimoto, "Optical coherence tomography: Advanced technology for the endoscopic imaging of Barrett's esophagus," *Endoscopy* **32**, 921-930 (2000).
16. N. G. Chen, C. H. Wong, S. P. Chong, and C. J. R. Sheppard, "Real time focal modulation microscopy," *Three-Dimensional and Multidimensional Microscopy: Image Acquisition and Processing Xvii* **7570**, - 268 (2010).
17. C. H. Wong, S. P. Chong, C. J. R. Sheppard, and N. G. Chen, "Simple spatial phase modulator for focal modulation microscopy," *Appl Optics* **48**, 3237-3242 (2009).
18. N. G. Chen, C. H. Wong, and C. J. R. Sheppard, "Focal modulation microscopy," *Opt. Express* **16**, 18764-18769 (2008).
19. W. Gong, K. Si, and C. J. R. Sheppard, "Improved spatial resolution in fluorescence focal modulation microscopy," *Opt. Lett.* **34**, 3508-3510 (2009).
20. K. Si, W. Gong, and C. J. R. Sheppard, "Edge enhancement for in-phase focal modulation microscope," *App. Opt.* **48**, 6290-6295 (2009).
21. S. P. Chong, C. H. Wong, C. J. R. Sheppard, and N. G. Chen, "Focal modulation microscopy: a theoretical study," *Optics Letters* **35**, 1804-1806 (2010).
22. M. Gu, and C. J. R. Sheppard, "Three-dimensional imaging in confocal fluorescent microscopy with annular lenses," *J. Mod. Opt.* **38**, 2247-2263 (1991).
23. M. Gu, T. Tannous, and C. J. R. Sheppard, "Improved Axial Resolution in Confocal Fluorescence Microscopy Using Annular Pupils," *Opt Commun* **110**, 533-539 (1994).
24. W. Gong, K. Si, N. Chen, and C. J. R. Sheppard, "Focal modulation microscopy with annular apertures: A numerical study," *J. Biophoton.* DOI, 10.1002/jbio.200900110 (2009).
25. M. Gu, and C. J. R. Sheppard, "Image of a Straight Edge in Fiberoptic Confocal Scanning Microscopy," *Opt Commun* **94**, 485-490 (1992).
26. C. J. R. Sheppard, W. Gong, and K. Si, "The divided aperture technique for microscopy through scattering media," *Opt Express* **16**, 17031-17038 (2008).
27. M. Gu, and C. J. R. Sheppard, "Signal level of the fibre optical confocal scanning microscope," *J. Mod. Opt.* **38**, 1621-1630 (1991).
28. M. Gu, *Principles of Three-Dimensional Imaging in Confocal Microscopes* (World Scientific, 1996).

Chapter 6 Two-photon focal modulation microscopy

6.1 Introduction

Two-photon fluorescence microscopy has become a popular tool for fluorescence imaging in biology and medicine. Compared with single-photon fluorescence microscopy, a number of significant advantages have popularized two-photon fluorescence microscopy. First, the nonlinear nature of two-photon excitation limits the fluorescence generation to the focal volume at a deep position within thick samples. As a result, image quality is greatly improved and photodamage is limited. Second, the near-infrared (NIR) photons employed for two-photon excitation of visible fluorescent photons are scattered and absorbed much less by the biological tissue than the ultraviolet (UV) and visible photons used in single-photon fluorescence excitation. Therefore, deeper penetration depth can be achieved with two-photon microscopy [1-2]. These unique characteristics make two-photon excitation a very attractive technique for biomedical imaging, especially in thick samples [3-4]. The imaging depth of the two-photon technique is fundamentally limited by the onset of out-of-focus fluorescence generation near the surface of the sample [5]. The simplest methods to increase the penetration depth in the two-photon technique are to increase the laser average power, and to

optimize the collection efficiency of the microscope, by for example using non-descanned detection. However, increasing the laser average power can lead to excitation saturation, photobleaching, and photodamage. Theer *et al.* have demonstrated that the decrease of the laser repetition rate for a constant pulse length leads to increased penetration depth, and successfully extended the penetration depth to $1000\ \mu\text{m}$ in mouse brain [6]. Later on, Balu *et al.* increased the penetration depth in biological tissues by using longer excitation wavelengths [7]. Recently, Mertz *et al.* developed a differential aberration two-photon microscopy using a deformable mirror to further reject out-of-focus background. However, because two images are taken at different times, subtraction cannot fully eliminate the background [8]. This limitation can be overcome by the focal modulation technique, which, recently, has been successfully applied in single-photon fluorescence microscopy [9-12]. In this chapter, we extended single-photon fluorescence focal modulation microscopy to two-photon fluorescence focal modulation microscopy (2PFMM). A theoretical model for 2PFMM is established by combining scalar diffraction theory and a statistical model for scattering in turbid media. Image formation in 2PFMM is studied, showing that 2PFMM can improve the spatial resolution. The signal to background ratio (SNR) is also investigated. Compared with the conventional two-photon fluorescence microscopy, 2PFMM can greatly reject background, arising from both ballistic and scattered excitation. It is possible to extend the imaging penetration depth of

2PM by a factor of 3, while meanwhile improving the sectioning ability and image resolution.

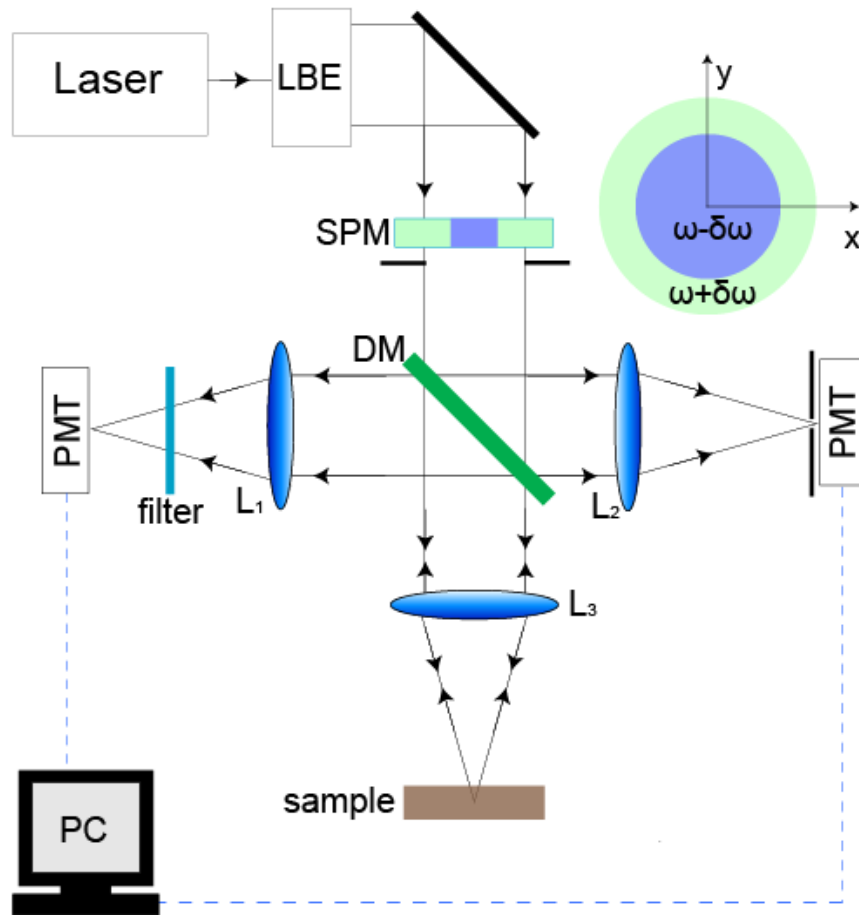


Figure 6.1. Schematic diagram of two-photon focal modulation microscopy with annular apertures. SPM: spatial phase modulator; DM: dichroic mirror; L_1 and L_2 : collection lenses; L_3 : objective lens; PMT: photomultiplier tube.

The system of 2PFMM is shown in Figure 6.1. Near-infrared light generated by a pulsed laser is expanded and then split into two spatially separated beams with an annular aperture. After passing through a spatial phase modulator, the two beams are subject to different phase delays. The excitation light exhibits an intensity modulation around the focal point. When the focal point is within a turbid medium, the excitation photons reaching the

focal point include both ballistic (unscattered) and scattered photons. The emitted fluorescence is detected by a photomultiplier tube (PMT), and finally demodulated by lock-in techniques. Only the ballistic photons contribute to modulated excitation intensity as they have well defined phase and polarization, so that the scattered light is filtered out.

6.2 Ballistic light analysis

6.2.1 3D Optical transfer function

We begin our analysis by applying scalar diffraction theory under paraxial approximation to determine the image formation of 2PFMM. Assume that the first Born approximation is valid, i.e., multiple scattering and depletion of the incident beam are neglected. To simplify the simulation, we assume that the incident wavelength is exactly twice as large as the emitted two-photon fluorescence wavelength, i.e. we neglect the Stokes' shift, which may result in a small degradation of the 3D optical transfer function (OTF). The corresponding 3D time-varying imaging intensity of a point object with an infinite size detector is given by:

$$\begin{aligned}
I(v, u, t) &= \left| h_a(v, u) + h_b(v, u) e^{i2\delta\omega t} \right|^4 \\
&= \left(|h_a|^2 + |h_b|^2 \right)^2 + |h_a|^2 |h_b|^2 \\
&\quad + 2 \left(|h_a|^2 + |h_b|^2 \right) \left(h_a^* h_b + h_a h_b^* \right) e^{i2\delta\omega t} \\
&\quad + 2 \left(|h_a|^2 + |h_b|^2 \right) \left(h_a^* h_b + h_a h_b^* \right) e^{-i2\delta\omega t} \\
&\quad + \left(h_a^* h_b h_a^* h_b e^{i4\delta\omega t} + h_a h_b^* h_a h_b^* e^{-i4\delta\omega t} \right).
\end{aligned} \tag{6.1}$$

where $2\delta\omega t$ is the instantaneous relative phase shift of the two spatially-separated beams. Here the optical coordinates u and v are related to the true distances from the focal point r , z by $v = (2\pi/\lambda)rn \sin \alpha$, $u = (8\pi/\lambda)zn \sin^2(\alpha/2)$ with λ the emission wavelength, α the semi-angular aperture of the lens, and n the refractive index of the immersion medium. $h_a(v, u)$ and $h_b(v, u)$ are the 3D amplitude point spread functions (APSF) of the two spatially separated and non-overlapping objective apertures, respectively. According to scalar diffraction theory and the paraxial approximation, these are defined by:

$$h_{a,b}(v, u) = \int_0^1 P_{a,b}(\rho) J_0(v\rho) \exp(-iu\rho/2) \rho d\rho, \tag{6.2}$$

where the coordinate ρ is the distance in the pupil plane, normalized by the pupil radius a . P_a and P_b are the pupil functions of two objective apertures. For example, P_a and P_b can be an annular objective aperture with inner and outer radii of εa and a ($0 < \varepsilon < 1$), and the circular objective aperture with radius of εa , respectively. These expressions also apply for other non-overlapping geometries for the pupils P_a and P_b .

After being demodulated at $2\delta\omega$ frequency, the ballistic intensity can be given by:

$$I_{bb} = I_b^2 = \left(h_a^*(v, u)h_b(v, u) + h_a(v, u)h_b^*(v, u) \right) \left(|h_a(v, u)|^2 + |h_b(v, u)|^2 \right), \quad (6.3)$$

where * denotes the complex conjugate operation. Note that equation 6.3 can also be expressed as the difference of the in-phase signal to the anti-phase signal,

$$I_{bb}(v, u) = |h_a(v, u) + h_b(v, u)|^4 - |h_a(v, u) - h_b(v, u)|^4 = \left(h_a^*(v, u)h_b(v, u) + h_a(v, u)h_b^*(v, u) \right) \cdot \left(|h_a(v, u)|^2 + |h_b(v, u)|^2 \right), \quad (6.4)$$

It should also be mentioned, if we demodulated at $4\delta\omega$, the ballistic intensity is given by $I_{bb}^{4\delta\omega} = (h_a h_b^* h_a h_b^* + h_a^* h_b h_a^* h_b)$. Since I_{bb} can be regarded as the intensity point spread function, the 3D optical transfer function (OTF) for AFMM is simply given by the 3D Fourier transform of I_{bb} , which can be expressed as:

$$C(l, s) = F_3 \left[\left(h_a(v, u)h_b^*(v, u) + h_a^*(v, u)h_b(v, u) \right) \left(|h_a(v, u)|^2 + |h_b(v, u)|^2 \right) \right], \quad (6.5)$$

where $l = \sqrt{m^2 + n^2}$ is the radial spatial frequency normalized by $\sin \alpha / \lambda$, and s is the axial spatial frequency normalized by $4 \sin^2(\alpha/2) / \lambda$. F_3 denotes the 3D Fourier transform operation.

Figure 6.2 illustrates the 3D OTF of 2PFMM with annular apertures ($\varepsilon = \sqrt{2}/2$) and D-shaped apertures ($d = 1$), compared with 2PM, respectively. It can be noticed that although the cut-off frequencies of the 3D OTF of 2PFMM are the same as 2PM, in the high frequency region, 3D OTF

of 2PFMM is broader than 2PM in both annular and D-shaped apertures, which indicates that better spatial resolution can be achieved by 2PFMM. In addition, annular 2PFMM has the advantage in the axial resolution, while D-shaped 2PFMM in the transverse resolution.

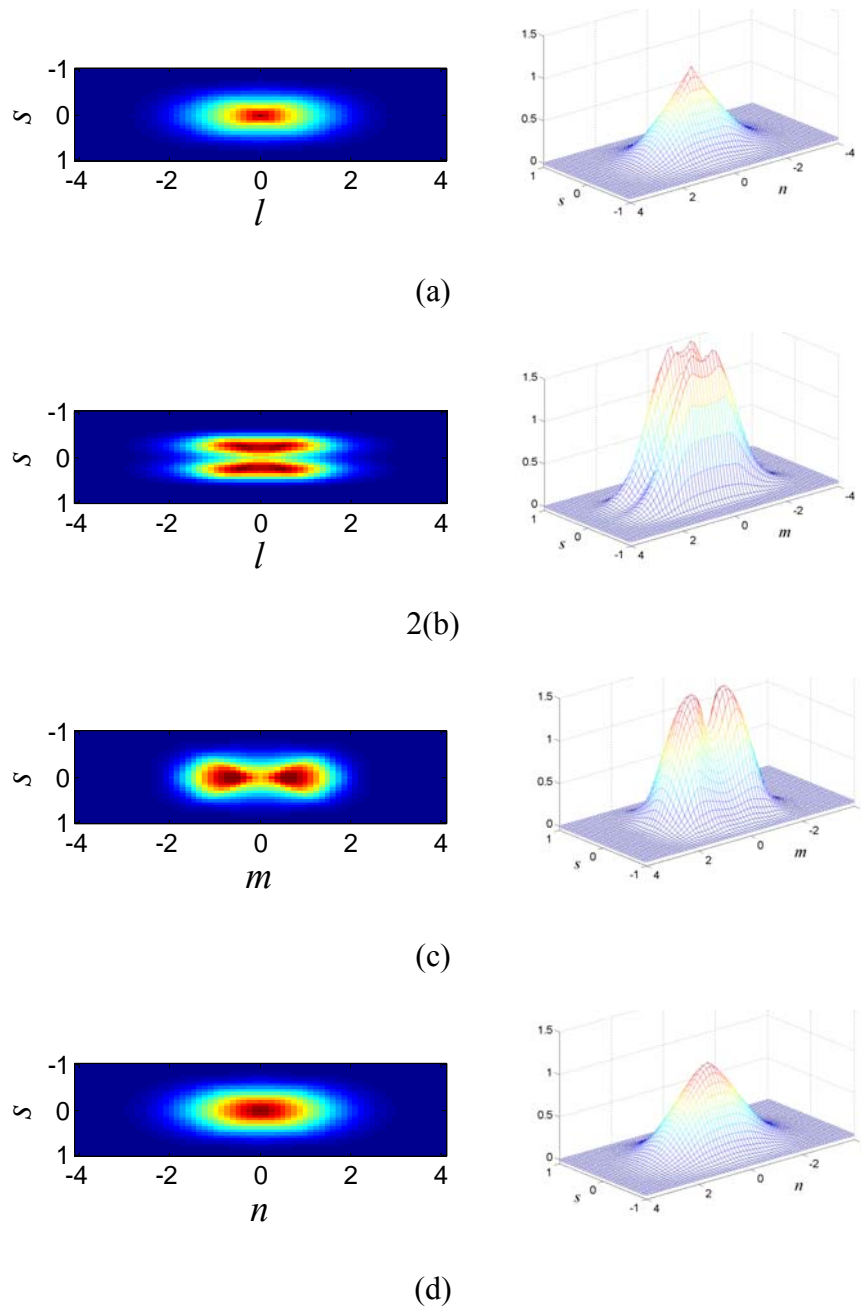


Figure 6.2 The 3D OTF of (a) 2PM and (b) 2PFMM with annular apertures; (c) 2PFMM with D-shaped apertures in m direction ($n=0$); (d) 2PFMM with D-shaped apertures in n direction ($m=0$).

6.2.2 Axial resolution

A model for the determination of the axial resolution is to image a thick uniform fluorescent layer scanned in the axial direction [13]. In this case, the sharper axial response of the layer corresponds to a higher axial resolution. In practice, this model is useful as it is easy to prepare a thick fluorescent layer.

For a thick fluorescent layer, the corresponding object function $o_f(x,y,z)$ is:

$$o_f(x,y,z) = \begin{cases} 1, & z \geq 0 \\ 0, & z < 0 \end{cases} \quad (6.6)$$

and its spatial spectrum $O(m,n,s)$ is given by

$$\begin{aligned} O(m,n,s) &= F_3(o_f(x,y,z)) \\ &= \delta(m)\delta(n) \left(\frac{\delta(s)}{2} + \frac{1}{2\pi is} \right). \end{aligned} \quad (6.7)$$

The corresponding fluorescence image is given by the 3D inverse Fourier transform of the product of the 3D OTF and the object spectrum. Therefore, the image intensities of the thick fluorescent layer can be expressed as,

$$I(u) = \frac{1}{2} + \frac{1}{\pi} \int_0^{s_c} C(m=0, n=0, s) \frac{\sin(us)}{s} ds, \quad (6.8)$$

where s_c is the axial cut-off spatial frequency. Here $s_c = 1$.

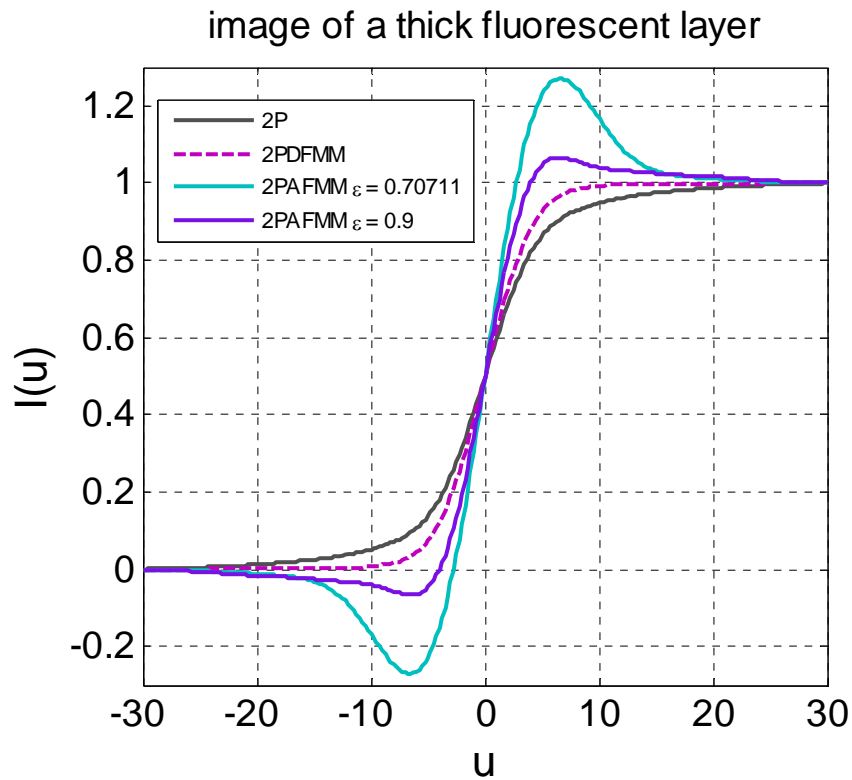


Figure 6.3 Images of a thick uniform fluorescent layer scanning in the axial direction for two-photon excitation fluorescence microscopy (2P), 2PFMM with D-shaped apertures (2PDFMM), and 2PFMM with annular apertures (2PAFMM), respectively.

Figure 6.3 compares the images of a thick uniform fluorescent layer among 2PM, 2PFMM with D-shaped apertures and 2PFMM with annular apertures, respectively. It shows that the images obtained by 2PFMM with annular apertures and D-shaped apertures are both sharper than 2PM, implied that 2PFMM can improve axial resolution than 2PM. Note that 2PFMM with annular apertures displays sharper images than 2PFMM with D-shaped apertures. This confirms again that 2PFMM with annular apertures is superior in the improvement of axial resolution. A similar phenomenon was reported for one-photon focal modulation microscopy [14]. It is found that although a hump with a relatively big value appears near the edge surface, 2PFMM with

equal-area annular apertures can achieve the best the axial resolution. This is due to the fact that the anti-phase signal $|h_a(v,u) - h_b(v,u)|^4$ generated by equal-area apertures can only produce an out-of-focus background while keeping the intensity at the focal point zero. Thus after subtracted by the in-phase signal $|h_a(v,u) + h_b(v,u)|^4$, the background of 2PFMM is suppressed while the intensity at the focal point keeps the maximum value.

6.2.3 Transverse resolution

The image of a sharp edge scanned in the transverse direction is considered, as a characterization of the transverse resolution [15]. Assume a thick, straight and sharp fluorescent edge scanned in the focal plane. Due to the non-centrosymmetric properties of two D-shaped apertures, two extreme cases for the orientation of an edge need to be considered. One is the fluorescent edge $o_{x \geq 0}(x, y, z)$ oriented parallel to the stripe between the two D-shaped apertures; the other $o_{y \geq 0}(x, y, z)$ is perpendicular to the stripe, expressed as:

$$\begin{cases} o_{x \geq 0}(x, y, z) = \begin{cases} 1, & x \geq 0 \\ 0, & x < 0 \end{cases} \\ o_{y \geq 0}(x, y, z) = \begin{cases} 1, & y \geq 0 \\ 0, & y < 0 \end{cases} \end{cases} \quad (6.9)$$

The corresponding image intensities of the edges of 2PFMM can be expressed as:

$$\begin{cases} I_{x \geq 0}(v) = \frac{1}{2} + \frac{1}{\pi} \int_0^{l_c} C(m=0, n, s=0) \frac{\sin(vn)}{n} dn, \\ I_{y \geq 0}(v) = \frac{1}{2} + \frac{1}{\pi} \int_0^{l_c} C(m, n=0, s=0) \frac{\sin(vm)}{m} dm. \end{cases} \quad (6.10)$$

for D-shaped apertures and

$$I(v) = \frac{1}{2} + \frac{1}{\pi} \int_0^{l_c} C(l, s=0) \frac{\sin(vl)}{l} dl, \quad (6.11)$$

for annular apertures, where l_c is the transverse cut-off spatial frequency.

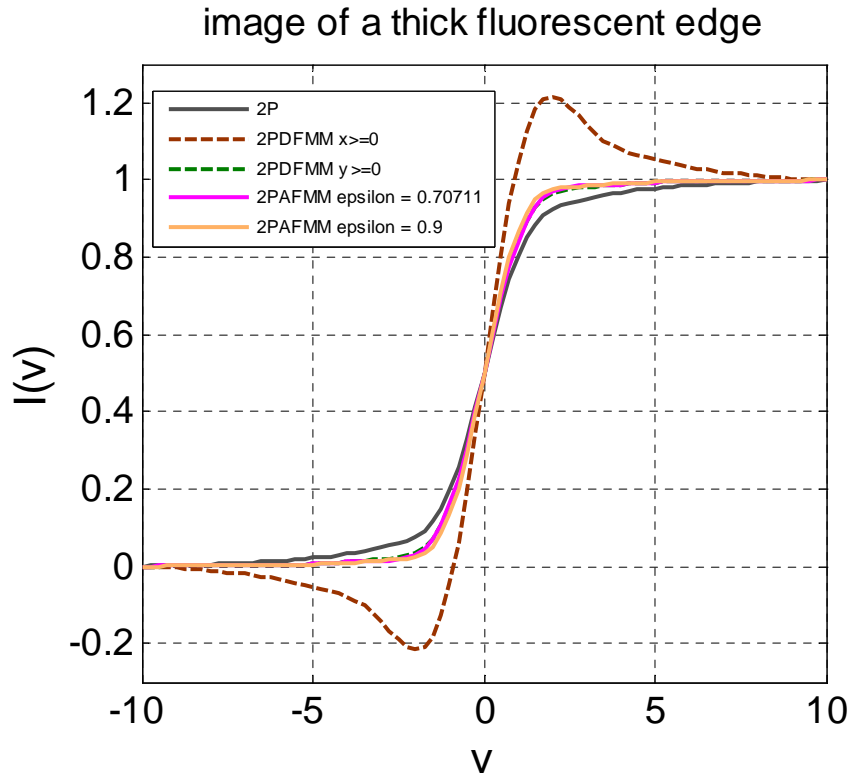


Figure 6.4 Images of a thick, sharp and straight fluorescent edge scanned in the transverse direction for two-photon excitation fluorescence microscopy (2P), 2PFMM with D-shaped apertures (2PDFMM), and 2PFMM with annular apertures (2PAFMM), respectively.

The comparison of the images of a thick, sharp and straight fluorescent edge for 2PM, 2PFMM with D-shaped apertures and 2PFMM with annular

apertures is shown in Figure 6.4. As expected from the analysis of the 3D OTF, 2PFMM can obtain sharper images than 2PM with either D-shaped apertures or annular apertures. However, from the view of transverse resolution, 2PFMM with D-shaped apertures is superior to annular apertures. Note that for one-photon FMM, even for a point detector, compared with D-shaped apertures, annular apertures can simultaneously improve the transverse resolution and the strength of optical sectioning [14]. It is also noted that for 2PFMM with annular apertures, the best transverse resolution can be obtained if the two apertures have same area ($\varepsilon = \sqrt{2}/2$).

An alternative method to characterize the transverse resolution is to scan a thin, straight and sharp fluorescent edge in the focal plane. The corresponding image intensities are

$$\begin{cases} I_{x \geq 0}(v) = \frac{1}{2} + \frac{1}{\pi} \int_0^{l_c} C_2(m=0, n) \frac{\sin(vn)}{n} dn, \\ I_{y \geq 0}(v) = \frac{1}{2} + \frac{1}{\pi} \int_0^{l_c} C_2(m, n=0) \frac{\sin(vm)}{m} dm, \end{cases} \quad (6.12)$$

for 2PFMM with D-shaped apertures, and

$$I(v) = \frac{1}{2} + \frac{1}{\pi} \int_0^{l_c} C_2(l) \frac{\sin(vl)}{l} dl, \quad (6.13)$$

for 2PFMM with annular apertures, where $C_2(m, n)$ denotes the two-dimensional in-focus OTF of the DFMM, given by the projection of the 3D OTF $C(m, n, s)$ in the focal plane.

The images of a thin, sharp and straight fluorescent edge are shown in Figure 6.5 for 2PM and 2PFMM with D-shaped apertures and annular apertures, respectively. It confirms that compared with 2PM, 2PFMM can improve the transverse resolution. Moreover, 2PFMM can achieve the best transverse resolution if D-shaped apertures are applied. For 2PFMM with annular apertures, best transverse resolution can be reached when the two apertures have equal area.

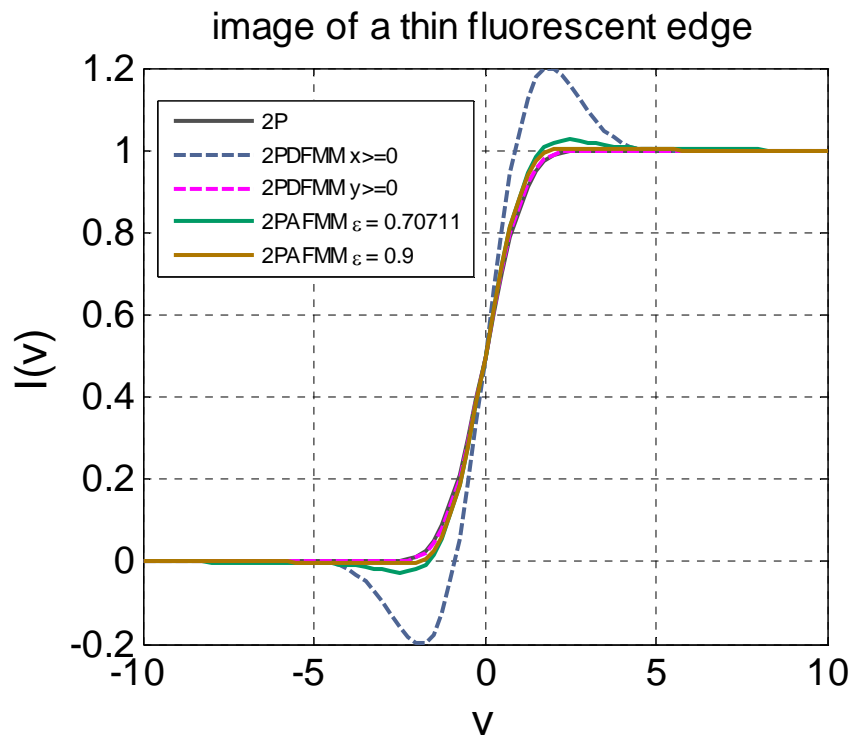


Figure 6.5 Images of a thin, sharp and straight fluorescent edge scanned in the transverse direction for two-photon excitation fluorescence microscopy (2P), 2PFMM with D-shaped apertures (2PDFMM), and 2PFMM with annular apertures (2PAFMM), respectively.

6.3 Multiple-scattering analysis

The ballistic light can be determined quite accurately with the above formula. However, it is difficult to calculate the scattered contribution. The

propagation of pulsed laser radiation through turbid media has been investigated using several different approaches including radiative transfer models [16-17], and Monte Carlo simulations [18]. Recently, analytical methods using simple statistical concepts were developed to treat scattering in turbid water [19-20], and further applied to investigate the imaging depth limit in two-photon microscopy [21]. Assuming that scattering is dominant and absorption negligible, this is appropriate for most biological tissues. Assuming that the variance of the transverse spread for a pulsed unidirectional beam incident on a medium corresponds to a Gaussian distribution, the variance of the transverse spread (σ_r^2) and the variance of the temporal spread (σ_t^2) for a pulsed unidirectional beam incident on a medium with highly anisotropic scattering are given by [20]:

$$\begin{aligned}\sigma_r^2(z) &= \frac{z^3}{3l_s} \langle \Theta^2 \rangle, \text{ and} \\ \sigma_t^2(z) &= \frac{z^3}{12c^2l_s} \langle \Theta^4 \rangle + \frac{z^4}{24c^2l_s^2} \langle \Theta^2 \rangle^2,\end{aligned}\tag{6.14}$$

respectively, with $\Theta = 2 \sin(\theta/2)$ and θ the scattering angle. Here z is the axial distance, c is the speed of light, l_s is the scattering-mean-free-path length, $\alpha = 1/l_s$, where μ_s is the scattering coefficient. The symbol $\langle \rangle$ represents the statistical average, i.e. the moments of Θ . The moments of Θ can be calculated with [22]:

$$\langle x^n \rangle = \frac{1}{2} \int_{-1}^1 x^n p(x) dx,\tag{6.15}$$

where $x = \cos \theta$ and $p(x)$ is the scattering phase function. In biological tissue optics, the phase function is usually well approximated with the aid of the postulated Henyey-Greestein function:

$$p(\theta) = \frac{1}{4\pi} \cdot \frac{1 - g^2}{(1 + g^2 - 2g \cos \theta)^{3/2}}, \quad (6.16)$$

where g is the scattering anisotropy factor

$$g = \langle \cos \theta \rangle = \int_0^\pi p(\theta) \cos \theta \cdot 2\pi \sin \theta d\theta, \quad (6.17)$$

and the normalization $\int_0^\pi p(\theta) 2\pi \sin \theta d\theta = 1$. The value of g varies in the range from 0 to 1. $g = 0$ corresponds to isotropic scattering and $g = 1$ to total forward scattering. Using Eq. 6.15, the second moment is given by:

$$\langle \cos^2 \theta \rangle = \frac{1}{2} \int_{-1}^1 x^2 p(x) dx = \frac{1}{3} (1 + 2g^2), \quad (6.18)$$

Thus $\langle \Theta^2 \rangle = 2(1 - g)$, $\langle \Theta^4 \rangle = (8/3)(1 - g)(2 - g)$. Hence the variance of the transverse spread σ_r^2 and the variance of the temporal spread σ_t^2 can be reduced to:

$$\begin{aligned} \sigma_r^2(z) &= \frac{2z^3}{3l_s} (1 - g), \text{ and} \\ \sigma_t^2(z) &= \frac{2z^3}{9c^2 l_s} (g - 2)(g - 1) + \frac{z^4}{6c^2 l_s^2} (1 - g)^2. \end{aligned} \quad (6.19)$$

The Gaussian beam can be viewed as being made up of a fan of rays travelling at various angles to the optical axis towards a common focus. Therefore, the approximation of the effective temporal and transverse spatial beam widths is:

$$\begin{aligned}\tau_{eff}(z) &= \sqrt{\tau_0^2 + 4\sigma_r^2(z)}, \text{ and} \\ w_{eff}(z) &= \sqrt{w^2(z) + 2\sigma_r^2(z)},\end{aligned}\tag{6.20}$$

where τ_0 and $w(z)$ are the $1/e^2$ temporal and lateral widths of a pulsed Gaussian beam in free space, respectively. For a Gaussian beam focused at

$$z = z_0, \quad w(z) = 2\sqrt{\frac{\lambda((z - z_0)^2 + z_r^2)}{4\pi n z_r + \lambda\alpha(z - z_0)}}, \quad z_r = \frac{w_0}{\theta_{1/e^2}} = \frac{\lambda}{n\pi\theta_{1/e^2}^2}, \quad w_0 = \sqrt{\frac{\lambda z_r}{n\pi}},$$

where λ is the wavelength, $\alpha = 1/l_s$ is the scattering coefficient, n is the refractive index, w_0 is the Gaussian beam waist, θ_{1/e^2} is the far-field beam angle, which is defined as the angle between the beam contour $w(z)$ and the optical axis.

Assuming that the variances of temporal and spatial broadening pertain to a Gaussian distribution, the intensity of the scattered light can be written as [23]:

$$I_s(\rho, z) = \frac{2P_{scat}(z)}{\pi w_{eff}^2(z)} e^{-\frac{2\rho^2}{w_{eff}^2(z)}},\tag{6.21}$$

where $P_{scat}(z)$ is the scattered light flux through a transverse plane,

$P_{scat}(z) = \int_0^\infty \sqrt{\frac{2}{\pi}} \frac{E}{\tau_{eff}(z)} e^{-2t^2/\tau_{eff}^2(z)} (1 - e^{-\alpha z}) dt$, and E is the energy in a single pulse.

The total excitation intensity in conventional 2P fluorescence microscopy can be simply expressed as:

$$\begin{aligned}I_{2PM}^{total} &= \left| I_s(r, z) + |h_a(r, z) + h_b(r, z)|^2 \exp(-\alpha z) \right|^2 \\ &= I_{2PM}^{bb} + I_{2PM}^{bs} + I_{2PM}^{ss}.\end{aligned}\tag{6.22}$$

Here $I_{2PM}^{bb} = |h_a + h_b|^4 \exp(-2\alpha z)$ is the ballistic excitation, which is the desired signal. The other two terms contribute to the scattered fluorescence, where $I_{2PM}^{bs} = 2I_s \cdot |h_a + h_b|^2 \exp(-\alpha z)$ and $I_{ss} = I_s^2$.

The total effective excitation intensity after demodulation in 2PFMM, is equal to the difference between the in-phase signal and the anti-phase signal, and can be given by:

$$\begin{aligned}
I_{2PFMM}^{total} &= \left| I_s(r, z) + |h_a(r, z) + h_b(r, z)|^2 \exp(-\alpha z) \right|^2 \\
&\quad - \left| I_s(r, z) + |h_a(r, z) - h_b(r, z)|^2 \exp(-\alpha z) \right|^2 \\
&= \left[I_s(r, z) + (|h_a(r, z)|^2 + |h_b(r, z)|^2) \exp(-\alpha z) \right] \\
&\quad \times (h_a^*(r, z)h_b(r, z) + h_a(r, z)h_b^*(r, z)) \cdot \exp(-\alpha z) \\
&= I_{2PFMM}^{bb} + I_{2PFMM}^{bs}.
\end{aligned} \tag{6.23}$$

Here $I_{2PFMM}^{bb} = (h_a h_b^* + h_a^* h_b) (|h_a|^2 + |h_b|^2) \exp(-2\alpha z)$ is the ballistic excitation, which is the desired signal. $I_{2PFMM}^{bs} = I_s \cdot (h_a h_b^* + h_a^* h_b) \exp(-\alpha z)$ is related to the scattered fluorescence, which contributes to the background in 2PFMM. $\alpha = 1/l_s$ is the scattering coefficient, where l_s is the scattering-mean-free-path length. The term I_{2PFMM}^{ss} cancels, but the analogous term for Mertz's differential aberration technique does not completely cancel because I_s is different in the two terms in the first line of Eq. 6.23. Here, we neglect the absorption process since in most biological tissues absorption of light is negligible compared to scattering. The symbol * denotes the complex conjugate operation. $h_a(r, z)$ and $h_b(r, z)$ are the 3D amplitude point spread functions (APSF) of the outer annular and central circular objective apertures,

respectively. According to the scalar diffraction theory and the paraxial approximation, these are defined by:

$$h_{a,b}(r, z) = \int_0^1 P_{a,b}(\rho) J_0(v\rho) \exp(-iu\rho/2) \rho d\rho. \quad (6.24)$$

Here we employ an equal-area annular aperture where $\varepsilon = \sqrt{2}/2$. These expressions also apply for other non-overlapping geometries for the pupils P_a and P_b .

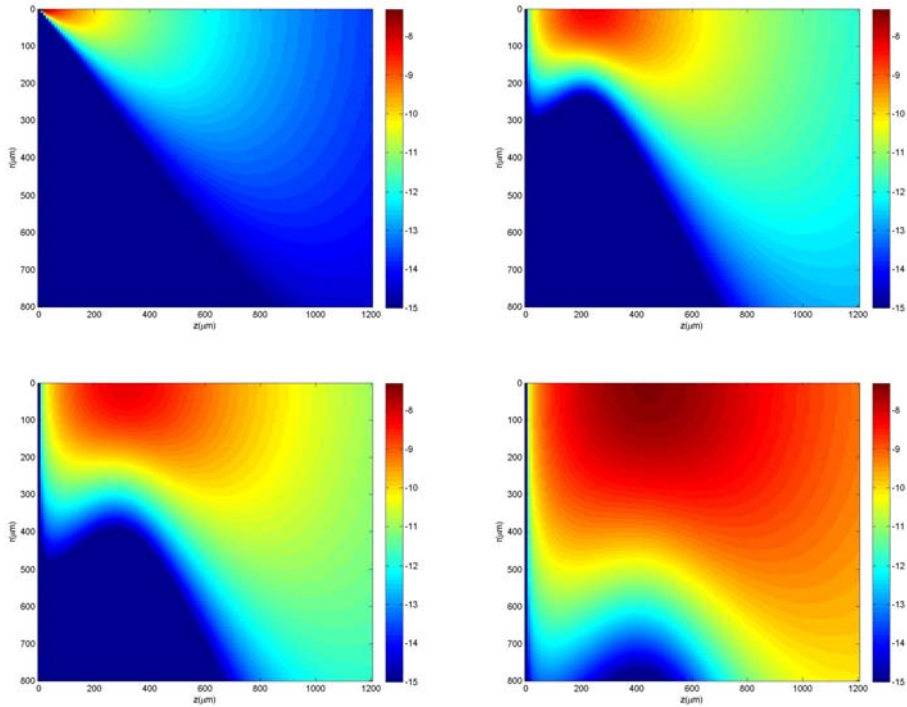


Figure 6.6. The scattering light with various focus depth at $0\mu\text{m}$, $400\mu\text{m}$, $600\mu\text{m}$, and $1000\mu\text{m}$, respectively. $l_s = 200\mu\text{m}$, $n = 1.33$, $NA = 0.566$, and

$$\lambda = 0.9\mu\text{m}$$

Figure 6.6 illustrates the scattering light I_{SS} with various focus depth at $0\mu\text{m}$, $400\mu\text{m}$, $600\mu\text{m}$, and $1000\mu\text{m}$, respectively. It can be noticed that the out-of-focus fluorescence generated by scattered light can extend to a depth

of several l_s and can be the overall dominating contribution. The peak of the scattered light does not converge on the focal point, but lies in some point between the surface and the focal point. As the focal depth increases, the depth where the peak value lies at increases.

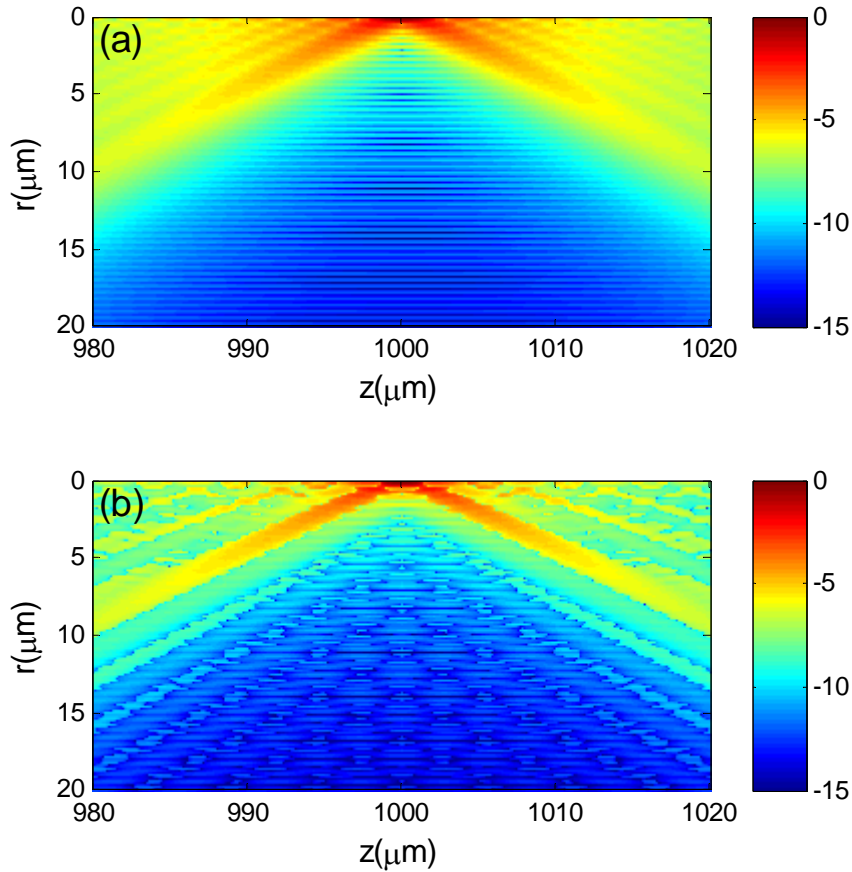


Figure 6.7. The ballistic light (log value) focused at $5l_s$ with $l_s = 200\mu\text{m}$, $n = 1.33$, $NA = 0.556$, and $\lambda = 0.9\mu\text{m}$ in (a) 2PM, and (b) 2PFMM.

Figure 6.7 illustrates the ballistic light of 2PFMM compared with conventional 2P fluorescence microscopy focused at $5l_s$, where $l_s = 200\mu\text{m}$, $n = 1.33$, and $\lambda = 0.9\mu\text{m}$, which are typical conditions encountered in two-photon imaging of brain tissue. It is noticed that the ballistic excitation light in 2PFMM is highly concentrated around the focal point and decays

rapidly outside the focal volume. This indicates that at the same focal depth, 2PFMM can achieve a better sectioning ability, which is a desirable behavior for high resolution imaging. It can be also noticed that there are some oscillating regions in 2PFMM compared with conventional 2P fluorescence microscopy, which are due to the negative values appeared in the in-phase signal [10].

Figure 6.8 illustrate the variations of the total excitation light distribution as the focal point moves deep into the sample for 2PM and 2PFMM, respectively. The out-of-focus fluorescence (background) in the two-photon excitation technique mainly comes from the scattered light, which extend to a depth of several l_s , and ballistic light near the surface and near the focal volume. For 2PM, at large imaging depth, fluorescence generated near the surface significantly increases, and scattered light become the overall dominant contribution. Thus, the imaging depth is fundamentally limited by the onset of out-of-focus fluorescence generation near the surface of the sample. However, the scattered contributions are filtered due to the demodulation mechanism in 2PFMM. Therefore, the near-surface fluorescence is not the limiting factor for 2PFMM, in which the imaging performance is limited by the out-of-focus fluorescence near the focal volume mainly. This property implies the potential for deep penetration depth with 2PFMM. Note that 2PFMM exhibits fringes around the focal point due to the

diffraction pattern of the ballistic intensity point spread function, which confirms that scattered light is largely suppressed.

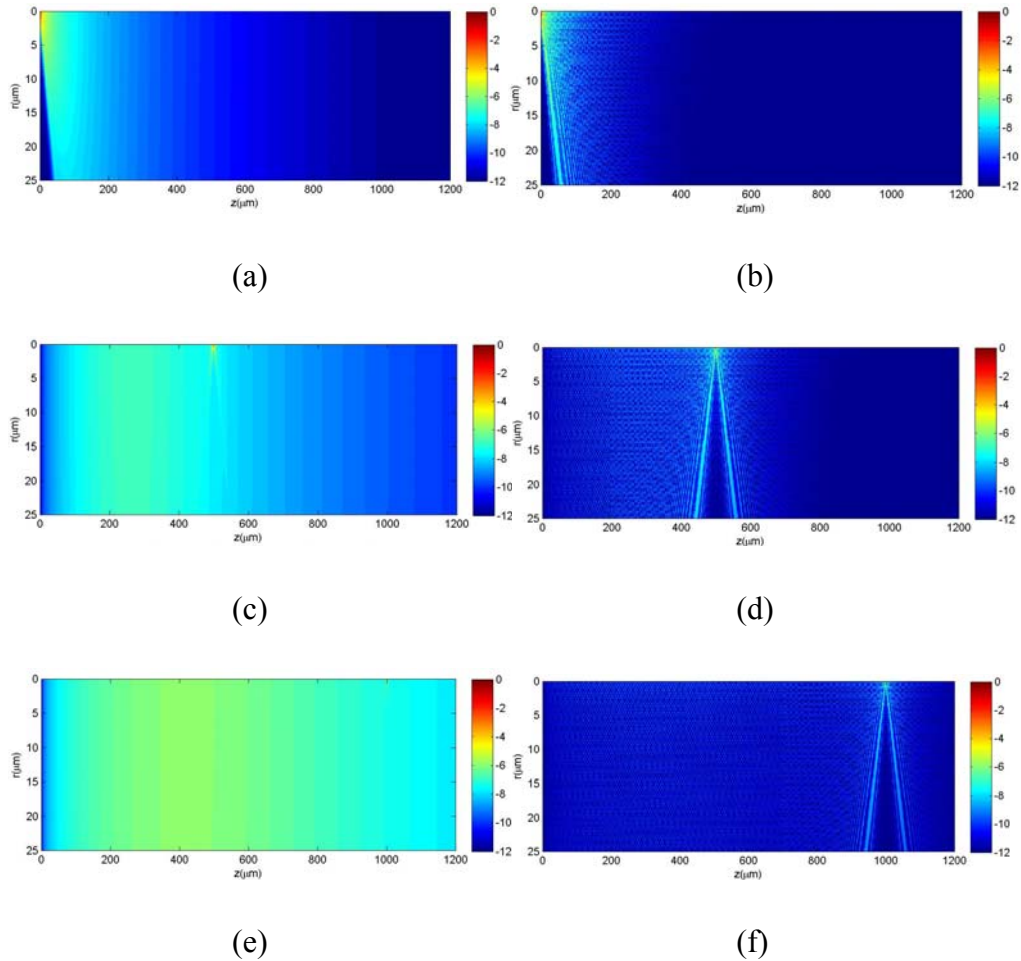


Figure 6.8. The variations of the total excitation (log value) with different focal depths in: (a) focused at $0\mu\text{m}$ in 2PM, and (b) focused at $0\mu\text{m}$ in 2PFMM, (c) focused at $500\mu\text{m}$ in 2PM, and (d) focused at $500\mu\text{m}$ in 2PFMM, (e) focused at $1000\mu\text{m}$ in 2PM, and (f) focused at $1000\mu\text{m}$ in 2PFMM.

$$l_s = 200\mu\text{m}, n = 1.33, NA = 0.566, \text{ and } \lambda = 0.9\mu\text{m}.$$

To reveal the background contribution of each depth slice, we introduce a simple scattering model, based on integrated intensity. If the intensity image of a point is $I(r, z)$, then the contribution to the background in the focal plane from a distribution of particles an axial distance z away is:

$$I_{\text{int}}(z) = \int_0^{\infty} I(r, z) r dr. \quad (6.25)$$

The integrated intensity can also be used to describe the background from an infinitely thin autofluorescent sheet.

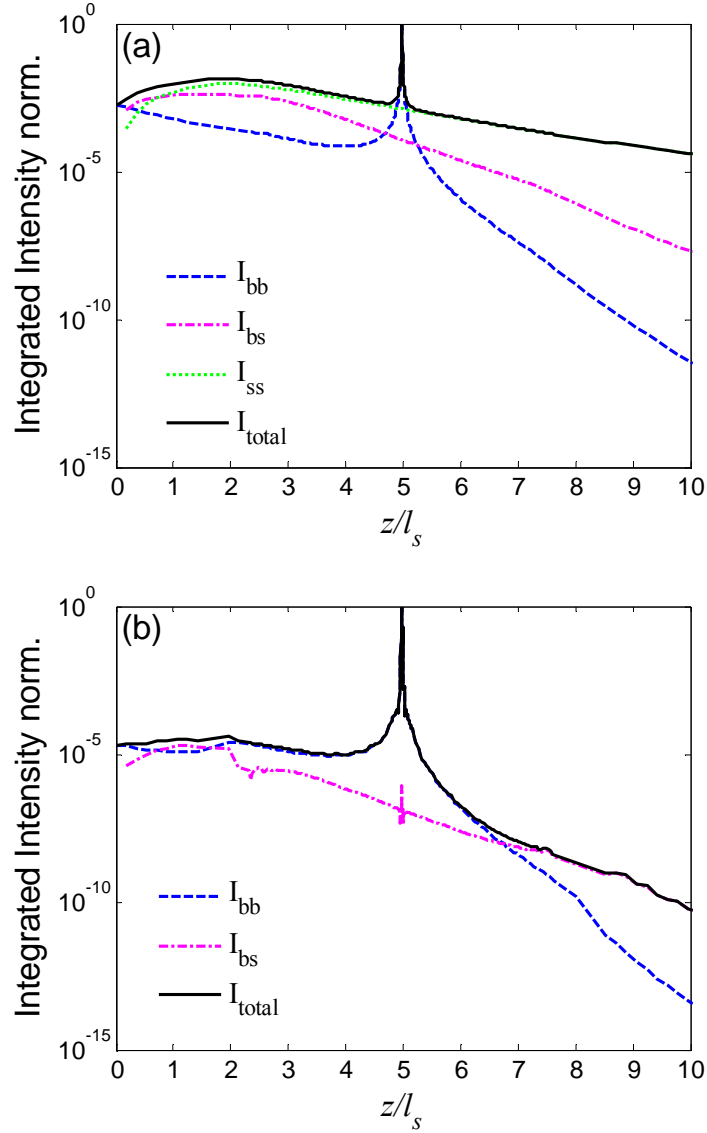


Figure 6.9. The comparison of the integrated intensity of I_{bb} , I_{bs} , I_{ss} , and I_{total} in (a) 2PM, and (b) 2PFMM. $z_0 = 1000\mu\text{m}$, $l_s = 200\mu\text{m}$, $n = 1.33$, $NA = 0.566$,

$$g = 0.9, \text{ and } \lambda = 0.9\mu\text{m}.$$

The comparison of the integrated intensity of I_{bb} , I_{bs} , I_{ss} , and I_{total} in 2PFMM and 2PM is shown in Fig. 6.9. Near the surface, background

fluorescence is mainly due to ballistic light in 2PFMM, which dominates down to a depth of approximately one scattering-mean-free-path length. However, near-surface background is dominated by the out-of-focus fluorescence generated by scattered light in 2PM. In addition, the out-of-focus ballistic fluorescence is much smaller in 2PFMM. As a result, given the same excitation intensity the total near-surface background is 20dB smaller in 2PFMM than in 2PM when focused at $5l_s$. 2PFMM results in reduced out-of-focus ballistic light and a largely suppressed out-of-focus scattered light, which imply the potential to achieve a greater imaging depth.

Assuming a detection efficiency that is independent of the fluorescence origin, the signal to background ratio (SBR) with wide field-detection can be expressed by:

$$SBR = \frac{\int_{V_0} I_{bb}(r, z) dV}{\int_0^\infty I_{total}(r, z) dV - \int_{V_0} I_{bb}(r, z) dV}, \quad (6.26)$$

where V_0 is the small focal volume, whose radius equals to the beam waist of the Gaussian beam. Figure 6.10 shows the SBR of 2PFMM and 2P fluorescence microscopy with different anisotropy, as a function of focus depth z_0 (Fig. 6.10a) and as a function of anisotropic factor g (Fig. 6.10b), respectively. It can be noticed from Fig. 6.10a that when the focal depth is smaller than $3l_s$, the SBR of both 2PFMM and conventional 2P fluorescence microscopy is maintained. This is understandable, because the background

mainly comes from the out-of-focus ballistic light near the focal volume. However, the SBR is approximately 7dB higher in 2PFMM than in 2PM. This indicates that 2PFMM contains approximately 7dB less out-of-focus background, and thus exhibits a much better resolution for a focal depth smaller than $3l_s$. When the focal depth is larger than $3l_s$ but smaller than $4l_s$, the SBR in conventional 2P fluorescence microscopy begins to decay, because the near-surface background fluorescence begins to dominate. When the focal depth is larger than $4l_s$, the SBR in conventional 2P fluorescence microscopy decays exponentially, depending on the anisotropy factor g . This is because the out-of-focus fluorescence generated by scattered light becomes dominating when two-photon excitation is focused at large focal depth. In contrast, the SBR in 2PFMM keeps almost constant until the focal depth is larger than $7l_s$, where the background fluorescence mainly comes from the out-of-focus fluorescence generation near the surface of the sample. This indicates that the scattered fluorescence plays a less important role in the background in 2PFMM than in 2PM. Thus the SBR in 2PFMM is significantly improved. For example, when the focal depth z_0 equals to $6l_s$, the SBR is enhanced by 23dB with 2PFMM. If the imaging depth limit is regarded as the depth where the signal (perifocal fluorescence) to background (out-of-focus fluorescence) ratio (SBR) of 2PM reduces to 1/10 of the surface, the imaging depth of 2PFMM can be increased by a factor of 2 when $g = 0.01$, and 3 when $g = 0.98$.

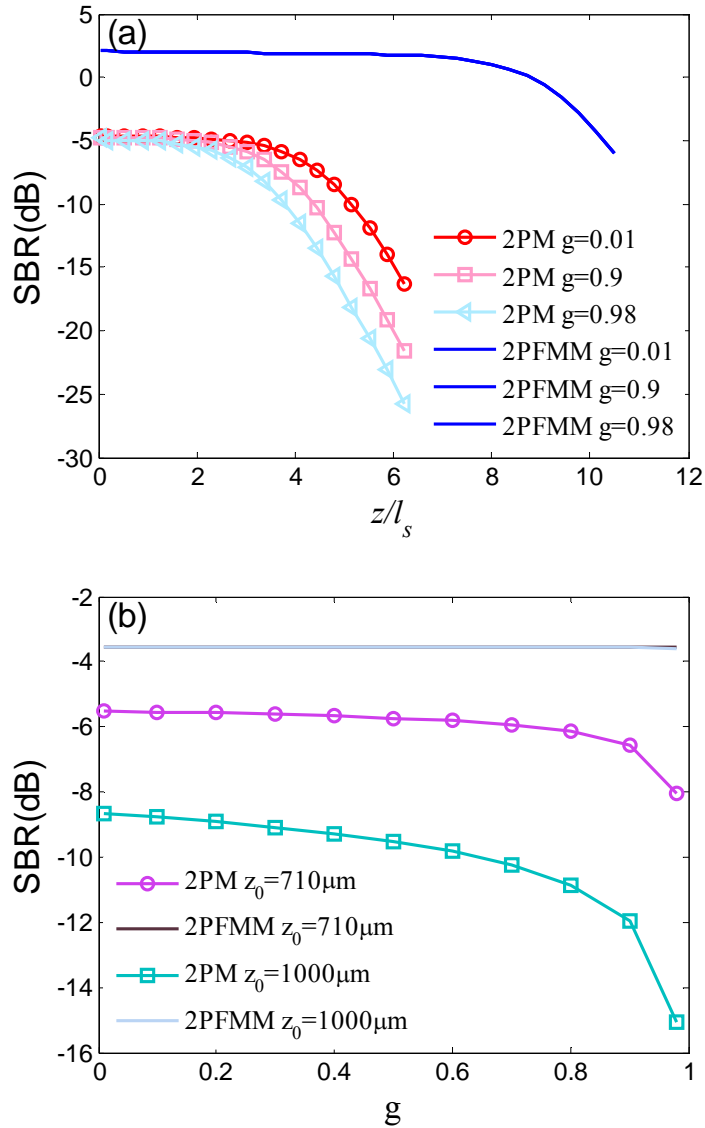


Figure 6.10. The signal to background ratio (SBR) in 2PFMM and 2PM: (a) as a function of focus depth z and (b) as a function of anisotropic factor g .

$$l_s = 200\mu\text{m}, n = 1.33, NA = 0.566, \text{ and } \lambda = 0.9\mu\text{m}.$$

Figure 6.10b provides the SBR variations as a function of anisotropy factor g . It can be seen that the SBR decays as g increases in conventional 2P fluorescence microscopy, which confirms the results that with a decreasing anisotropy factor, the ratio of perifocal and out-of-focus fluorescence increases, as reported by Theer *et al.* [21]. However, the SBR is maintained in

2PFMM. This suggests that the out-of-focus fluorescence generated by scattered light, which is crucial factor in conventional 2P fluorescence microscopy, plays a minor role in the total background fluorescence in 2PFMM. This property implies a potential for 2PFMM in the imaging of thick tissue in biology and medicine.

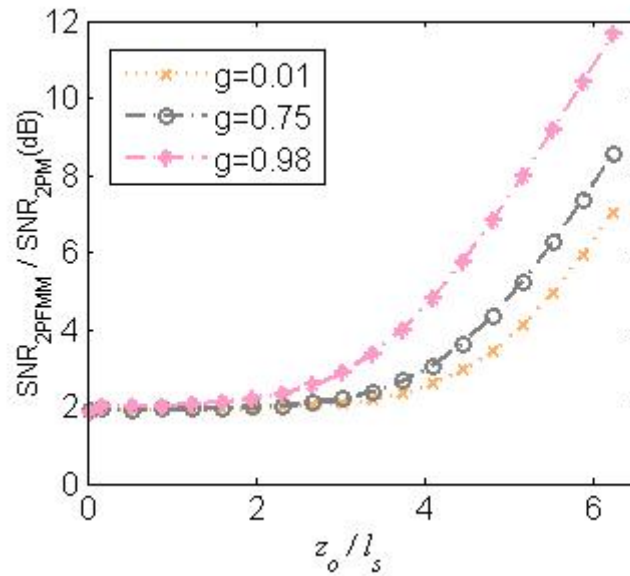


Figure 6.11 The ratio of SNR in 2PFMM to SNR 2PM as a function of focus depth z_o . $l_s = 200\mu m$, $n = 1.33$, $NA = 0.56$, and $\lambda = 0.9\mu m$.

The signal-to-noise ratio in the photon-counting mode can be written as

[24]

$$SNR = \frac{S}{\sqrt{S+B}}, \quad (6.27)$$

Both S and B are proportional to the number of photons collected by unit time by a given microscope port. If a high speed modulator (eg.10MHz) is used, the pixel dwell-time will be very short, thus we neglect the dark count as

compared to the background noise. Figure 6.11 illustrates the ratio of the SNR in 2PFMM to SNR in 2PM as a function of the focal depth z_0 . It can be noticed that the superior of SNR in 2PFMM over 2PM is 2dB even when focused at the surface. As the focus depth increases, the noise rejection of 2PFMM is further improved, indicating a deeper penetration depth with 2PFMM technique. For example, when focus at $8l_s$, the SNR of 2PFMM is improved by 18dB. The enhanced noise rejection capability of 2PFMM is due to the fact that the use of lock-in amplifier rejects the noise components that do not fall on the modulation frequency.

In one photon focal modulation microscopy, as the detector pinhole size increases, the signal level first increases, then decreases, leading to a maximum value [11, 14, 25]. However, for 2PFMM, the signal level increases monotonically as the detector pinhole size increases, showing in Figure 6.12.

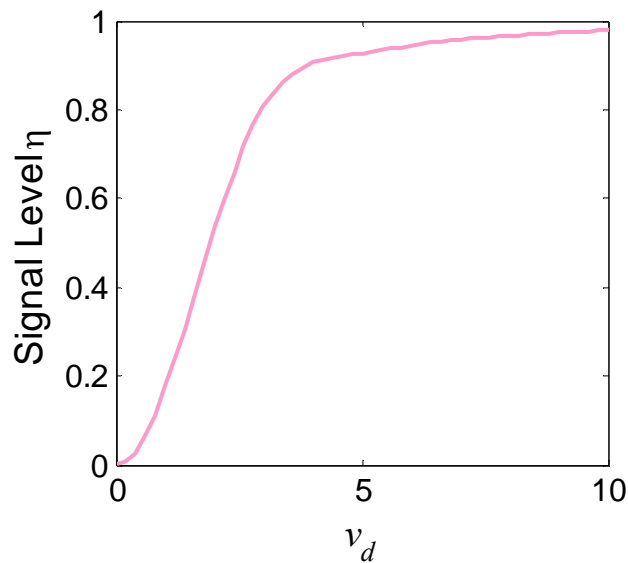


Figure 6.12 Signal level for 2PFMM with a finite-sized detector pinhole.

6.4 Conclusion

In summary, we have demonstrated theoretically a focal modulation imaging technique to reject out-of-focus background in two-photon imaging of thick tissue. The theoretical comparison of signal to background ratio between 2PFMM and 2PM reveals that using 2PFMM the imaging penetration depth of 2PM can be extended by a factor of up to 3. An added benefit of our technique is that it can improve the spatial resolution due to the fact that the excitation light is more concentrated around the focal point and decays more quickly outside the focal volume. Moreover, using modulation and demodulation techniques can further enhance the noise rejection by reducing noise components that do not fall near the modulation frequency.

References

1. V. E. Centonze and J. G. White, "Multiphoton excitation provides optical sections from deeper within scattering specimens than confocal imaging," *Biophys J* **75**, 2015-2024 (1998).
2. W. Denk, J. H. Strickler, and W. W. Webb, "Two-photon laser scanning fluorescence microscopy," *Science* **248**(1990).
3. B. R. Masters, P. T. C. So, and E. Gratton, "Multiphoton excitation fluorescence microscopy and spectroscopy of in vivo human skin," *Biophys J* **72**, 2405-2412 (1997).
4. P. T. C. So, H. Kim, and I. E. Kochevar, "Two-photon deep tissue ex vivo imaging of mouse dermal and subcutaneous structures," *Opt Express* **3**, 339-350 (1998).
5. J. P. Ying, F. Liu, and R. R. Alfano, "Spatial distribution of two-photon-excited fluorescence in scattering media (vol 38, pg 224, 1999)," *Appl Optics* **38**, 2151-2151 (1999).
6. P. Theer, M. T. Hasan, and W. Denk, "Two-photon imaging to a depth of 1000 μm in living brains by use of a Ti:Al₂O₃ regenerative amplifier," *Opt. Lett.* **28**, 1022-1024 (2003).
7. M. Balu, T. Baldacchini, J. Carter, T. B. Krasieva, R. Zadoyan, and B. J. Tromberg, "Effect of excitation wavelength on penetration depth in nonlinear optical microscopy of turbid media," *J Biomed Opt* **14**, - (2009).
8. A. Leray and J. Mertz, "Rejection of two-photon fluorescence background in thick tissue by differential aberration imaging," *Opt Express* **14**, 10565-10573 (2006).
9. N. G. Chen, C. H. Wong, and C. J. R. Sheppard, "Focal modulation microscopy," *Opt. Express* **16**, 18764-18769 (2008).
10. W. Gong, K. Si, and C. J. R. Sheppard, "Improved spatial resolution in fluorescence focal modulation microscopy," *Opt. Lett.* **34**, 3508-3510 (2009).
11. K. Si, W. Gong, and C. J. R. Sheppard, "Edge enhancement for in-phase focal modulation microscope," *App. Opt.* **48**, 6290-6295 (2009).
12. S. P. Chong, C. H. Wong, C. J. R. Sheppard, and N. Chen, "Focal modulation microscopy: a theoretical study," *Opt. Lett.* **35**, 1804-1806 (2010).
13. M. Gu, *Principles of Three-Dimensional Imaging in Confocal Microscopes* (World Scientific, 1996).
14. W. Gong, K. Si, N. Chen, and C. J. R. Sheppard, "Focal modulation microscopy with annular apertures: A numerical study," *J. Biophoton.* **DOI**, 10.1002/jbio.200900110 (2009).

15. M. Gu and C. J. R. Sheppard, "Comparison of 3-Dimensional Imaging Properties between 2-Photon and Single-Photon Fluorescence Microscopy," *J Microsc-Oxford* **177**, 128-137 (1995).
16. H. C. Vandehulst and G. W. Kattawar, "Exact Spread Function for a Pulsed Collimated Beam in a Medium with Small-Angle Scattering," *Appl Optics* **33**, 5820-5829 (1994).
17. S. Kumar, K. Mitra, and Y. Yamada, "Hyperbolic damped-wave models for transient light-pulse propagation in scattering media," *Appl Optics* **35**, 3372-3378 (1996).
18. C. M. Blanca and C. Saloma, "Efficient analysis of temporal broadening of a pulsed focused Gaussian beam in scattering media," *Appl Optics* **38**, 5433-5437 (1999).
19. R. F. Lutomirski, A. P. Ciervo, and G. J. Hall, "Moments of Multiple-Scattering," *Appl Optics* **34**, 7125-7136 (1995).
20. J. W. McLean, J. D. Freeman, and R. E. Walker, "Beam spread function with time dispersion," *Appl Optics* **37**, 4701-4711 (1998).
21. P. Theer and W. Denk, "On the fundamental imaging-depth limit in two-photon microscopy," *J Opt Soc Am A* **23**, 3139-3149 (2006).
22. V. I. Haltrin, "One-parameter two-term Henyey-Greenstein phase function for light scattering in seawater," *Appl Optics* **41**, 1022-1028 (2002).
23. P. Theer, "On the fundamental imaging-depth limit in two-photon microscopy," Doctoral dissertation (University of Heidelberg, 2004).
24. A. K. Dunn, V. P. Wallace, M. Coleno, M. W. Berns, and B. J. Tromberg, "Influence of optical properties on two-photon fluorescence imaging in turbid samples," *Appl Optics* **39**, 1194-1201 (2000).
25. K. Si, W. Gong, N. Chen, and C. J. R. Sheppard, "Enhanced background rejection in thick tissue using focal modulation microscopy with quadrant apertures," *Optics Comm.* **doi:**, 10.1016/j.optcom.2010.1011.1007 (2010).

Chapter 7 Polarization effects in microscopy

7.1 Introduction

So far in this thesis we have used scalar paraxial theory to calculate imaging properties of microscope systems, but in practice microscopes usually use high numerical aperture objectives where the paraxial theory is not really valid. Polarization effects are known to be an important consequence of high numerical apertures. Polarization will have important effects on the performance of FMM, which can be seen very simply from the symmetry of the pupils. However, here we consider 4Pi microscopy, where the role of polarization is even more important.

The 4Pi microscope is well known as a way of substantially improving the axial resolution in confocal or two-photon microscopy [1-3]. The illumination is arranged to approximate a complete sphere of incoming radiation [4]. The three-dimensional (3D) imaging properties of 4Pi microscopy, based on a scalar theory, have been described in a few papers [5-6, 7], but as 4Pi microscopy uses high numerical aperture objectives, vectorial polarization effects are important. Although Refs. 1-3 gave plots of the point spread function for the vectorial case with plane-polarized light, comparison with conventional focusing was not discussed. Recently, our group has presented parameters that can be applied to focusing in optical systems with various

different polarization properties [8-10]. These three papers discussed the cases of plane polarized or radially polarized illumination, and mixtures of electric and magnetic dipole or transverse electric and transverse magnetic fields. All of these can also be applied to the 4Pi case to investigate the effects of polarization in different cases. Tight 3D focusing of light also has applications in other areas, including laser trapping and cooling [11].

7.2 Symmetry considerations

The field distributions on the surface of the reference sphere for focused ingoing radiation for various different illumination polarizations are illustrated in Figure 7.1.

In order to produce the most concentrated electric field in 3D at the focal point, the polarization must match up with that of an electric dipole. For the complete spherical case, this dipole can be oriented either in a transverse direction, corresponding to an electric dipole field (ED), or in the longitudinal direction, corresponding to radially polarized illumination of the lens (TM₀, or R). These two limiting cases are by symmetry completely equivalent. But if we implement these arrangements using a lens of limited numerical aperture, the angular spectrum components that are missing are different in the two cases. The complete magnetic dipole field concentrates all the energy into the magnetic field at the focus, giving a zero in electric energy density, so this

arrangement is undesirable for 4Pi imaging. The mixed dipole polarization (Mixed), which results from the focusing of plane polarized light, is a reasonably good approximation to the transverse electric dipole case for one hemisphere, but for the other hemisphere the match becomes worse the closer to the optical axis. Thus for plane polarized illumination, the two lenses in a 4Pi system should each be individually illuminated with plane polarized radiation. This is then an approximation to the electric dipole field for the correct relative phase of the two components. If the two components are in antiphase the polarization approximates to the magnetic dipole field. Finally, the transverse electric distribution TE₁ can also be used. Note that this is fundamentally different from the TE₀, azimuthally polarized case, but for simplicity in the following sections we refer to it as simply TE.

Figure 7.2 shows the polarization necessary in the front focal plane of the lens to produce these different polarizations on the reference sphere. Note that instead of illuminating with plane polarized light we can use circularly polarized light, which corresponds to vertical and horizontal polarizations added in quadrature. In this case the focal spot is circularly symmetrical. A similar approach can be applied for the other polarizations: the equivalent form for TE₁ is azimuthal polarization with a phase singularity (vortex) of charge unity. ED becomes an elliptical polarization, with ellipticity increasing with angle subtended at the axis, with a phase singularity superposed.

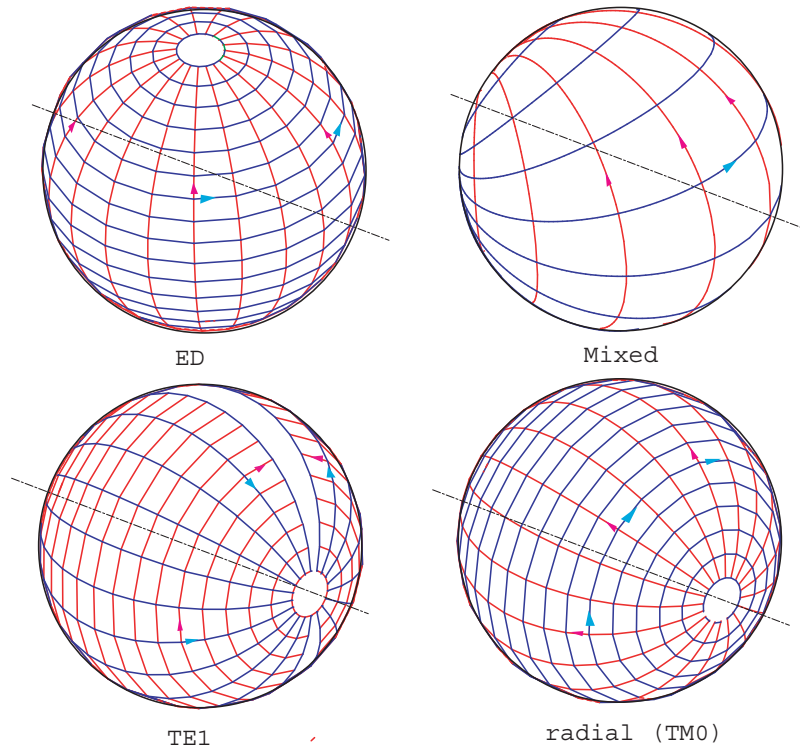


Figure 7.1. The electric and magnetic fields on the surface of the reference sphere for ingoing radiation satisfying various different polarization conditions. Electric field is shown in red and magnetic field in blue.

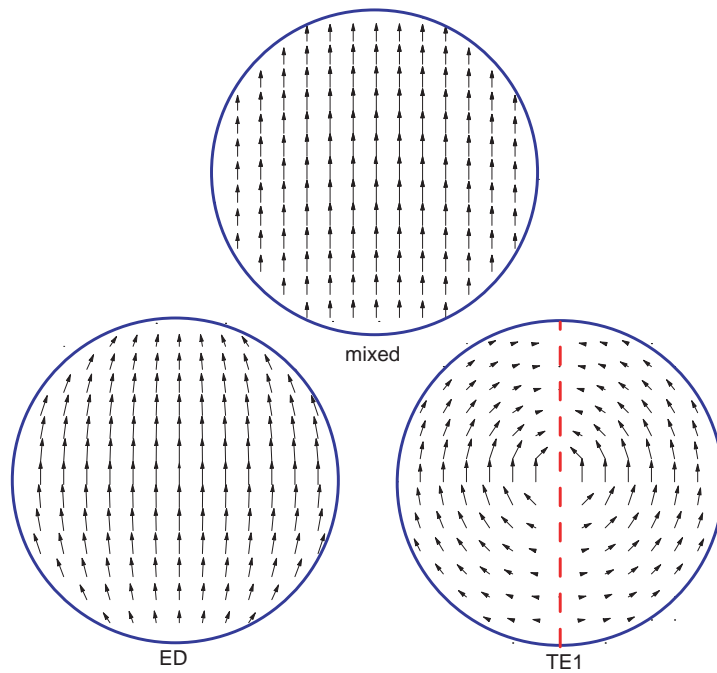


Figure 7.2. The electric field in the front focal plane of each lens for different polarization distributions. The radius of the circles corresponds to $\sin \alpha = 1$. The electric field is zero at the dashed line.

7.3 Illumination using two counter-propagating beams

We consider five important cases for the illumination. The first is the usual experimental arrangement of illuminating two aplanatic lenses with two counter-propagating beams of plane polarized light (A). The second case is also for plane polarized light, but with the apodization modified to optimise intensity at the focus (Mixed) [12]. We call this condition the mixed-dipole field, as it corresponds to the fields of a transverse electric dipole and a transverse magnetic dipole oriented at right angles to each other at the focal point. The third case we consider is that of electric dipole polarization, where the polarization is modified to increase the electric energy density at the focus (ED) [13-14]. In addition, another interesting case that has been considered is illumination with transverse electric polarized light (TE) [10]. Finally, we consider illumination with radially polarized light (R) [15-20]. The electric energy density at the focus for a given focused power (F) for all these cases has been presented previously [21]. F is defined so that it is unity for a complete electric dipole field.

Figure 7.3 compares the behaviour for all five 4π cases. The electric dipole field ED exhibits the best performance. The mixed dipole field (Mixed) is slightly better than the aplanatic case A. The radial case R is only better than the aplanatic case if the numerical aperture is very high (above $0.97NA$ in air, corresponding to a semi-angular aperture of the system $\alpha > 83^\circ$). The TE case

gives lower values of F than the other cases for high numerical apertures. For the limiting case of $\alpha = 90^\circ$, the values of F are $64/75$, $7/8$, 1 , $3/4$, 1 for A, Mixed, ED, TE, R, respectively.

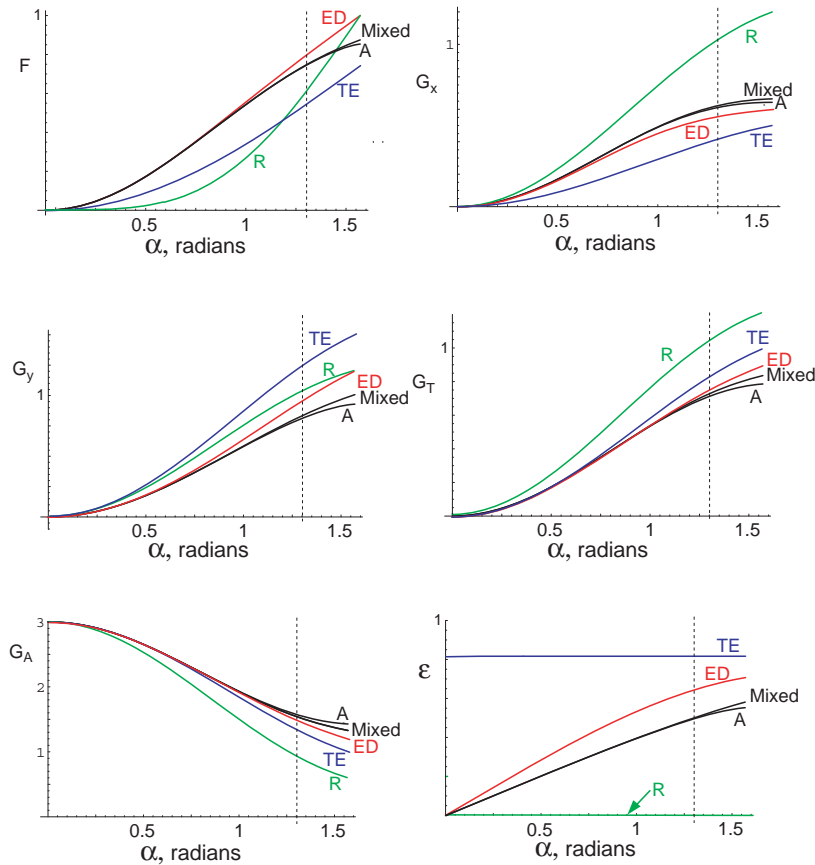


Figure 7.3. The variation in the parameters F , G_x , G_y , G_T , G_A , and ϵ with angular semi-aperture of each objective lens in a 4π system. The dashed line corresponds to a numerical aperture of 1.46 in oil. A is aplanatic, Mixed is mixed dipole, ED is electric dipole, TE is transverse electric TE1, and R is radial polarization.

The first two, plane polarized, cases can be treated based on Ref.[8]. But they are also special cases of Ref.[10], on which we base our treatment here. The electric field at the point with cylindrical coordinates ρ, ϕ, z in the focal region of a single lens can be written in terms of electric and magnetic dipole

components [14, 22]

$$\begin{aligned}
 E_x &= -ikf \left[(I_{0p} + I_{0m}) + (I_{2p} + I_{2m}) \cos 2\phi \right], \\
 E_y &= -ikf (I_{2p} + I_{2m}) \sin 2\phi, \\
 E_z &= -2kf (I_{1p} + I_{1m}) \cos \phi,
 \end{aligned} \tag{7.1}$$

where

$$\begin{aligned}
 I_{0p} &= \int_{-1}^1 Q_p(c) (1+c^2) J_0(k\rho\sqrt{1-c^2}) \exp(ikzc) dc, \\
 I_{1p} &= \int_{-1}^1 Q_p(c) c\sqrt{1-c^2} J_1(k\rho\sqrt{1-c^2}) \exp(ikzc) dc, \\
 I_{2p} &= \int_{-1}^1 Q_p(c) (1-c^2) J_2(k\rho\sqrt{1-c^2}) \exp(ikzc) dc, \\
 I_{0m} &= \int_{-1}^1 Q_m(c) 2c J_0(k\rho\sqrt{1-c^2}) \exp(ikzc) dc, \\
 I_{1m} &= \int_{-1}^1 Q_m(c) \sqrt{1-c^2} J_1(k\rho\sqrt{1-c^2}) \exp(ikzc) dc, \\
 I_{2m} &= 0.
 \end{aligned} \tag{7.2}$$

The pupil function is expressed in terms of its electric and magnetic dipole field components, $Q_{p,m}(c)$, expressed as functions of $c = \cos \theta$, where θ is the angle between the direction of propagation of a plane wave component and the optical axis. The pupil functions are defined so that $Q_p(c) = Q_m(c) = 1$

corresponds to a mixed dipole field (Mixed) [12], which is the field of an electric dipole oriented along the x axis and a magnetic dipole oriented along the y axis. The electric and magnetic field magnitudes are axially symmetric and vary as $(1+\cos\theta)/2$. For any plane-polarized illumination, the electric and magnetic dipole components are equal. For an aplanatic system (A) with no pupil filter we have $Q_p(c)=Q_m(c)=2c^{1/2}/(1+c)$. Note that the pupil function is defined differently from those in some earlier treatments [8]. For the electric dipole field (ED), the magnetic dipole component is zero: $Q_p(c)=1, Q_m(c)=0$ [13-14].

These formulae can be applied directly to the case of 4Pi imaging. Then we have for an aplanatic system (A)

$$\begin{aligned}
 Q_p(c) &= \begin{cases} \frac{2c^{1/2}}{1+c}, & \cos\alpha < c < 1, \\ \frac{2c^{1/2}}{1+c}, & -\cos\alpha > c > -1, \end{cases} \\
 Q_m(c) &= \begin{cases} \frac{2c^{1/2}}{1+c}, & \cos\alpha < c < 1, \\ -\frac{2c^{1/2}}{1+c}, & -\cos\alpha > c > -1. \end{cases}
 \end{aligned} \tag{7.3}$$

and zero otherwise. This corresponds to the system being set up to give a maximum in electric field, but a zero in magnetic field at the focus. We can note that the axial resolution improvement of 4Pi microscopy can be explained by the fact that the magnetic component of the pupil exhibits odd symmetry, so that the magnetic dipole component cancels at the focal point. So the

electric field approximates to that of an electric dipole. Alternatively, if the system is adjusted so that the two beams are in antiphase, the electric dipole component cancels, and the field approximates to that of a magnetic dipole. In both cases the polarization is different from that produced using a deep paraboloid mirror with linearly polarized illumination [12]. The field in the focal region can be calculated directly from Eqs. 1-3. Equivalently, we can replace the complex exponential by a cosine for the electric dipole and i times a sine for the magnetic dipole components, and take the pupils as zero outside of the range $\cos \alpha < c < 1$.

For the case of electric dipole polarization (ED), we have

$$Q_p(c) = \begin{cases} 1, & \cos \alpha < c < 1, \\ 1, & -\cos \alpha > c > -1, \end{cases} \quad (7.4)$$

$$Q_m(c) = 0.$$

and zero elsewhere. We see that A and Mixed can be considered as approximations to ED, in all cases the electric field of the magnetic dipole component cancelling at the focal point. Previously we defined performance parameters G_x, G_y, G_A that describe the parabolic widths of the central lobe of the focal spot in the x , y , and axial directions:

$$W = W_0 \left[1 - G_x \frac{(kx)^2}{3} - G_y \frac{(ky)^2}{3} - G_A \frac{(kz)^2}{3} \right] \quad (7.5)$$

the widths of the central lobe of the focused spot in different directions being proportional to $1/G^{1/2}$. The parameters are normalized to unity for a full spherical scalar wave. We can also introduce the transverse gain averaged over all transverse directions

$$G_T = (G_x + G_y)/2, \quad (7.6)$$

and the polar gain (averaged over all directions in three dimensions)

$$G_P = (G_x + G_y + G_A)/3 = (2G_T + G_A)/3. \quad (7.7)$$

Note that the parameter G_T also applies for the transverse gain for illumination with circularly polarized rather than plane-polarized light. In this case the focal spot is circularly symmetrical. The eccentricity of the focal spot is $\varepsilon = (1 - G_x/G_y)^{1/2}$. The performance parameters, in terms of the moments of the pupils [10]

$$q_{pn} = \int_{-1}^1 Q_p(c) c^n dc, \quad (7.8)$$

$$q_{mn} = \int_{-1}^1 Q_m(c) c^n dc,$$

for the 4Pi case reduce to

$$G_x = \frac{3}{4} \frac{q_{p0} + 2q_{p2} - 3q_{p4} + 4q_{m1} - 4q_{m3}}{q_{p0} + q_{p2} + 2q_{m1}},$$

$$G_y = \frac{3}{4} \frac{3q_{p0} - 2q_{p2} - q_{p4} + 4q_{m1} - 4q_{m3}}{q_{p0} + q_{p2} + 2q_{m1}},$$

$$G_T = \frac{3}{2} \frac{q_{p0} - q_{p4} + 2q_{m1} - 2q_{m3}}{q_{p0} + q_{p2} + 2q_{m1}}, \quad (7.9)$$

$$G_A = 3 \frac{q_{p2} + q_{p4} + 2q_{m3}}{q_{p0} + q_{p2} + 2q_{m1}},$$

$$G_p = 1.$$

In general, for a system adjusted to give a maximum in electric field at the focus, we have the symmetry conditions $q_{pn} = 0, n \text{ odd}$ and $q_{mn} = 0, n \text{ even}$. Note that the symmetry has resulted in the polar gain being unity, independent of the aperture. In fact all the case considered here have this property. Thus transverse and axial gains are simply related, so that if one increases the other decreases.

For the case of plane polarized illumination, A and Mixed, $Q_p = Q_m$, so $q_{pn} = q_{mn} = q_n$, say, and

$$\begin{aligned}
G_x &= \frac{3}{4} \frac{q_0 + 4q_1 + 2q_2 - 4q_3 - 3q_4}{q_0 + 2q_1 + q_2}, \\
G_y &= \frac{3}{4} \frac{3q_0 + 4q_1 - 2q_2 - 4q_3 - q_4}{q_0 + 2q_1 + q_2}, \\
G_T &= \frac{3}{2} \frac{q_0 + 2q_1 - 2q_3 - q_4}{q_0 + 2q_1 + q_2}, \\
G_A &= 3 \frac{q_2 + 2q_3 + q_4}{q_0 + 2q_1 + q_2}, \\
G_P &= 1.
\end{aligned} \tag{7.10}$$

For the case of the electric dipole polarization (ED), we have $q_{mn} = 0$, so we can write $q_{pn} = q_n$, giving

$$\begin{aligned}
G_x &= \frac{3}{4} \frac{q_0 + 2q_2 - 3q_4}{q_0 + q_2}, \\
G_y &= \frac{3}{4} \frac{3q_0 - 2q_2 - q_4}{q_0 + q_2}, \\
G_T &= \frac{3}{2} \frac{q_0 - q_4}{q_0 + q_2}, \\
G_A &= 3 \frac{q_2 + q_4}{q_0 + q_2}, \\
G_P &= 1.
\end{aligned} \tag{7.11}$$

The parameters can alternatively be calculated by expanding the pupil into TE and TM components, $Q_{TE,TM}(c)$, as we have described in a previous paper

[10]. In general for the 4Pi case, $q_{TE_n} = 0, n \text{ odd}$ and $q_{TM_n} = 0, n \text{ even}$. Then

$$\begin{aligned}
 G_x &= \frac{3}{4} \frac{q_{TE0} - q_{TE2} + 3q_{TM1} - 3q_{TM3}}{q_{TE0} + q_{TM1}}, \\
 G_y &= \frac{3}{4} \frac{3q_{TE0} - 3q_{TE2} + q_{TM1} - q_{TM3}}{q_{TE0} + q_{TM1}}, \\
 G_T &= \frac{3}{4} \frac{q_{TE0} - q_{TE2} + q_{TM1} - q_{TM3}}{q_{TE0} + q_{TM1}}, \\
 G_A &= 3 \frac{q_{TE2} + q_{TM3}}{q_{TE0} + q_{TM1}}, \\
 G_P &= 1.
 \end{aligned} \tag{7.12}$$

For an aplanatic system A we then have $Q_{TE}(c) = Q_{TM}(c) = c^{1/2}$ when nonzero.

If $Q_{TE}(c) = Q_{TM}(c) = 1 + c$ when nonzero, the system reduces to Mixed.

For the electric dipole case, $q_{TM_n} = q_{TE(n+1)} = q_{n+1}$, and

$$\begin{aligned}
 G_x &= \frac{3}{4} \frac{(q_0 + q_2)(q_0 + 2q_2 - 3q_4) - 4(q_1 - q_3)^2}{(q_0 + q_2)^2}, \\
 G_y &= \frac{3}{4} \frac{3q_0 - 2q_2 - q_4}{q_0 + q_2}, \\
 G_T &= \frac{3}{4} \frac{(q_0 + q_2)(q_0 - q_4) - (q_1 - q_3)^2}{(q_0 + q_2)^2}, \\
 G_A &= 3 \frac{q_2 + q_4}{q_0 + q_2}, \\
 G_P &= 1.
 \end{aligned} \tag{7.13}$$

Then if $Q(c)=1$ when nonzero, the system reduces to ED.

If $Q_{TM}=0$, then the electric field in the focal region is purely transverse (TE) for any form of Q_{TE} , and

$$G_x = \frac{3}{4} \frac{q_0 - q_2}{q_0}, G_y = \frac{9}{4} \frac{q_0 - q_2}{q_0}, G_T = \frac{3}{2} \frac{q_0 - q_2}{q_0}, G_A = 3 \frac{q_2}{q_0}, G_P = 1. \quad (7.14)$$

A special transverse electric case (called TE here) is when $Q_{TE}(c)=1$ when nonzero. This corresponds to $Q_p(c)=1/(1-c^2)$, $Q_m(c)=-1/(1-c^2)$. The gains of these special cases are illustrated in Figure 7.3.

For illumination with radially polarized light [17], the parameters developed for the radially polarized case can be used [9], $Q(c)$ is the pupil function expressed as a function of $c = \cos \theta$, that includes an apodization factor that depends on the design of the optical system and an additional factor $\sqrt{1-c^2}$. Then in general $q_n = 0, n$ odd, and the gains reduce to

$$G_T = \frac{3(q_0 - q_2)}{2q_0}, G_A = \frac{3q_2}{q_0}, G_P = 1. \quad (7.15)$$

Many different apodizations could be considered for radial polarization [23]. For the particular case when $Q(c)=1-c^2$ if nonzero, the intensity at the focus is maximized, and the field corresponds to that of an axially oriented electric dipole (called R here). Again the behaviour of the parameters is presented in Figure 7.3.

7.4 Comparison of various geometries

Figure 7.3 illustrates the behaviour of the parameters for various different cases. The dashed vertical line is at a numerical aperture of 1.46 in oil, the value for a Leica lens recommended for 4Pi microscopy. We see that the electric energy density at the focus is greatest for the electric dipole case (ED) for any value of angular semi-aperture less than 90° . The transverse gain G_T is greatest for the radial polarization case for any aperture. The axial gain for all cases for low aperture is equal to 3, corresponding to $\cos^2 kz$ fringes. Then as the aperture is increased, the axial gain decreases, but this is of course accompanied by a fall in the strength of the axial side lobes. The polar (3D) gain has a constant value of unity for all cases for any value of aperture. Values of F and G_T at NA 1.46 are given in Table 1.

	F	G_T (4Pi)	$M = F G_T$ (4Pi)	G_T (single lens)	% increase in resolu.
aplanatic	0.746	0.713	0.532	0.573	10.4
mixed dipole	0.747	0.729	0.545	0.581	10.7
electric dipole	0.797	0.756	0.603	0.694	4.2
Helmholtz	0.463	0.995	0.461	0.680	17.3
parabolic mirror	0.697	0.833	0.581	0.630	13.0
TE	0.552	0.833	0.460	0.833	0
radial	0.612	1.032	0.632	0.821	10.8

Table 7.1. Values of the parameters F , G_T and M for NA = 1.46. “% increase in resolution” is for 4Pi compared with the single lens case.

We also give values for two other plane-polarized cases, for two opposing systems satisfying the Helmholtz condition, and for paraboloid mirrors. Both these cases exhibit enhanced G_T but reduced F . The Helmholtz apodization is produced by a diffractive optical element, but a similar effect can be obtained using a conventional refractive lens with an amplitude mask. We also give values in Table 1 for an overall performance parameter $M = FG_T$. The electric dipole case gives the highest value of M for all the polarizations considered except for radial polarization.

The values for the gains shown in Figure 7.3 are seen to be different from those presented elsewhere for a single lens (non 4Pi) system [8-10]. The values of F are simply double those for a single lens. This is because the power input is increased by a factor of two in 4Pi, but the intensity at the focus increases by a factor of four. Although 4Pi microscopy is primarily used for its improved axial resolution, transverse imaging is also improved because the cross-components of polarization tend to cancel out. Thus previously we showed that G_T for radial polarization at low NA becomes negative because the transverse field near the focus is stronger than the longitudinal field [9]. This effect does not apply for the 4Pi case. The values of the gains are for most cases larger than for the single-lens case. Table 1 gives some values. The percentage increase in resolution (defined in terms of the width of the parabolic central lobe) resulting from using 4Pi geometry is given: the improvement is greatest for the Helmholtz case (17.3%) as this case has strong

off-axis angular spectrum components that give strong cross components of polarization. We also note that all the examples presented give better transverse resolution than 4Pi using aplanatic plane polarized illumination: there is a 16.9% improvement for radially polarized illumination.

The normalized widths of the central lobe in the different directions can be calculated directly from the gains as $1/\sqrt{G}$. Figure 7.4 shows the transverse and axial widths for the different cases. This particular normalization gives transverse and axial widths for TE that are both unity for $\alpha = 90^\circ$. The full-width at half-maximum (FWHM) of the focal spot is then given by

$$FWHM = \left(\frac{3\lambda^2}{2\pi G} \right)^{1/2}. \quad (7.16)$$

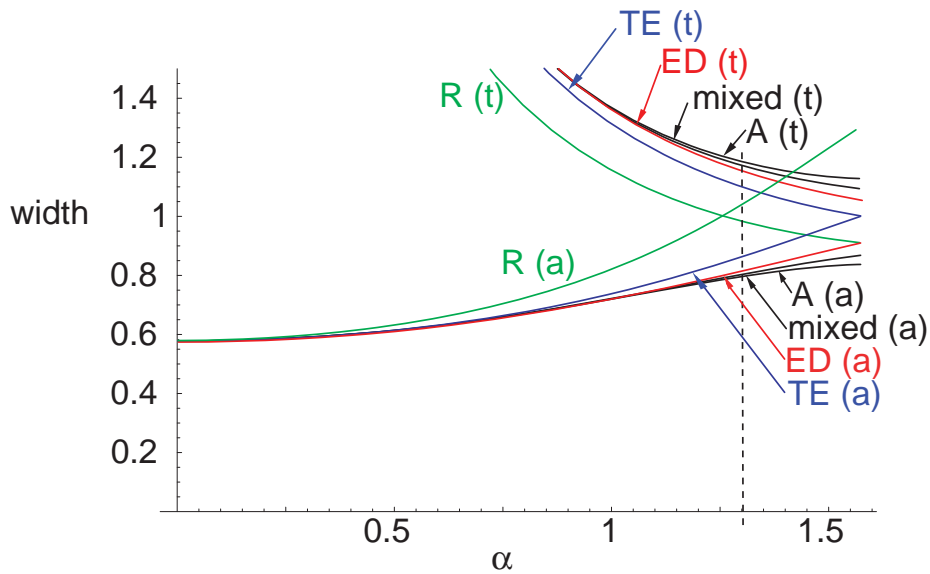


Figure 7.4. The normalized widths of the focal spot in the transverse and axial directions for 4Pi systems for different polarization cases. (t) corresponds to the transverse direction and (a) to the axial direction. The dashed line corresponds to a numerical aperture of 1.46 in oil. A is aplanatic, Mixed is mixed dipole, ED is electric dipole, TE is transverse electric 1, and R is radial polarization.

7.5 Discussion

We have derived performance factors that can be used to compare the imaging performance of 4Pi microscopes for a variety of different polarization and apodization conditions. An important observation is that the transverse resolution is improved for 4Pi microscopy, resulting from the cancellation of the longitudinal electric fields (or the transverse fields for radially polarized illumination of the lens).

References

1. S. Hell and E. H. K. Stelzer, "Fundamental improvement of resolution with a 4Pi-confocal fluorescence microscope using two-photon excitation," *Optics Communications* **93**, 277-282 (1992).
2. S. W. Hell and E. H. K. Stelzer, "Properties of a 4Pi confocal fluorescence microscope," *Journal of the Optical Society of America A* **9**, 2159-2166 (1992).
3. S. W. Hell and E. H. K. Stelzer, "Enhancing the axial resolution in far-field light microscopy: two-photon 4Pi-confocal fluorescence microscopy," *Journal of Modern Optics* **41**, 675-681 (1994).
4. C. J. R. Sheppard and H. J. Matthews, "Imaging in high aperture optical systems," *Journal of the Optical Society of America A* **4**, 1354-1360 (1987).
5. C. J. R. Sheppard and C. J. Cogswell, "Reflection and transmission confocal microscopy," in *Optics in Medicine, Biology and Environmental Research: Proceedings of the International Conference on Optics Within Life Sciences*, Series of the International Society on Optics Within Life Sciences (Elsevier, Amsterdam, 1990), 310-315.
6. M. Gu and C. J. R. Sheppard, "Three-dimensional transfer functions in 4Pi confocal microscopes," *Journal of the Optical Society of America A* **11**, 1619-1627 (1994).
7. M. Gu and C. J. R. Sheppard, "Optical transfer function analysis for two-photon 4Pi confocal fluorescence microscopy," *Optics Communications* **114**, 45-49 (1995).
8. C. J. R. Sheppard and M. Martinez-Corral, "Filter performance parameters for vectorial high-aperture wave-fields," *Optics Letters* **33**, 476-478 (2008).
9. C. J. R. Sheppard and E. Y. S. Yew, "Performance parameters for focusing of radial polarization," *Optics Letters* **33**, 497-499 (2008).
10. C. J. R. Sheppard, N. K. Balla, and S. Rehman, "Performance parameters for highly-focused electromagnetic waves," *Optics Communications* **282**, 727-734 (2009).
11. S. J. van Enk, "Atoms, dipole waves, and strongly focused light beams.," *Physical Review A* **69**, 043813 (2004).
12. C. J. R. Sheppard and K. G. Larkin, "Optimal concentration of electromagnetic radiation," *Journal of Modern Optics* **41**, 1495-1505 (1994).
13. J. J. Stamnes and V. Dhayalan, "Focusing of electric dipole waves," *Pure and Applied Optics* **5**, 195-226 (1996).
14. C. J. R. Sheppard and P. Török, "Electromagnetic field in the focal region of an electric dipole wave," *Optik* **104**, 175-177 (1996).

15. A. Drechsler, M. A. Lieb, C. Debus, A. J. Meixner, and A. Tarrach, "Confocal microscopy with a high numerical aperture parabolic mirror," *Optics Express* **9**, 637-644 (2001).
16. M. A. Lieb and A. J. Meixner, "A high numerical aperture parabolic mirror as imaging device for confocal microscopy," *Optics Express* **8**, 458-474 (2001).
17. N. Bokor and N. Davidson, "Towards a spherical spot distribution with 4p focusing of radially polarized light," *Optics Letters* **29**, 1968-1970 (2004).
18. N. Davidson and N. Bokor, "High-numerical-aperture focusing of radially-polarized doughnut beams with a parabolic mirror and a flat diffractive lens," *Optics Letters* **29**, 1318-1321 (2004).
19. J. Stadler, C. Stanciu, C. Stupperich, and A. Meixner, "Tighter focusing with a parabolic mirror," *Optics Letters* **33**, 681-683 (2008).
20. N. Lindlein, R. Maiwald, M. Konnermann, U. Peschel, and G. Leuchs, "A new 4Pi geometry optimized for focusing on an atom with a dipole-like radiation pattern," *Quantum Optics, Laser Physics and Spectroscopy* **17**, 927-934 (2007).
21. C. J. R. Sheppard, "Fundamentals of superresolution (Vol. 38, pg 165, 2007)," *Micron* **38**, 772 (2007).
22. B. Richards and E. Wolf, "Electromagnetic diffraction in optical systems. II Structure of the image field in an aplanatic system," *Proceedings of the Royal Society of London A* **253**, 358-379 (1959).
23. E. Y. S. Yew and C. J. R. Sheppard, "Tight focusing of radially-polarized Gaussian and Bessel-Gauss beams," *Optics Letters* **32**, 3417-3419 (2007).

Chapter 8 Conclusions and suggestions for further work

This study explored tissue optics modeling in biological tissue and cells. In the random non-spherical model, general functions of random non-spherical rough-surfaced particles with axially-symmetric properties were introduced. It was found that with a series of generation functions restricted by the “display window”, the medium can be characterized by a cluster of random non-spherical particles. An important feature of this generation function is that generally all kinds of shapes can be described completely with five parameters. This method can thus greatly reduce the complexity of the calculation and facilitate the process of tissue optics modeling in biological science.

The random non-spherical model combined with the T -matrix method was proposed in this study to model the tissue optics properties in biological science. We investigated the phase function, which describes the angular distribution of the scattered intensity. It was found that: i) providing the same values of effective radius and effective variance of a size distribution, different size distributions have similar phase functions. Thus only two key parameters can provide a unified classification of all distributions; ii) phase functions are insensitive to the dimension-to-length ratios D/L in most of the scattering regions for different kinds of rough cylinder. This finding is of crucial

importance in terms of characterization of cylindrical particles in tissue optics modeling, since an average parameter can be used instead of considering various values of D/L for every cylindrical particle; iii) The good agreement between theoretical predictions with the non-spherical model and experimental data confirms our hypothesis that the particles' shapes are the key contributor to tissue optics modeling. The theoretical results have slight differences with the experimental results in the forward scattering region and back scattering region. This may be attributed to the exististence of multiple scattering. The phase function for surface-equivalent spheres showed larger discrepancy with experiments, especially in the side-scattering and backscattering regions. This suggests that the scattering properties of non-spherical particles can be significantly different from those of equivalent spheres. Therefore, the random non-spherical model has the power to simulate biological tissue better than the spherical model. This random non-spherical model can thus contribute to the accurate and efficient optical description for biological science and medical diagnosis.

It is acknowledged that this study did only a preliminary analysis on modeling tissue optics properties with random non-spherical generation functions and the T -matrix method. The experimental data are limited to mouse skeleton tissue, mitochondria and rat embryo fibroblast cell. To extrapolate our conclusions to other kinds of tissue, additional laboratory experiments on particular tissue and cells and additional calculations are

needed to examine the validity of this random non-spherical model. An extension to various biological tissue and cells with different refractive indexes is also recommended, since the current computational results pertained to a specific refractive index of typical biological tissue.

It should be pointed out that this random non-spherical model did only a single scattering analysis based on the random non-spherical model. Therefore, for thick tissue where multiple scattering dominates, further work is needed to correlate the simulation to multiple scattering processes, which can be simplified with diffusion theory.

This study also investigated the fractal mechanism to model the optical properties in biological tissue. The structure function was developed to describe the interaction of light and fractal aggregates. It was found that the second order structure function is related to the fractal dimension directly. The structure function is different from the correlation function that was discussed by Xu *et al.* [1] and Sheppard [2]. The relationship is of importance since it should help to predict the fractal properties from the second order structure function, which is also related to the correlation function $R(r)$. The fractal model with the structure function has a wider scale of applications, since it can be applicable to the medium containing fractal-type aggregates; however, the correlation function cannot be used for the finite form of fractal sample.

This fractal model with structure function can be also applied in the anisotropic case. With specific limits of small directional sensitivity, the

power spectrum based on the structure function can be reduced to the isotropic case in good accordance with the analytical expressions obtained by previous work [2]. These findings have provided valuable insight into fractal tissue optics modeling of anisotropic tissue in biological science. Based on the power spectrum calculated from a series of phase contrast images, optical properties, such as anisotropy factor and reduced scattering coefficient, can be obtained directly.

The tissue fractal modeling method developed in this study is not able to describe thick biological tissue, where the size distribution of scatterers occupies a large range. The simulation results began to deviate from the experimental data as the thickness of the tissue increases. The deviation may be attributed to the existing of multiple scattering, since in thick tissue, the multiple scattering processes always dominate. Therefore, the assumption of the fractal model with structure function that single scattering processes are the main pattern in the medium brakes down. To keep the accuracy of the anisotropic fractal model, further research is needed to correlate the simulation to multiple scattering processes. To achieve this, a multi-fractal tissue model is required, where the optical properties of the thick biological tissue can be characterized with a multi-fractal mechanism. It is also recommended that a series of experiments on light scattering of different thick biological tissue be investigated in order to examine the validity of the multi-fractal property in various biological tissue and cells.

This study also examined the angular gating techniques in optical microscopy. For a confocal microscopy with angular gating technique, the three-dimensional coherent transfer function and three-dimensional optical transfer function are investigated when a pair of D-shaped apertures is used. The optical sectioning property, background rejection capability and signal level are studied when different kinds of divided apertures are used, including off-axis apertures, elliptical apertures and Schwartz apertures. If the pupils are separated by a strip of width $2d$, from the performance comparison among D-shaped, off-axis and elliptical apertures, we find that: i) given the same value of d , D-shaped apertures can obtain the best optical section properties and background rejection capability, as well as the highest signal level. This is because D-shaped apertures have the largest aperture area. However, the above three properties can be further improved by using serrated D-shape aperture, due to the Poisson spot being suppressed by the serrated edge [3]; ii) given the same kind of divided apertures, as d increases, the background decay rate increases for deep defocus planes; iii) given equal area, off-axis apertures can obtain the best optical sectioning properties and background rejection capability, as well as the highest signal level.

We also proposed a simple rule to estimate the optical sectioning and background rejection properties of a confocal system by using the integrated pupil function $P_\theta(t)$, given by the integration of the pupil function $P(\rho, \theta)$ with respect to the angle θ . The Fourier transform of $P_\theta(t)$ determines the

optical sectioning property, while the derivative of $P_{\theta}(t)$ determines the background decay rate. According to this method, Schwartz apertures, to our knowledge, are proposed for the first time to dramatically reject the background. We believe Schwartz apertures will have wide application in deep penetration imaging, for example, in focal modulation microscopy [4-6].

By combining the angular gating technique with modulation and demodulation techniques, we investigated a high performance microscopy, named focal modulation microscopy (FMM). The imaging performance of one-photon and two-photon FMM is presented. It was found that FMM can simultaneously acquire conventional confocal images and FMM images. Experimental results for chicken cartilage showed that the imaging depth of one-photon FMM can be extended to around 600 μm . Compared with conventional confocal microscopy, which is usually performed at an imaging depth up to a few tens of microns for subcellular imaging, FMM system exhibits a much deeper penetration depth. This finding is of crucial importance, since owing to the high penetration depth, non-invasive optical biopsies can be obtained from patients and *ex vivo* tissue by morphological and functional fluorescence imaging of endogenous fluorophores such as NAD(P)H, flavin, lipofuscin, porphyrins, collagen and elastin. The simulation results suggest that the background of FMM decays with distance from the focal plane most quickly among all the microscopy technologies discussed. This property is of importance since it should help to reduce the cross-talk between the in-focus

image and out-of-focus images, thus contributing to the high spatial resolution and deep imaging penetration depth. The superior image performance of FMM has a simple explanation. In the FMM case, only the ballistic photons in the focal region can be detected due to their well defined phase and polarization. However, in confocal microscopy, some ballistic photons scattered from the vicinity of the focal plane can still be collected by the detector through the pinhole. Thus the spatial filtering effect using only a pinhole in confocal microscopy is not as effective as in FMM, where the spatial filtering effect is enhanced by a phase modulator. Moreover, detection of the in-phase signal after demodulation in FMM, instead of the modulation signal, gives better spatial resolution and deeper penetration depth, making it promising for *in vivo* imaging. In practice, the use of lock-in amplifier can further enhance the noise rejection by reducing noise components that do not fall on the modulation frequency.

To our knowledge, we have investigated for the first time a two-photon focal modulation microscopy (2PFMM). The theoretical comparison of signal to background ratio between 2PFMM and traditional two-photon fluorescence microscopy (2PM) reveals that using 2PFMM the imaging penetration depth of 2PM can be extended by a factor of up to 3. An added benefit of our technique is that it can improve the spatial resolution due to the fact that the excitation light is more concentrated around the focal point and decays more quickly outside the focal volume. Moreover, using modulation and

demodulation techniques can further enhance the noise rejection by reducing noise components that do not fall near the modulation frequency.

It should also be pointed out that the analysis of focal modulation microscopy is under the paraxial approximation. This approximation is largely true when the numerical aperture is less than 0.7. However, it loses its validity as the numerical aperture increases above 1. Therefore, for a system with large numerical aperture, vector diffraction theory is needed to be taken into account. It is also recommended that the focal modulation microscopy with various polarization conditions be established and described, which can be greatly different from the unpolarized cases.

The effects of different apodization conditions and polarization distributions on imaging in 4Pi microscopy are also discussed, which is a preparation to introduce polarization effect in focal modulation technique. Performance parameters are derived that allow the different implementations to be compared. 4Pi microscopy is mainly used because of its superior axial imaging performance, but it is shown that transverse resolution is also improved in the 4Pi geometry, by as much as 25% compared with focusing by a single aplanatic lens. Compared with plane polarized illumination in a 4Pi aplanatic system, transverse resolution in the 4Pi mode can also be increased by about 18%, using radially polarized illumination, but at the expense of axial resolution. The electric energy density at the focus for a given power input can

be increased using electric dipole polarization, which is relevant for atomic physics experiments such as laser trapping and cooling.

For the two-photon FMM, we used a statistical approach to describe the effects of multiple scattering. We found the results agreed well with Monte Carlo modeling. It would be useful to extend this approach to 1-photon confocal microscopy, and to investigate in detail the effects of multiple scattering in the comparison of different theories based on integrated intensity and extinction of the excitation.

References

1. M. Xu, and R. R. Alfano, "Fractal mechanisms of light scattering in biological tissue and cells," *Opt. Lett.* **30**, 3051-3053 (2005).
2. C. J. R. Sheppard, "A fractal model of light scattering in biological tissue and cells," *Opt. Lett.* **32**, 142-144 (2007).
3. W. Gong, K. Si, and C. J. R. Sheppard, "Improvements in confocal microscopy imaging using serrated divided apertures," *Opt. Commun.* **282**, 3846-3849 (2009).
4. W. Gong, K. Si, N. G. Chen, and C. J. R. Sheppard, "Improved spatial resolution in fluorescence focal modulation microscopy," *Optics Letters* **34**, 3508-3510 (2009).
5. N. G. Chen, C. H. Wong, and C. J. R. Sheppard, "Focal modulation microscopy," *Opt Express* **16**, 18764-18769 (2008).
6. K. Si, W. Gong, N. G. Chen, and C. J. R. Sheppard, "Penetration depth in two-photon focal modulation microscopy," *Optics Letters* (submitted).